

IPSL/ONERA

# Annual Report Climaviation 2021-2022

Agreement number 2021-39 relating to the « Aviation & Climate » project



The Climaviation project team  
17/05/2022  
Final version: 1

## TABLE OF CONTENTS

<b>EXECUTIVE SUMMARY .....</b>	<b>2</b>
<b>1. AXIS 1: CONTRAILS .....</b>	<b>4</b>
1.1. WP 1.1: Microphysical mechanisms of particle and ice formation .....	4
1.2. WP 1.2: Modelling of contrail formation (near field) .....	6
1.3. WP 1.3: Influence of aircraft configuration .....	9
1.4. WP 1.4: Evolution of contrails at intermediate scales .....	15
1.5. WP 1.5: Evolution of contrails on climatic scales .....	37
1.6. WP 1.6: Detailed study of the radiative impact of contrails .....	41
<b>2. AXIS 2: ATMOSPHERIC CHEMISTRY .....</b>	<b>51</b>
2.1. WP 2.1: Effective emission index .....	51
2.2. WP 2.2: Improvement of the overall model .....	53
2.3. WP 2.3: Impact of emissions on ozone and oxidizing capacity .....	54
2.4. WP 2.4: Impact of emissions on methane .....	54
<b>3. AXIS 3: IMPACT OF AEROSOLS ON NATURAL CLOUDS .....</b>	<b>56</b>
3.1. WP 3.1: Competition with background aerosols .....	56
3.2. WP 3.2: Aerosol transport from aviation .....	59
3.3. WP 3.3: Cloud response .....	62
<b>4. AXIS 4: OBSERVATIONS .....</b>	<b>65</b>
4.1. WP 4.1: Use of existing data .....	65
4.2. WP 4.2: Data acquisition .....	76
4.3. WP 4.3: Model evaluation for contrail prediction .....	76
<b>5. AXIS 5: CLIMATE IMPACTS OF AVIATION .....</b>	<b>77</b>
5.1. WP 5.1: Traffic and emission scenarios .....	77
5.2. WP 5.2: Integration of all non-CO <sub>2</sub> effects in the climate model .....	81
5.3. WP 5.3: Estimation of climate impacts .....	81
5.4. WP 5.4: Development of OSCAR-Aviation .....	81
<b>6. AXIS 6: OPTIMISATION STRATEGIES .....</b>	<b>82</b>
6.1. WP 6.1: Assessment and relevance of climate change metrics for aviation .....	82
6.2. WP 6.2: Climate impact of the fleet estimated by OSCAR .....	82
6.3. WP 6.3: Quality and relevance of numerical weather prediction for contrail forecasting .....	82
6.4. WP 6.4: Study of optimisation strategies .....	83
<b>REFERENCES .....</b>	<b>88</b>

## EXECUTIVE SUMMARY

The Climaviation research project on the climate impacts of aviation is a partnership between Institut Pierre Simon Laplace (IPSL, climate research) and the French Aerospace Lab ONERA (aeronautical research). The project is funded by the Direction Générale de l'Aviation Civile (DGAC) for the period 2021-2026.

The project is structured around 6 axes of research. The project has three objectives:

- To reduce uncertainties in the radiative forcing exerted by contrails and contrail cirrus (Axis 1), aviation emissions with a focus on NO<sub>x</sub> (Axis 2) and interactions between aviation aerosols and clouds (Axis 3). Improved process understanding is facilitated by modelling at different scales, combined with the exploitation of existing observations and the acquisition of new observations (Axis 4).
- To quantify the radiative forcing of the current fleet, design scenarios of future aircraft traffic and technological changes, and quantify the radiative forcing associated with those scenarios (Axis 5).
- To evaluate strategies to minimize the total climate impact of aviation including by looking for compromises between CO<sub>2</sub> and non-CO<sub>2</sub> effects, for both individual flights and a fleet (Axis 6).

This Annual Report covers the period between the official start of the project in May 2021, and May 2022. Most work packages report progress in the first year, including those in the more downstream Axes 5 and 6. The project team has grown quickly: 32 individual researchers contributed to this annual report, including permanent researchers at IPSL and ONERA, postdoctoral researchers, research engineers, PhD students hired on the project and Masters interns. Progress in the active work packages over the past few months is summarised below. There were no significant deviations to the workplan.

### Axis 1: Contrails

- *WP 1.1 Microphysical mechanisms of particle and ice formation:* Preliminary quantum chemistry calculations, which do not account for the kinetics of chemical reactions, suggest that the most efficient way to form aerosols from nitric acid involves charged nitric acid clusters.
- *WP 1.2 Modelling of contrail formation (near field):* Design of a wind tunnel experiment looking at interaction between a jet and a wingtip vortex has begun. The experiment itself is planned for 2023.
- *WP 1.3 Influence of aircraft configuration:* Different wing and engine configurations have been selected for modelling studies on their impact on the vortex phase. Preliminary results from a PhD thesis suggest that geometry of the airplane can affect mixing of the jets and wake, and therefore condensation.
- *WP 1.4 Evolution of contrails at intermediate scales:* A literature review of methods to simulate contrail ageing from the vortex to the diffusion and dissipation phases has been concluded. Studies of a numerical strategy to cover those different phases with a hierarchy of models (RANS calculations, Large Eddy Simulation, Limited-Area Modelling) is under way.
- *WP 1.5 Evolution of contrails on climatic scales:* A parameterization for ice supersaturated regions (ISSR) has been added to the IPSL LMDZ climate model. Preliminary tests suggest that it behaves reasonably but further calibration is needed.
- *WP 1.6 Detailed study of the radiative impact of contrails:* A benchmarking of six radiative transfer codes used at IPSL and ONERA has begun. A PhD thesis has started at IPSL on the radiative impact of heterogeneities in cirrus cloud fields, with improvements to a Monte-Carlo radiative transfer already being deployed.

### Axis 2 Atmospheric Chemistry

- *WP 2.1 Effective emission index:* Work has begun on devising a strategy to link computational fluid dynamics calculations by ONERA's CEDRE model (first few seconds of the aircraft plume evolution) to the chemistry parametrization used by IPSL's LMDZ INCA chemistry-climate model.

- *WP 2.2 Improvement of the global model:* The chemistry parametrizations of LMDZ INCA are being adapted to the new version of the model, which includes more vertical levels, a new radiation code, and new convection and boundary layer parametrizations.
- *WP 2.3 Impact of emissions on ozone and oxidative capacity:* A submitted paper describes a new quantification of aviation NO<sub>x</sub> radiative forcing using LMDZ INCA. NO<sub>x</sub> forcing in these simulations is slightly negative for both present-day and 2050 emissions because of revisions to methane radiative forcing and the inclusion of feedback on aerosol formation. Uncertainties remain high.
- *WP 2.4 Impact of emissions on methane:* The submitted paper includes revised calculations of methane feedback on its own lifetime, tropospheric ozone and stratospheric water-vapour adjustments, and carbon dioxide production, which all contribute to total methane forcing and its uncertainty.

### **Axis 3 Impact of aerosols on natural clouds**

- *WP 3.1 Competition with background aerosols:* A configuration of the MONC large eddy simulation model that represents the whole chain from aerosol activation to ice crystal nucleation is being built. A cirrus cloud is already obtained with soluble aerosols and homogeneous freezing of cloud droplets.
- *WP 3.2 Aerosol transport from aviation:* A Masters internship is investigating tracer transport in the LMDZ climate model. Preliminary results suggest residence times longer than 50 days for particulate emissions at 250 hPa, leaving open the possibility of long-range horizontal and vertical transport.
- *WP 3.3 Cloud response:* Previous results on the response of a gravity-wave cirrus cloud to a perturbation of its ice crystal number have been successfully reproduced with a no-aerosol version of MONC.

### **Axis 4 Observations**

- *WP 4.1 Use of existing data:* An analysis of radiosonde measurements near Paris and ERA5 suggests that meteorological conditions that favor the formation of ice supersaturated regions are more humid than average, while short-lived contrails are characterized by average humidity. Decreasing flight altitude can reduce contrail formation in summer months but is less effective in other seasons. In addition, an automatic contrail detection algorithm in hemispheric camera images is being developed.
- *WP 4.2 Data acquisition:* A new hemispheric camera has been installed at the SIRTAs instrumented site south of Paris. It will provide images of the sky at increased spatial and temporal resolutions.

### **Axis 5 Climate impacts of aviation**

- *WP 5.1 Traffic and emission scenarios:* An analysis of five existing air traffic databases suggests that a combination of databases is needed to accurately count global air traffic. A new model to estimate global fuel consumption by aviation is being built.
- *WP 5.3 Estimation of climate impacts:* Different methods to estimate carbon dioxide emissions by aviation, accounting or not for different aircraft and engine types, lead to different estimates but the more complex methods require information that is difficult to get from traffic databases.

### **Axis 6 Optimization strategies**

- *WP 6.2 Climate impact of the fleet estimated by OSCAR:* The first official Climaviation paper compared different methods of attributing the forcing of carbon dioxide to aviation and found that the most accurate method leads to a radiative forcing 12% larger than that from previous studies.
- *WP 6.4 Study of optimisation strategies:* A comparison of wind-optimised (fastest) trajectories in the North Atlantic Flight Corridor to actual flight trajectories suggest that many flights already follow the wind-optimised trajectories. The large-scale structure of ice supersaturated regions makes them difficult to avoid on some routes.

## 1. AXIS 1: CONTRAILS

The objective of this axis of research is to study the formation, ageing and characteristics of contrails, and their possible evolution into induced cirrus clouds. For each of these phases, the aims are to improve the understanding and modelling of the various mechanisms involved in the formation and the evolution of the contrail and influencing its radiative properties on the climate scale.

### 1.1. WP 1.1: Microphysical mechanisms of particle and ice formation

Contributor: Ismael K. Ortega (ONERA)

Work package 1.1 is devoted to the analysis of the mechanisms of formation of the ice crystals that form contrails. The objective is in particular to identify the respective influence of the various mechanisms which can intervene depending on the chemical composition of the fuels used.

The first task of this work package is related to nucleation mechanisms at work in the case of hydrogen fuel. The objective is to determine if nitric acid produced from oxidation of NO<sub>x</sub> can be a precursor of volatile particles.

With this aim, we have started a series of quantum chemical calculations to determine the evaporation rates of molecular clusters of nitric acid. In addition, we have included in the study other species like ammonia, which is known to stabilize acid clusters formed in the atmosphere.

The calculations are done in two steps (Figure 1-1); a first set of calculations is done to do a conformational sampling of each cluster studied. In other words, several clusters are studied but changing the arrangement of the molecules in them. After this step, the most stable clusters are selected to perform high level calculations using the commercial package Gaussian. The Gibbs formation energies of each cluster are obtained as results of the calculations. These Gibbs formation energies can be used to calculate the evaporation rates of each cluster. Once a complete set of clusters is studied, the evaporation rates can be used in the Atmospheric Clusters Dynamics Code (ACDC) model to estimate the formation rate of volatile particles in different conditions.

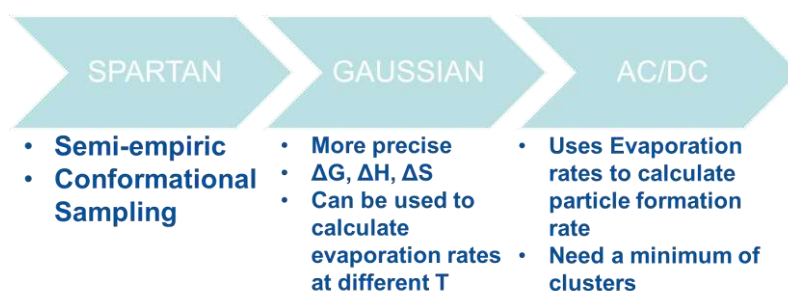


Figure 1-1: Schematic representation of the work planned in the first task of WP 1.1

The Gaussian suite was installed successfully on the ONERA supercomputer SATOR in January 2022. So far, calculation for pure neutral nitric acid clusters up to 4 molecules, negatively charged pure nitric acid clusters up to 3 molecules, and neutral clusters containing one ammonia molecule and up to 2 nitric acid molecules have been done. The objective of the calculations is to obtain formation energies for clusters containing up to 4 nitric acid and 4 ammonia molecules, both neutral and charged (positively and negatively)

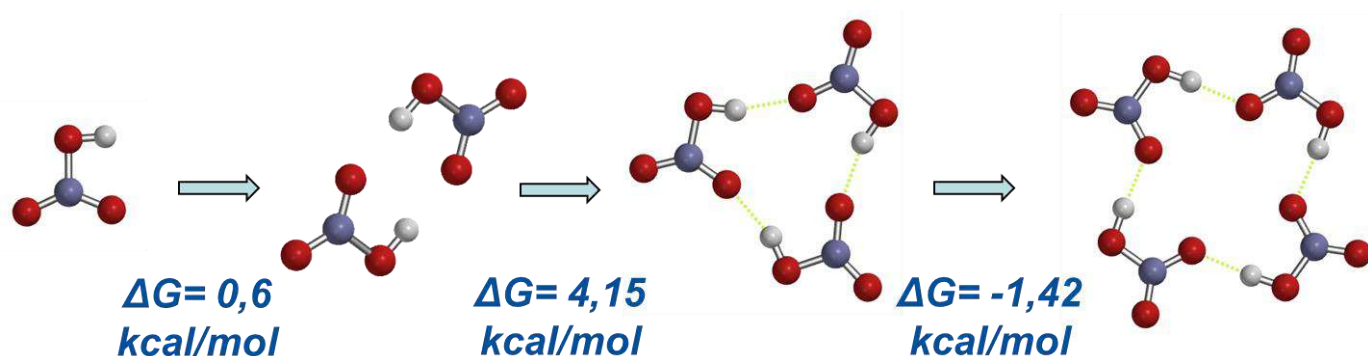


Figure 1-2: Addition energies for neutral pure nitric acid clusters up to 4 molecules. Red balls represent O atoms, blue balls represent nitrogen atoms and white balls represent hydrogen atoms. All addition Gibbs free energies are calculated at 298 K.

Results obtained for neutral pure nitric acid clusters are shown in Figure 1-2. Gibbs free energies are given for each step. It must be kept in mind that these results are preliminary, and that they only reflect the stability of each cluster. To determine the role of nitric acid as volatile particle precursor, all cluster dynamics must be considered. Nevertheless, we can observe how the formation of nitric acid clusters is not favorable at this temperature.

Results for neutral clusters containing one ammonia molecule are summarized in Figure 1-3. Preliminary results obtained for those clusters show how the addition of an ammonia molecule to a nitric acid molecule is favorable, while further addition of nitric acid is not. This is a clear difference with sulfuric acid clusters, where the addition of a second molecule of sulfuric acid to a cluster of one sulfuric acid and one ammonia molecule induces a proton transfer from sulfuric acid to ammonia, resulting in a big stabilization of the cluster. On the other hand, in the case of Nitric acid, the addition of a second acid molecule is not enough to induce the proton transfer, this, linked to the relative stability of nitric acid-ammonia cluster, results in making the addition of nitric acid to the cluster unfavorable.

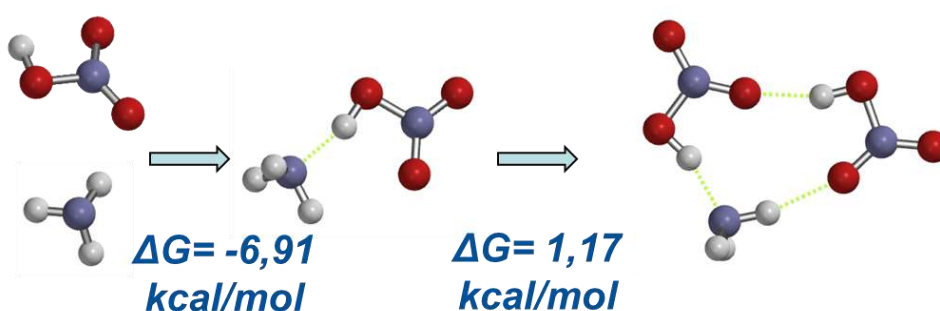


Figure 1-3: Addition energies for neutral pure nitric acid containing one ammonia molecule clusters. Red balls represent O atoms, blue balls represent nitrogen atoms and white balls represent hydrogen atoms. All addition Gibbs free energies are calculated at 298 K.

The last clusters where results are available are the negatively charged pure nitric acid clusters (Figure 1-4). In this case, results show how addition of nitric acid is favorable up to clusters containing 3 molecules of nitric acid. Calculations with larger clusters must be carried out to confirm this tendency and a potential impact of this pathway in volatile particle formation.

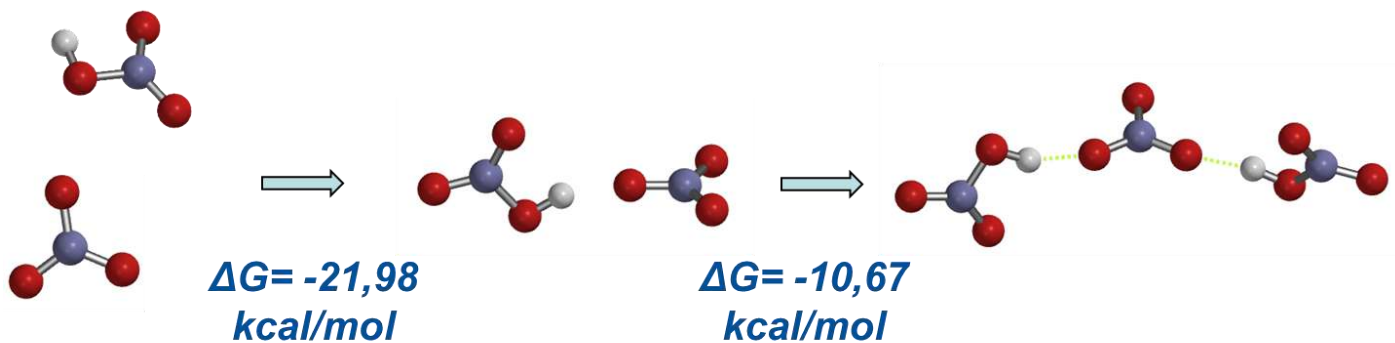


Figure 1-4: Addition energies for negatively charged pure nitric acid clusters. Red balls represent O atoms, blue balls represent nitrogen atoms and white balls represent hydrogen atoms. All addition Gibbs free energies are calculated at 298 K.

## 1.2. WP 1.2: Modelling of contrail formation (near field)

Contributor: Vincent Brion (ONERA), Marie Couliou (ONERA), Thibault Leudiere (ONERA)

The objective of work package 1.2 is first to describe the interaction between a jet and a wingtip vortex within a specific wind tunnel test to acquire experimental data. Then, later in the project, to simulate the studied configuration with the ONERA's CEDRE code. The comparison of the simulation results with the experimental data should mainly help to make the appropriate choices in terms of numerical approaches (turbulence models, meshing) or to improve them to properly simulate the mixing of an engine jet and its interaction with the aircraft wake.

The interaction of the jet exhausts with the wake of the aircraft dictates the intermediate evolution of the contrail. After a few wingspans behind the aircraft, the jet exhausts are entrained and mixed by the vortices that have rolled-up from the vortex sheet issued by the aircraft. This interaction between a jet that is turbulent with a vortex that on the contrary tends to remain laminar generates a highly inhomogeneous and unsteady flow that is difficult to capture with current simulation tools. Moreover, due to the various scales involved (the "small" transverse dimensions of the jet and vortices and, at the other end, the "long" axial dimension of the wake), the computational power required for the simulation is very high. Yet the understanding and the modelling of this phase of the evolution of the contrail are important to correctly initialize the localization and distribution of ice crystals in the atmosphere after the vortices have relaxed into the atmosphere (from 100 to 1000 wingspans behind the aircraft).

In this activity, the goal is to describe the evolution of the jet interacting with the vortex wake in the first few seconds of the contrail evolution. The thermodynamic and chemistry of the jet and various phases of the flow are not the primary concern here because we assume that the formation of the ice crystals forming the contrails occurs very rapidly after the jet exhaust and therefore the interaction phase between the wake and the jet is primarily concerned with an already formed ice plume. Hence the motivation is to investigate the mixing of this plume and its distribution in space following the downstream evolution of the flow. Therefore, we consider the jet exhaust as a passive scalar and do not consider the mass transfers that participate in ice formation or depletion.

The analysis is carried out using a wind tunnel experiment. Because the wake shortly downstream of the aircraft is formed of two trailing vortices, we neglect the influence of the precise geometry of the aircraft and

consider instead a lifting wing of rectangular planform. The wing is set with jet engines underneath whose position can be varied laterally to explore the influence of the jet to wing tip distance. Here also the detailed geometry of the jet integration about the wing is overlooked. Both the incidence of the wing and the mass flow rate of the jet can be varied in order to vary the lift to thrust ratio. The reference case is for cruise-like conditions, and a lift coefficient approximately equals 0.5.

The experiment will take place at the Lille Fluid Mechanics Laboratory (LFML) facility. This wind tunnel features a long (40 m) and wide (1 m height per 2 m width) test section. The flow speed is 9 m/s in the test section inlet section and increases up to 10.1 m/s at the outlet. The boundary layer thickness at the lateral walls is 0.1 m at the section  $x = 6.8$  m, 0.16 m at  $x = 12.5$  m and 0.242 m at  $x = 19.2$  m. The turbulence level is about 0.3%.

A schematic of the experimental setup is shown in Figure 1-5. It offers a side view of the model equipped with the jet and illustrates the wake formed by the jet and vortices. The preliminary positioning of the test model is also provided. The wing is made of a NACA0012 airfoil geometry, of chord 0.125 m and span 0.5 m similarly to the model used by Jacquin et al (2007). The mast holds the model from the roof of the test section and features a NACA0015 profile. The flow is investigated downstream of the model up in principle to 40 wingspans, but we consider that due to measurement constraints and reduced vortex intensity, we will probably not be able to reach such a far distance, and rather plan to follow the flow up to 20 wingspans. The roll-up is almost complete at about 10 wingspans in the wind tunnel, but that will be checked during the test campaign.

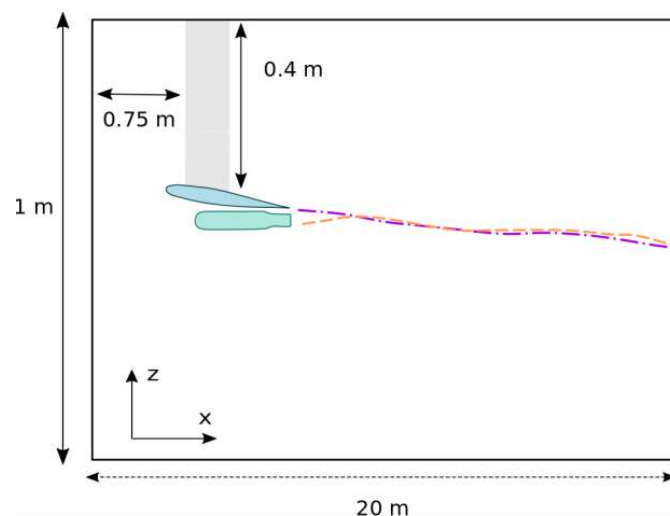
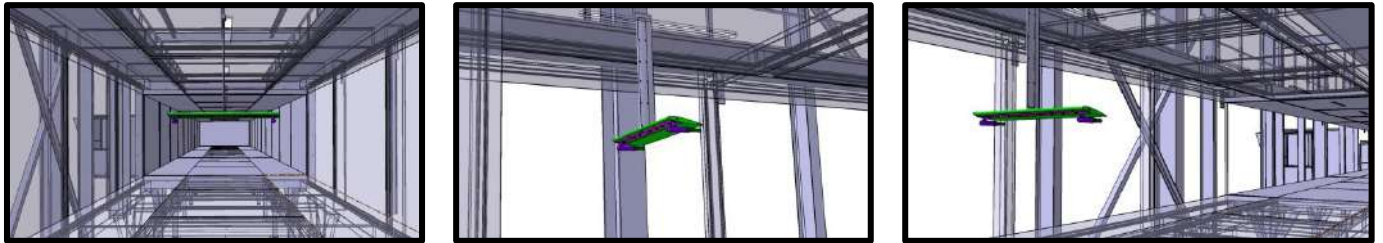


Figure 1-5: Schematic of the experiment on the jet / wake interaction, installed in the LMFL wind tunnel. Side view. The purple and orange lines indicate the locus of the tip vortex and jet, respectively

During this first period of the Climaviation project, the work has focused on the definition of the experimental setup and design of the model. We have started the CAD of the model and explored several options to integrate the jets underneath the wing. Unlike Jacquin et al (2007), in this test setup, the compressed air that feeds the jets will be channeled through the mast and the wing. The mass flow rate is on the order of 1 g/s to 10 g/s corresponding to jet velocity on the order of 10 m/s to 40 m/s. The jet diameter is 0.01 m. The lateral positions of the jet are given in terms of the distance to wing tip normalized by the wingspan and are planned to take values in the set (5, 10, 21, 30, 40) percent with a last position at the root chord with a single jet twice the diameter of the side jets (that is 0.02 m). The incidence of the NACA0012 wing can be varied in the set (5, 7, 9) degrees about the horizontal axis. Note that the jets are oriented horizontally independently of the wing

incidence. A view of the CAD is shown in Figure 1-6. The model is installed in the test section close to its upstream end.



*Figure 1-6: View of the CAD drawing of the test setup that is prepared for the wind tunnel testing of the jet / vortex wake interaction in LMFL wind tunnel facility in Lille. From left to right: front view and two side views.*

The velocity measurements of the flow will be carried out by Particle Image Velocimetry (PIV) in transverse planes located at a selection of axial distance ( $L_x$ ) from the wing axis. A low speed stereo PIV system is considered in transverse ( $y,z$ ) planes covering the wake development over one half side of the setup, as a consequence of the symmetry. Therefore, in the PIV plane only one jet and one tip vortex will be observed. A preliminary check of the full symmetry of the flow will be accomplished using fog visualizations. The case of the middle jet will be considered separately. The typical PIV plane size is about  $L_y = 0.2$  m per  $L_z = 0.2$  m. The PIV seeding is made of show fog. The jets need also to be seeded; this is under analysis. We plan to carry out the PIV measurements at sections of axial distances in the set  $L_x = (0.5, 1, 2, 4, 8, 16)$  wingspans from the wing trailing edge (defined for 0-degree incidence). The dataset that results from the combination of the PIV measurement section and jet to wing tip distance parameter leads to approximately 36 PIV acquisitions.

A point of concern is the tracking of the jet exhaust. This tracking is a crucial question for the experiment to describe the dispersion of the jet exhausts within the vortex wake. In the experiment of Jacquin et al (2007), the jets were heated so that the temperature field served as the tracking quantity. However, the jet temperature decreases very rapidly downstream due to the intense mixing of the jet by turbulence and therefore the temperature is only an efficient tracker at a close distance from the exhaust. In the present project, an analysis of the best tracking methodology will be carried out. There are currently several options: seeding of the jets (alone) or simply by analyzing the flow field (for instance using the kinetic turbulence intensity - the jet is a zone of high turbulence). In any case, the tracking of the jet over such a large distance is a challenge.

In the coming period, the CAD of the model will be completed. Several mechanical details need to be worked out, in particular the attachment of the jet to the wing, and the turbulent grids inside the jets. Furthermore, the compressed air system feeding the jets from the top of the mast needs to be validated in terms of tube internal diameters to prevent flow blockage and allow for the required range of mass flow rate. As for the agenda, the completion of the test model design is planned for September 2022. Then the manufacturing of the model will take place. Next, at the beginning of 2023, the model compressed air system will be tested in laboratory and finally the model will be sent to the LMFL facility for the test campaign. The test campaign is planned within the first semester of 2023.

### 1.3. WP 1.3: Influence of aircraft configuration

Contributors: Weeded Ghedhaïfi (ONERA), Pierre S Saulgeot (ONERA)

The objective of work package 1.3 is first to study the influence of the mixing mechanisms and the aircraft configuration, and secondly to evaluate the possibilities of action on the wake to act on the evolution of the contrail.

#### 1.3.1. *Study of the influence of aircraft configuration and propulsive layout on contrail formation*

Different configurations will be analyzed by detailed 3D simulations with the CEDRE code to evaluate the influence of aircraft geometry on the characteristics of contrails that can form. The comparison between the different configurations should provide a better understanding of the role of the aircraft wake on the evolution of the jet plume. The study will consider for instance:

- the evolution of the plume with and without the aircraft wake (i.e., without the wake vortex) by comparing the plume of a single engine jet (Figure 1-7) for typical cruising altitude conditions and the plume evolving behind the whole aircraft (Figure 1-8). This comparison should allow a better understanding of the role played by the wing tip vortices on the plume dilution.
- the evolution of the plume for different engine positions: the original one (Figure 1-8), another position of the engine under the wing (e.g. Figure 1-9) and finally by moving the engine to the tail (e.g. Figure 1-10).

The study may be enriched by considering other variants like wings equipped with winglets or more generally, other types of aircraft if the geometries are available. This work will be closely linked to the study of the intermediate field addressed in work package 1.4 to determine the influence of the aircraft configuration on the fully developed properties of contrails and their radiative impact. If the impact of near field processes on the evolution of the contrail in the far field is recognized, then the simulation of different aircraft types (e.g., medium and jumbo jet) would be helpful to provide a database for global models with specific contrails properties by aircraft type. Finally, the better understanding of the possible link between the aircraft geometry and then the wake dynamics on fresh contrail properties may provide sensible information about possible contrail control by design, by keeping the plume subsaturated or through enhanced evaporating conditions for instance.

The first calculations will be carried out using the CRM (Common Research Model), an open source geometry representative of a B777 (Vassberg et al (2008)), which has already been used for previous studies dedicated to 3D simulation of contrails formation at ONERA (Montreuil et al. (2018) and Ghedhaïfi et al. (2019)).

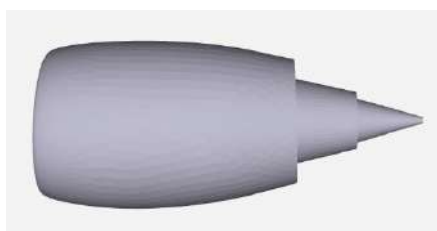


*Figure 1-7: Single engine*



*Figure 1-8: A B777 aircraft like with the original position for engines*



*Figure 1-9: A B777 aircraft like with a shifted position for the engines*

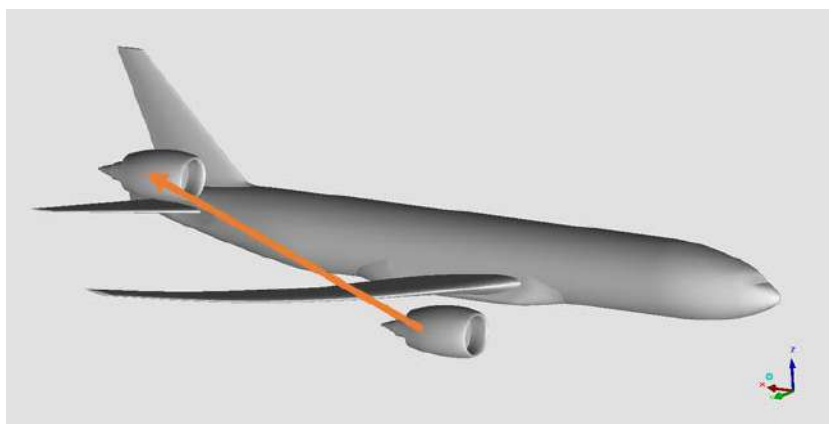


*Figure 1-10: A B777 aircraft like where the engine is moved to the aircraft tail*

### 1.3.2. Study of the mixing of the jets by the wake and the possibilities of changes

The work is carried out within the framework of a PhD thesis. The first part of the work has been dedicated to a parametric study of the mixing of a jet in a vortex wake under atmospheric stratification.

#### 1.3.2.1. Context

Four phases can be distinguished in the evolution of the wake and engine jets in the atmosphere (see Gerz et al., (1998)): the jet phase, the vortex phase, the dissipation phase and the diffusion phase. Figure 1-11 shows the first two phases, the second of which is of greatest interest here. There is no strict separation between these different phases.



Figure 1-11: The first two phases of the jets.

Qualitatively, the jet phase corresponds to the initial phase in which the jet has strong axial momentum (parallel to the plane motion), but this decreases rapidly. Generally, the transition from the jet phase to the vortex phase is considered to have taken place when the jet dynamics has decreased very sharply and can be neglected. It can be described using the ratio  $R_3$  introduced in Jacquin and Garnier (1996) of the axial momentum to the transverse momentum of the jet:

$$R_3 = \frac{\Delta p}{\rho_0 V_\theta^2 A_j} = 16\pi \frac{\Delta p}{\rho_0 \Gamma_0^2} \left( \frac{r(x)}{D(x)} \right)^2$$

In this relation  $A_j = \frac{\pi D(x)^2}{4}$  is the cross-sectional area of the jet at a distance  $x$  downstream of the engine outlet. The jet is located at a distance  $r(x)$  from the center of the vortex, far away enough to consider that the flow due to the vortex is potential, *i.e.*,  $V_\theta(r) = \frac{\Gamma_0}{2\pi r}$ . A semi-empirical law for  $D$  is given by  $D(x) = a_D x$  with  $a_D$  of the order of  $10^{-1}$  (see Papamoschou and Roshko (1988)). Jets produce a nominal thrust intensity  $p = \rho_j U_j^2 A_j(0)$  where  $A_j(0) = \frac{\pi \phi_j^2}{4}$  is the initial diameter of the jet and  $U_j$  the engine jet velocity. Cruising flight is characterized by the equality of thrust and drag. The increment of momentum flow induced by the engine whose flow is fed upstream by the external flow  $U_0$  is  $\Delta p = \rho_j U_j (U_j - U_0) A_j(0)$ . A justification for the existence of the jet phase is given by  $R(0) \gg 1$ . The transition takes place for the length  $x_{jet}$  downstream of the jet such that  $R_3(x_{jet}) \simeq 1$ . Taking the values corresponding to an A-330 (see Jacquin and Garnier (1996)) we obtain  $\frac{x_{jet}}{b_0} \simeq 3.7$ .

At this point, the wake vortices, generated by the rolling up of the vortex sheet issued by the aircraft various lifting surfaces, have already formed and are beginning to entrain the jets plume into their velocity field. Atmospheric effects also start to play an important role: stratification, wind shear, turbulence. The physics of the realistic flow remains to be fully understood. Free of turbulence and stratification, vortices descend throughout the atmosphere by induction of about half a dozen wingspans. After that, instabilities (most likely the Crow (1970) or the elliptical (Le Dizès and Laporte (2002) instabilities) will develop, giving rise to a succession of non-linear mechanisms that will eventually lead to the total loss of coherence of the flow and the dissipation of the wake momentum. High levels of turbulence accelerate the dissipation and bypass the Crow mechanism by strong transient dynamical processes (see Crow and Bate (1976)). The thermal stratification of the atmosphere modifies the vertical momentum of the vortices by buoyancy effect and baroclinic torque, which can significantly transform the vertical dynamics of the flow.

The question of the jet mixing in such a stratified environment especially requires further inquiry, as we do here. We review associated work thereafter. The dynamics of the engine jets and of the vortex sheet roll-up was the subject of a numerical study (Garnier et al. (1997)) and a wind tunnel experiment (Jacquin et al. (2007) to describe the influence of the position and temperature of the jets on the position of the plume in the near field. The work of Jacquin and Pantano (2002) then focused on the persistence of wake vortices. The entrainment of jets in these vortices during the vortex phase was then analyzed in Brunet et al. (1999) using a laminar numerical simulation. Several authors (for instance Gerz et al. (1998), Paoli et al. (2003), Misaka et al. (2012), Paoli et al. (2013), Unterstrasser et al. (2014)) added the consideration of atmospheric conditions – stratification, wind shear, turbulence. In particular, stratification has been shown to have an important influence on the dynamic evolution of the wake, in particular the creation of the secondary wake. Turbulence can destabilize the vortices and cause instabilities to appear which dissipate them.

In this study, we investigate the role of stratification and jet engine lateral distance on the evolution of the jet plume in the vortex phase by conducting a parametric study on a 2D DNS. Figure 1-12 (b) shows that most of the dilution takes place during the jet phase and follows the straight line of slope  $G$ . The end of the dilution takes place during the vortex phase. The wake then interacts with the atmosphere and the curve may change. Thermodynamic processes change the dilution curve, and we will investigate that in the next stage of the study. Vortex entrainment will also have a strong effect, mostly because vortices move down from flight altitude, at a rate that depends on stratification. This changes the surrounding pressure and temperature seen by the contrail. The phenomena at play during this phase can then favor or hinder the appearance and persistence of contrails.

The vortex wake is considered to be two parallel horizontal vortices and the plume is considered to be two passive scalar distributions moving, deforming and diluting under the wake influence. The Earth atmosphere is naturally stratified in temperature and the saturation vapor pressure varies with it. Thus, it is important to know the position of the plume to determine whether a condensation trail might appear and persist. The value of the atmospheric stratification is therefore of great importance in the study of contrails. The position of engine jets in the wake of the aircraft has been little studied. However, it is an important parameter with regard to the plume lift and its evolution in the wake when it interacts with the atmosphere. Several simulations were therefore carried out for several initial length  $b_{jet}$  between the two initial plume disks. The initial altitude of the plume was not changed.

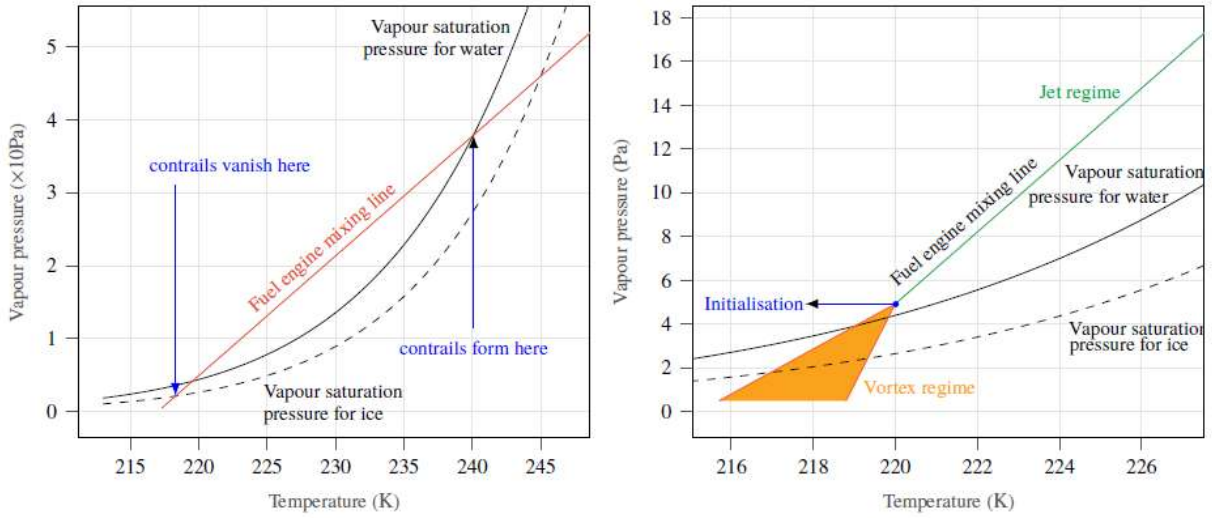


Figure 1-12: (a) Illustration of the Schmidt-Appleman criterion for aircraft contrails. We use Goff-Gratch equations (see Goff (1946)) for the vapor saturation pressure formulas. (b) Schematic representation of the first two phases on the dilution line. We initialize the study at the beginning of the vortex phase.

The main scales of the study are for space the initial distance  $b_0 = \frac{\pi}{4} b$  between the vortices ( $b$  is the wingspan) and for time  $\tau_0 = \frac{2\pi b_0^2}{\Gamma_0}$  ( $\Gamma_0$  is the initial circulation of the vortices). The time of appearance of the Crow instability is of the order of 5 to 8  $\tau_0$  (Johnson et al. (2016)).

### 1.3.2.2. Results

The influence of the Brunt-Väisälä frequency and the distance between the jets on the average altitude of the plume is shown in Figure 1-13 for  $t = 5\tau_0$ , i.e., before the onset of the Crow instability. Two zones are clearly distinguished: one where the plume has remained or returned to the flight altitude and one where the plume has descended with the vortices. In the latter case (blue area in the figure), it is in a warmer atmosphere, which is favorable to less condensation. The values of  $\bar{N} = N\tau_0$  encountered in the atmosphere at flight altitude are generally between 0.3 and 1.5. The figure shows the position corresponding to the geometry of an A321 Neo. This geometry is far from optimal for this altitude criterion for most of the possible stratification values. The value of  $b_{jet}/b_0$  most favorable to a plume descent is between 0.8 and 1.2  $b_0$ , i.e., an engine close to the wingtip. These results should be contrasted against those obtained by Sussmann and Gierens (2001) who compared the contrails lifetime between a 2-engine and a 4-engine aircraft. They found that the contrails of a 4-engine aircraft always survive the vortex phase, compared to the contrails of the 2-engine aircraft, which can be short lived. Investigating the various mechanisms that could explain this difference, they report a small influence of the lateral position of the jet engine, unlike our present study.

Sometimes the Crow instability does not trigger during the evolution of the wake. One can then look at the altitude of the plume for longer times. Figure 1-14 represents the average altitude (taken as the barycenter of the jet concentration field) of the plume for  $t = 8\tau_0$ . The conclusions are the same and the difference between the two regimes described above is reinforced.

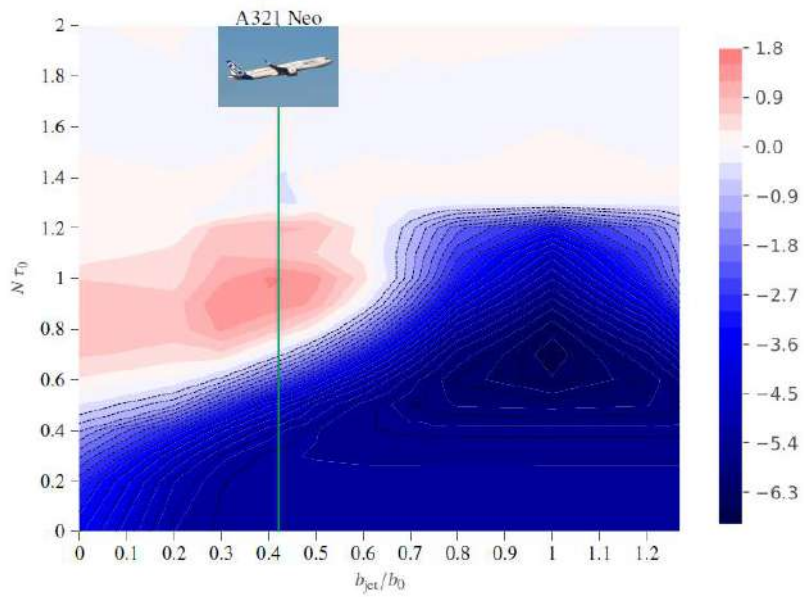


Figure 1-13: Average plume altitude as a function of  $b_{jet}/b_0$  and  $\bar{N} = N\tau_0$  at  $t = 5\tau_0$ . The position corresponding to the geometry of an A321 Neo is indicated.

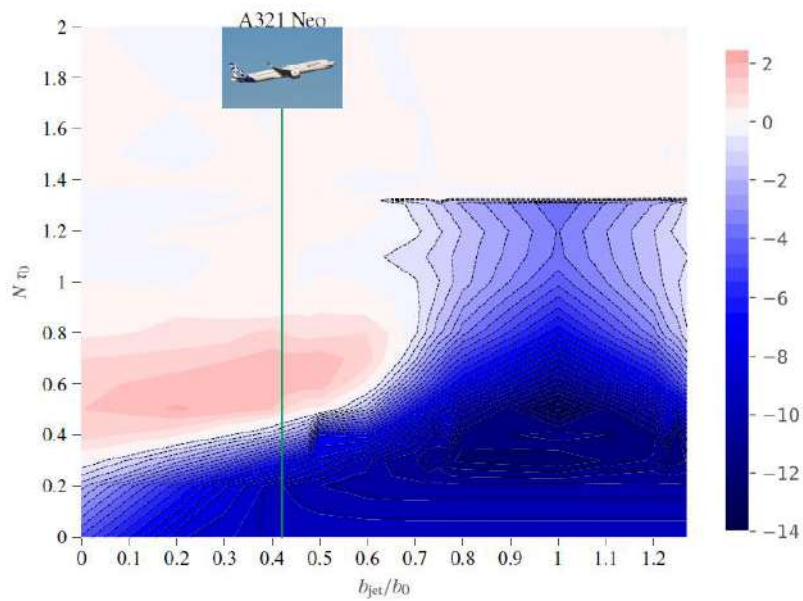


Figure 1-14: Average plume altitude as a function of  $b_{jet}/b_0$  and  $\bar{N} = N\tau_0$  at  $t = 8\tau_0$ . The position corresponding to the geometry of an A321 Neo is indicated.

## 1.4. WP 1.4: Evolution of contrails at intermediate scales

Contributors: Nicolas Bonne (ONERA), Aurélie Bouchard (ONERA), Magalie Buguet (ONERA)

The first objective of work package 1.4 is to set up a simulation methodology for the intermediate scales that cannot be calculated with the spatial and stationary simulation approaches (Reynolds Averaged Navier-Stokes, RANS) used for the near field immediately downstream of the aircraft. One will need to identify the characteristics of the contrails, beyond their initial formation phase and the disappearance of the disturbance generated by the aircraft, which will make it possible to define the parameterizations of the properties of the contrails in the climate models. A second objective is to interface with the near-field RANS simulations to consider all the physics of the jet regime in the calculation of the development of contrails at intermediate scales. This is to better understand the influence of the near field and the aircraft configuration on the large-scale properties of the contrail, an influence that remains poorly understood.

### 1.4.1. *Analysis and synthesis of simulation methods*

Task 1.4.1 is composed of two parts. The first contains the analysis of existing methods for the simulation of the aging of contrails. The second part deals with the different way plans to define the chain of simulation of contrail at the intermediate scale. A discussion of the impact of different methods on the obtained results is outside the scope of this analysis. As described more precisely in the following subsections, the simulation of the contrails evolution at intermediate scale relies on the use of atmospheric models. Consequently, in a first time, a reminder on atmospheric modeling is done with a focus on specific limited-area modeling.

#### 1.4.1.1. *Atmospheric modeling*

The simulation of a contrail spreads over different spatial and time scales. Indeed, the evolution of the aircraft wake to a contrail cover different stages, which must be simulated with different spatial and temporal resolution, from 1 m and 1 s for the vortex regime to 1 km and several minutes (or even one hour) for the diffusion stage. Many studies have highlighted the importance of the environment in the development of the contrail (Jensen et al. (1998), Paoli and Shariff (2016), Kärcher (2018), Schumann and Heymsfield (2017), Unterstrasser and Gierens (2010a, b), Unterstrasser et al. (2016)). With time, the influence of the aircraft decreases, and the influence of the meteorological conditions become essential. For example, during the dissipation regime, the presence of wind shear will affect the dispersion of the contrail. From a thermodynamic point of view, the magnitude of the relative humidity will play a role in the creation of ice particles (mainly the air saturation in respect of the ice) and the development of the contrail. We can also mention the impact of the turbulence magnitude on the life span and the impact of the radiative transfer.

In the TC2 project (final report of TC2 project (2015)), it appears that the turbulence magnitude impacts the lifetime of the vortex but has only a small impact on the amount of ice formed in the contrail. It appears too that the speed of creation of ice in contrails significantly depends on humidity (just after the optimum instability of the vortex) (Picot et al. (2015)). Around 20 minutes after the contrail formation, radiative transfer is effective, and the turbulence has no more significant role on the evolution of the contrail.

Consequently, to perform the simulation of the contrail at the intermediate scale, covering the diffusion and dissipation regime, the use of an atmospheric weather model is important and required.

Numerical weather prediction (NWP) models are based on the resolution of the time variation of the fluid mechanics equation adapted to the atmosphere, which is considered as a fluid. The main equations governing the evolution of the atmosphere are the conservation of momentum (the Navier-Stokes equation adapted to the

atmosphere), the continuity equation (conservation of mass), the thermodynamics equation (conservation of energy), the equation of state (linking pressure to virtual temperature), and the equation of conservation of specific humidity. These equations govern the space-time evolution of the model prognostic variables: wind components, potential temperature, pressure, and density. Some models like the Méso-NH model (Lafore et al. (1998)) also have the humidity mixing ratio for the different kind of hydrometeor (ice, graupel, water vapor, snow ...) and the turbulence kinetic energy (noted TKE) as the prognostic variables. The equations mentioned above cannot be solved analytically, so are discretized on a grid and approximate solutions are obtained. Importantly, models use a slightly different set of equation linked to different applications or different choices of discretization or physical process.

In meteorology, two kinds of NWP models have been developed to simulate the time evolution of the atmosphere: the global model and the limited-area model. In both cases, processes that are very small or too complex are simulated via parametrizations where small processes are related to variables that the model resolves. For example, in the limited-area Weather Research and Forecasting model (noted WRF; Skamarock et al. (2019)), the LES (Large-Eddy-Simulation) scheme should be applied for a resolution less than 100 m, whereas no cumulus scheme is needed with a resolution less than 10 km. On the contrary, for most global NWP models, the spatial resolution, which can reach  $0.1^\circ \times 0.1^\circ$  or  $0.25^\circ \times 0.25^\circ$  in the Global Forecasting Model (GFS) developed by NCEP (Yang et al. (2006)) or the Action Recherche Petite et Grande Echelle (ARPEGE) developed by Météo-France and the European Centre for Medium-Range Weather Forecast (Courtier et al. (1991)), implies the use of physical schemes for all physical processes not resolved, including clouds. Consequently, only limited-area models resolve the physical processes describing the contrail evolution at the intermediate scale without using physical parametrizations.

In the framework of the contrail study, global models have been used mostly to study environmental conditions (Haywood et al. (2009)). Different models use the outputs of NWP models, supplying an estimation of the ambient meteorological condition in input of contrail prediction tool. We can cite, for example, the Contrail Cirrus Prediction tool (noted CociP) developed by Schumann (2012), the logistic regression model detailed in Duda et al. (2009) or forecasting method based on the identification of contrail forming area (Carleton et al. (2008)). Furthermore, global models extended by parametrizations (like Global Climate Models) can simulate line-shaped contrail (Rap et al. (2010), Burkhardt and Kärcher (2011)) in order to study their environmental impact (see also Section 1.5).

Limited-area models (LAMs) cover only a limited geographical area. LAMs need boundary conditions provided by global models at different time during the simulated period. At kilometeric resolution, LAMs are close to Cloud Resolving Models (CRM). One of the main advantages of the LAM is grid nesting, as illustrated on Figure 1-15. The nesting concept is associated to one-way or two-way options where information is transferred between the parent and the child(s) domain(s). The use of multiple domains with different time and space scale allows adapting the physical scheme to activate and obtain a better simulation. Among the different limited-area model, we can cite the models: Méso-NH, WRF, MM5, AROME or ALADIN-NH, which are frequently used in the atmospheric community. For the present study, we focus on the two open-source models: Méso-NH and WRF model. Both models can be run in ideal or real mode. The ideal mode allows simulating an idealized atmosphere and has been used in older studies as Paugam (2008) for the simulation of the vortex phase. The real mode allows simulating real state of the atmosphere using output of global models for boundary conditions. This second mode helps to simulate the time evolution of the contrail for the dissipation and diffusion stage in a real atmosphere.

- Nesting in limited area model

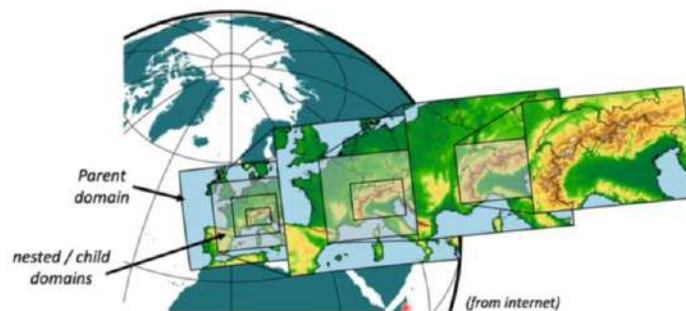


Figure 1-15 : Principle of grid-nesting (Wei Wang, Mesoscale and Microscale Meteorology Laboratory, NCAR, WRF tutorial 2022).

The Weather Research and Forecasting (WRF) modelling system has been developed by a collaborative partnership of the National Center for Atmospheric Research (NCAR), the National Oceanic and Atmospheric Administration from the National Centers for Environmental Prediction (NCEP), the U.S. Air Force, the Naval Research Laboratory (NRL), the University of Oklahoma and the Federal Aviation Administration (FAA). This model is used both for atmospheric research and operational forecasting application (Skamarock et al. (2019)), replacing the MM5 (5<sup>th</sup>-generation Pennsylvania State University-National Center for Atmospheric Research (PSU-NCAR) Mesoscale Model). WRF is a compressible, non-hydrostatic finite difference model. Past contrail studies using WRF or MM5 include Mazon (2016), comparing contrail simulations geostationary satellite observations and Stuefer et al (2005), describing a method to forecast contrails at the diffusion stage (resolution of 45 km) in the MM5 model.

The Meso-NH Atmospheric Simulation System (Lafore et al (1998), Lac et al (2018)) has been developed by the Centre National de Recherches Météorologiques (CNRM; Météo-France) and the Laboratoire d'Aérodynamique (Laero). In addition to the non-hydrostatic assumption, the anelastic assumption (pressure becomes a diagnostic variable) is applied in the model. Unlike the WRF model, which is used as a forecast tool, Méso-NH is mainly used for research on mesoscale atmospheric studies. Méso-NH has been used for simulating the aging of contrails for many years through the work of the CERFACS team composed by Daniel Cariolle, Roberto Paoli and Ronan Paugam (2008, 2010, 2016...). They coupled the solver NTMIX to simulate the vortex regime and the Méso-NH to simulate the evolution of the contrail after the vortex stage. More details on these methods are given in the section 1.4.1.2.2.4.

The main differences between WRF and Méso-NH are summarized in Table 1. For simulating contrails, the advantage and inconvenient of the use of these models are the following:

- the nesting principle is available in both models.
- in comparison to Méso-NH, WRF has not been used to simulate specific stages of contrail lifetime like the vortex regime or the dissipation stage. So, the feasibility of the approach for the simulation is not guaranteed.
- Méso-NH seems to have more flexibility to add an idealized wind perturbation like the Lamb-Oseen vortex. However, the WRF model is more flexible within a restart mode based on intermediate file, available in netCDF format and at each time step defined by the user.
- the surface schemes are externalized in the SURFEX platform (Masson et al. (2013)).

The final choice between the two models will be done based on the feasibility of the coupling of the NWP model and the output of the vortex regime simulation (obtained either by another LAM simulation or by a near-field RANS simulation).

Table 1 : Main characteristics of WRF and Méso-NH in the framework of the contrail simulation.

Mode I	Input for idealized mode	Compressible/incompressible	Surface coupling	Restart option	Advection scheme & Numerical schemes	Parametrization scheme
<b>WRF</b>	Predefined cases with sounding defined by the user.	<ul style="list-style-type: none"> <li>• Compressible</li> <li>• Non-hydrostatic</li> <li>• There is a run-time hydrostatic option.</li> </ul>	Database and information present in the global model output.	Yes, from a specific date.	Arakawa-C grid. Time: 3 order Runge Kutta Space: 5 <sup>th</sup> order WENO	<ul style="list-style-type: none"> <li>• Radiation (longwave and shortwave)</li> <li>• Surface</li> <li>• Planetary boundary layer</li> <li>• Turbulence/ Diffusion</li> <li>• Cumulus parametrization</li> <li>• Microphysics</li> </ul>
<b>Méso-NH</b>	<ul style="list-style-type: none"> <li>• Sounding</li> <li>• Stratified atmosphere with the Brunt Väisälä frequency.</li> <li>• Analytical 3D field</li> <li>• Possibility to add a perturbation.</li> </ul>	<ul style="list-style-type: none"> <li>• Non-hydrostatic Anelastic model</li> <li>• Pseudo-incompressible</li> <li>• For idealized case, possibility to use the Boussinesq approximation to reach the incompressibility (adapted to boundary layer).</li> </ul>	The SURFEX model (Vegetation, town, sea, lake).	Yes, from a segment. A segment can cover multiple time steps.	Arakawa-C Grid. Time: 4th order Runge-Kutta. Space: 5 <sup>th</sup> order WENO (Lunet, 2017)	<ul style="list-style-type: none"> <li>• Radiation</li> <li>• Turbulence</li> <li>• Shallow convection</li> <li>• Microphysical scheme for warm cloud and atmospheric ice</li> <li>• Electrical scheme</li> <li>• Wind turbine parametrization</li> </ul>

#### 1.4.1.2. Methods of contrail simulation

Simulating contrail development is very challenging because several temporal scales (few seconds to 1 hour) and spatial (few meters to ten kilometers) scales take part in the process. Most of past simulations were focused on one or two step(s) of the development like the jet phase, or the coupling between the jet and the vortex phases. Other studies focused instead on the diffusion phase. Nonetheless, many studies have been led in the past on the simulation of the development and the aging of the contrails. Among them, a number of the methodologies stand out. The aim of this section is to present a summary of the main methods found in the literature, distinguishing the simulation of young contrail from methods covering different stages of the contrail lifetime, including diffusion and dissipation stage.

##### 1.4.1.2.1. Simulations of young contrails in vortex regime

This section is dedicated to the simulation of the second stage of life of the contrails between ~10 s and 100 s. Despite the fact that during that stage, contrails are still young, this can be the stage during which the transition

between the near field and the far-off field could be made. The published simulations presented in the following subsection focus on the works of the DLR and IFU teams based on two codes: MESOSCOPE and EULAG.

1.4.1.2.1.1. Simulations of the first contrail stages with MESOSCOPE

This section focuses on the simulations of the contrail lifetime during the vortex regime (~ 10 s to 100 s) by Klaus Gierens and Ralf Sussman (Gierens (1996), Sussman and Gierens (1999), Sussmann and Gierens (2001)). The simulations were performed with the hydrodynamics code MESOSCOPE (Schumann et al. (1987)) coupled with a spectrally resolving cloud microphysics model developed at NASA (Jensen et al. (1994)). Sussmann and Gierens (1999) assume that ice crystals are the only class of particles present (i.e., no ambient aerosols, no liquid droplets) and the only microphysical process considered is the condensational growth of ice crystals or the evaporation. Sussmann and Gierens (2001) included the possibility of a decreasing number of ice crystals under sublimation conditions. They used a bulk microphysics code with a lognormal ice crystal mass distribution. The velocity field that constitutes the initial vortex pair of a wide-body four-turbofan aircraft was from Garnier et al. (1997). It is a vortex pair of a B-747 cruising at 10 km altitude at a speed of 250 m/s. The computed circulation of each vortex is 540 m<sup>2</sup>/s. All the initial fields correspond to plume age of 21 s. For the initialization of the microphysical fields, ice saturation is assumed inside the vortex pair. The total water content in this region consists of the background humidity (that is partly entrained into the plume and partly sucked through the engines), plus the water vapor formed by the combustion of kerosene. All the moisture above ice saturation is assumed to form the ice crystal population in the plume.

The base configuration is represented on Figure 1-16. The 2-D domain is 400 m × 800 m (cross section × altitude). The spatial resolution is 4 m. The altitude range is 9.5 km to 10.3 km and the contrail is formed at 10.17 km. The vertical profiles of temperature and wind speed are obtained from research aircraft measurements. The ambient relative humidity is treated as a free parameter and taken to be constant in the model domain. Atmospheric or aircraft-induced turbulence is ignored. The time step is 0.15 s and the duration of the simulation is 150 s (i.e., 171 s plume age). It has to be short because of the high swirling velocities in the vortices. This is already a stage (the so-called dispersion regime) when vortex breakdown, due to Crow instabilities or vortex bursting has occurred (Crow (1970), Chevalier (1973), Spalart and Wray (1996)). These 3-D effects cannot be observed in this 2-D simulation.

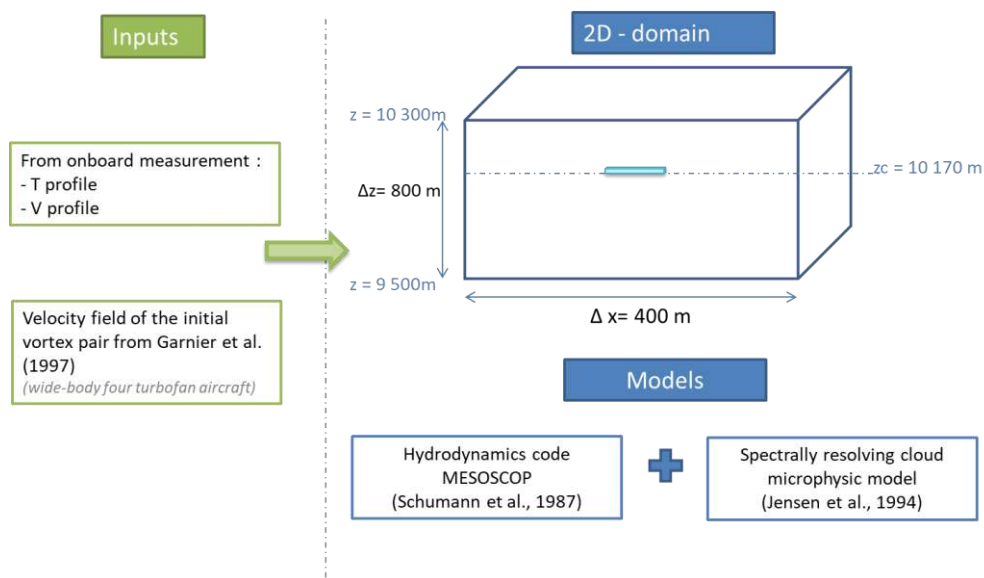


Figure 1-16 : Sketch of the simulation realized by Sussmann and Gierens (1999).

#### 1.4.1.2.1.2. Simulations of the first contrail stages with EULAG

This section focuses on the simulations of the contrail lifetime during the vortex phase or even younger through the work of Simon Unterstrasser's team (Unterstrasser et al. (2008), Unterstrasser et al. (2014), Unterstrasser and Stephan (2020)) using a model called EULAG.

The EULAG model (Smolarkiewicz and Margolin (1997), Smolarkiewicz, et al. (2014)) is a non-hydrostatic anelastic LES model, which employs the positive definite advection scheme MPDATA (Smolarkiewicz and Margolin (1998)). MPDATA is an iterative advancement of the fundamental upstream differencing method minimizing its dispersiveness. The horizontal direction  $x$  is along wingspan and  $z$  is the vertical coordinate. The computation of eddy viscosity uses Smagorinsky's closure. In their study, the code EULAG is coupled with the Lagrangian Cirrus Module (noted LCM), which is a Lagrangian ice microphysics code (Solch and Karcher (2010), Unterstrasser and Sölch (2014)). LCM comprises explicit aerosol and ice microphysics for simulating pure ice clouds like natural cirrus or contrails.

For the 2-D simulation of the vortex phase by Unterstrasser et al. (2008), the calculation of the ice microphysics is based on a parameterization developed by Spichtinger and Gierens (2009) instead of the LCM code. This parametrization of bulk microphysics is based on a consistent two-moment scheme (i.e. prognostic equations for ice crystal mass concentration and number density). They do not use explicit ice nucleation (as e.g. homogeneous nucleation) in the vortex but they prescribe the ice crystal number density and the ice water content at the start of the simulations. The large eddy simulations have been carried out with the EULAG model. The study focuses only on the vortex phase of the contrail evolution. The simulation starts at a plume age of about 20 s, when the vortex roll-up is completed and the temperature of the exhaust jets has relaxed to ambient values (Gerz and Ehret (1997)). The base configuration is represented on Figure 1-17. It is a domain with a horizontal extent (transverse direction) of 256 m, a vertical extent of 500 m, with a 1-m resolution in each direction. The simulations stop after 160 s and the time step is 0.02 s. A large aircraft (type: A340/B777) with wingspan of 60 m ( $b_{span}$ ) is located at the cruise altitude of 400 m. The real height of the flight level is determined by the choice of temperature at cruise altitude. The body of the plane is in the middle of the domain. The engine exits are 20 m to the left/right of the plane body. The simulation starts at the beginning of the vortex phase, so it is assumed that the vortices have fully rolled up and each vortex can be initialized with a Hallock-Burnham profile of tangential velocity ( $v_\theta$ ):

$$v_\theta(r) = \frac{\Gamma_0}{2\pi r} \frac{r^2}{r^2 + r_c^2}.$$

where the critical radius  $r_c$  is chosen to be 4 m and the initial circulation  $\Gamma_0 = 650 \text{ m}^2/\text{s}$ .

The horizontal separation distance of the two vortex centers is:

$$b_0 = \frac{\pi}{4} b_{span}.$$

The ice crystals are assumed to be uniformly distributed in 20-m circles centered at the vortex cores. The authors considered low to moderate supersaturation up to 20 %. The (ambient) turbulence is characterized in terms of eddy dissipation rate  $\varepsilon = 3.5 \times 10^{-5} \text{ m}^2/\text{s}^2$ , which represents an atmosphere with light turbulence following the turbulence classification of Sharmann et al. (2005).

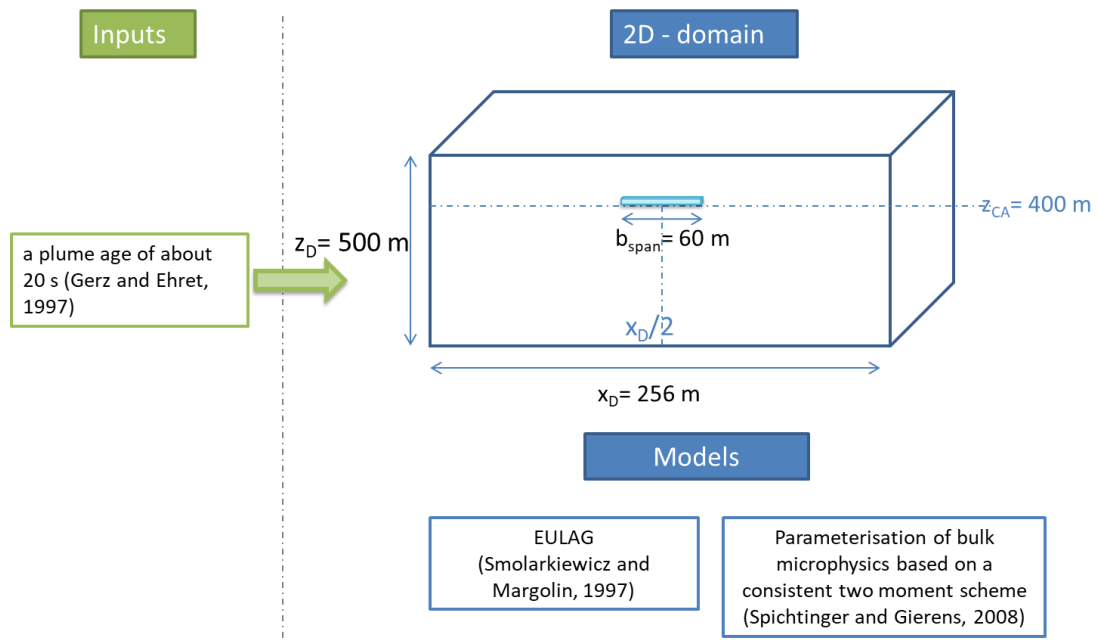


Figure 1-17 : Sketch of the simulated domain by Unterstrasser et al. (2008) with the position of the plane.

For the 3-D simulation of the vortex regime (first 5 minutes) realized by Unterstrasser (2014), LCM is used (EULAG-LCM, Sölch and Kärcher (2010)) to describe the ice microphysics. The sketch of the 3D simulation is given on Figure 1-18. It comprises explicit aerosol and ice microphysics. In this work, deposition and latent heat release are the only microphysical processes switched on. Turbulent fields are generated in a priori runs for prescribed stratification and eddy dissipation rate. These are superimposed with a counterrotating vortex pair.

The dimensions of the model domain are  $L_x = 384$  m (transverse direction),  $L_y = 400$  m (the flight direction – longitudinal) and  $L_z = 600$  m (vertical direction). The grid resolution is 1 m along the vertical and transverse direction ( $z$  and  $x$ ) and 2 m along the flight direction ( $y$ ). Periodic boundary conditions are applied in the horizontal and rigid boundaries in the vertical. The latter means that all the three components of the velocity are null at the top and bottom layers. The simulations were run until 300 s. The time step is initially 0.03 s and increases to 0.1 s at later stage of the simulation. The initialization of the simulation is realized with a Lamb-Oseen vortex, with core radius of 4 m and an initial circulation of  $520 \text{ m}^2 \cdot \text{s}^{-1}$  at  $z = 500$  m. The vortex separation distance  $b_0$  is 47.3 m and corresponds to an aircraft with wingspan of 60 m (type: A340/B777). The domain length  $L_y$  is chosen such that the formation of the most unstable Crow mode ( $\sim 8.6 b_0$ ) can be triggered (Crow (1970)). A further sensitivity simulation with  $L_z = 800$  m shows that the default domain height and the distance of the vortices from the top and bottom boundaries is large enough to avoid spurious boundary effects. A calm atmosphere is represented: the Brunt-Väisälä frequency is  $1.15 \cdot 10^{-2} \text{ s}^{-1}$  and the eddy dissipation rate of the ambient turbulence field is  $10^{-7} \text{ m}^2 \text{ s}^{-3}$ . It is assumed that the initial ice crystals contain exactly the amount of the water vapor emitted due to fuel burning.

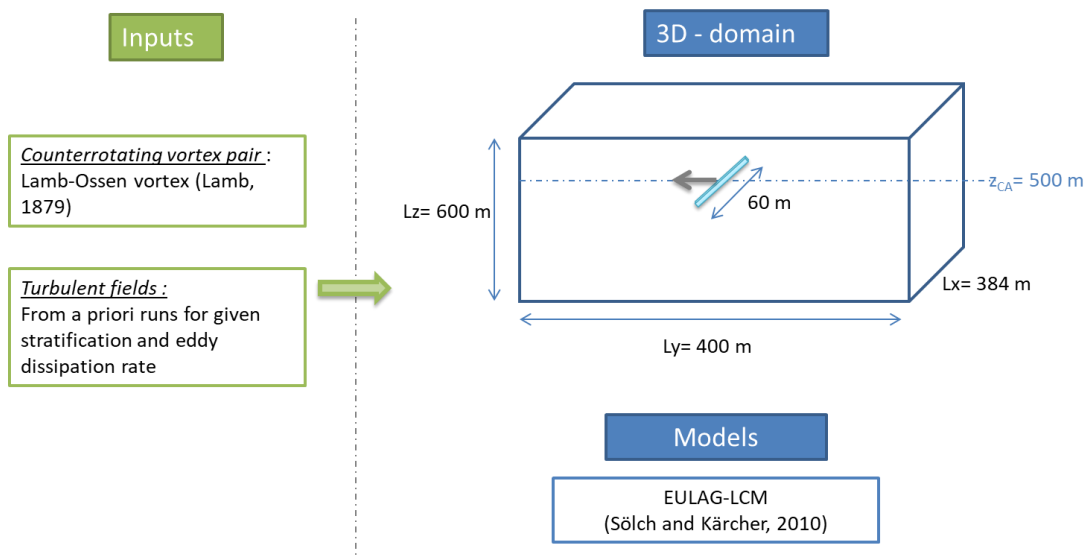


Figure 1-18 : Sketch of the simulated domain by Unterstrasser (2014) with the position of the plane.

#### 1.4.1.2.2. Simulations from the vortex regime to the diffusion regime

In this section, we focus on the studies that, in addition to dealing with the vortex regime, also simulate the more advanced phases of contrail aging, e.g., dissipation regime (between 100 s and around 1000 s) and the diffusion regime (from 1000 s to few hours). The different models presented in the previous section have been adapted to simulate the contrail at different stage. Thus, the adaptation of MESOSCOPE and EULAG-LCM are presented in the present section. In addition to this method, methods based on the LES wake model and Mésos-NH model are detailed.

##### 1.4.1.2.2.1. Simulation with MESOSCOPE

In the continuity of the work of Gierens and Sussman (Section 1.4.1.2.1.1), the MESOSCOPE model coupled with the Ames Aerosol Model has been applied to the study of the contrail to cirrus transition (Gierens and Jensen (1998)). The same aircraft configuration has been used for the simulation. As detailed in Gierens and Jensen (1998), the 2D-simulation has been performed in two steps: the vortex phase until 150 s followed by a dispersion phase until 30 min. The simulation of the vortex phase is the same as the simulation used in Sussman and Gierens (1999), except that the size of the domain is  $400 \text{ m} \times 400 \text{ m}$  instead of  $400 \text{ m} \times 800 \text{ m}$  in the Sussman and Gierens (1999).

At the end of the first simulation, the fields obtained, corresponding to the end of the vortex phase, are smoothed to a resolution of 16 m (instead of 4 m in the first simulation) and transferred to a larger domain of  $3200 \times 1600 \text{ m}^2$ , extending up to 11.5 km. The fields obtained after the smoothing are then used as the initial state of the second simulation. For the simulation of the dispersion phase, a time step of 1 s has been chosen by the authors. It is important to note that periodic boundaries are used in the span direction. It can be noted that only ice crystals as hydrometeor are considered in the simulation, with the diffusional growth and evaporation of ice crystal as processes.

#### 1.4.1.2.2.2. Simulations with EULAG-LCM

Simulations of the dissipation and diffusion phases (Unterstrasser (2020)) use, as in the previous section, the EULAG-LCM model (Smolarkiewicz and Margolin (1997), Smolarkiewicz et al. (2014)). For the high-resolution simulations of contrail-cirrus realized by Unterstrasser (2020), the simulation for a single aircraft starts with a 5- minutes old contrail at a time when aircraft wake vortices decayed and the initial contrail data are provided by Unterstrasser and Stephan (2020), where the vortex phases is simulated by using the EULAG-LCM model. The simulated time covers 8 hours of the contrail-cirrus life cycle. To reduce the complexity of the simulations, and simplify their interpretation, several LCM components are switched off (like heterogeneous nucleation, aggregation, and radiation).

A 2-D model, whose domain is perpendicular to the direction of the flight and represents some portion of the UT/LS (upper tropospheric/lower stratospheric) region, is used. In the vertical direction ( $z$ ), the domain dimension is 2.5 km, in the horizontal direction ( $x$ ), the domain dimension is 40 or 80 km, depending on the strength of the vertical wind shear (higher wind shear leads to broader contrails). Uniform grid boxes with sizes  $dx = dz = 10$  m span a regular Cartesian mesh. The base configuration is represented on Figure 1-19. As mentioned before, the total simulated time is 8 h and the dynamical time step  $\Delta t_{\text{dyn}}$  is 2 s or 1.25 s, depending on the vertical wind shear; and the nucleation step  $\Delta t_{\text{nuc}}$  is 0.4 s. It can be noted that nucleation is turned on only in simulations with  $t_{\text{dyn}} = 2$  s. The type of aircraft is A340/B777 (wingspan of around 60 m). In the computational domain, the aircraft is at 1.5 km, in the middle of the ice supersaturated layer resulting in 600 m thick fractions of the ice supersaturated layer above and below cruise altitude.

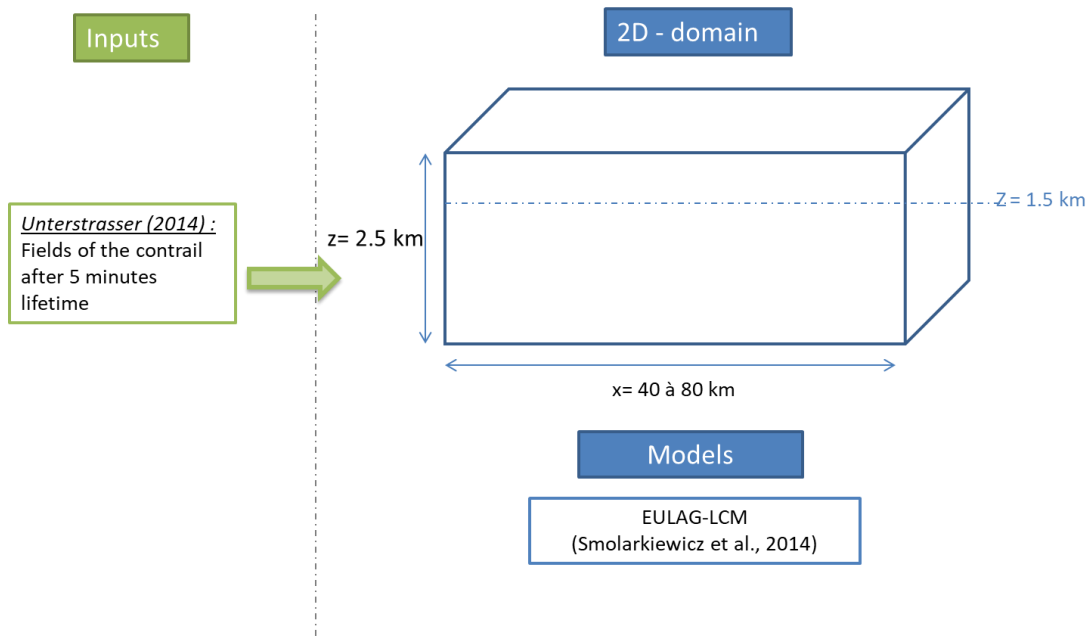


Figure 1-19 : Sketch of the simulated domain by Unterstrasser (2020). The inputs of the simulations are the outputs of the simulation represents on Figure 1-18.

In input, the vertical temperature profile used corresponds to a stably stratified atmosphere (they consider a typical value in the upper troposphere of  $N_{bv} = 10^{-2} \text{ s}^{-1}$ ). Background turbulent velocity fields are taken from a-priori simulation and have a root mean square value of:

$$\hat{u} = \sqrt{\sum_i (u_i^2 + w_i^2)} \approx 0.12 \text{ m} \cdot \text{s}^{-1}$$

Even without any turbulence forcing mechanism,  $\hat{u}$  does not drop below  $0.1 \text{ m s}^{-1}$  and the turbulence intensity is quasi-constant over the simulated period.

To incorporate the vortex phase simulation data in the model domain, the Eulerian 3D data from the works of Unterstrasser (2014) (e.g., velocity (u, w), perturbation of water vapor concentration  $q_v$ , and potential temperature  $\theta$ ) are averaged along flight direction and interpolated on the coarser grid and embedded into the enlarged 2D model domain.

#### 1.4.1.2.2.3. Simulation with the LES wake model

The large eddy-simulation (LES) wake model used for studies of wake dynamics, wake-plume chemistry, and contrails is described in Lewellen and Lewellen (1996, 2001). A 3D finite-difference implementation of the incompressible Navier–Stokes equations is employed, second-order accurate in space and time, with a direct solver for the pressure and a variable time step (Lewellen (2014)). The piecewise parabolic method (PPM) is used for advection of the liquid-ice potential temperature, total water mixing ratio, ice number densities, and passive species concentrations. The subgrid model uses a quasi-equilibrium second-order turbulence closure scheme with a prognostic equation for the subgrid TKE and diagnostic equation for the subgrid turbulence length scale.

This model has been used for exploring aircraft wake and contrail dynamics, from the period beginning several wingspans behind the aircraft, after ice crystal formation, through to contrail demise possibly many hours later (Lewellen and Lewellen (1996, 2001), Lewellen et al. (2014), Lewellen (2014)).

In Lewellen et al. (2014), the simulations are based on the study of the contrails generated by a B-767 aircraft, with wingspan of 47.25 m and flight speed of 273 m/s at altitude of 10.7 km and a total circulation in the wake of 391  $\text{m}^2/\text{s}$ . The 6 domains and grid resolution used to simulate the different time periods and stage of the contrails are listed in the Table 2 and illustrated in the Figure 1-20. Periodic copies are used to extend from the smaller to larger downstream domain and an ambient-turbulence field added. The simulations are initialized from 2D Boeing wake rollup calculations (Czech et al. (2005)) from two steps:

- an initial high-resolution short domain run without ice for the early turbulent spread of the exhaust jet.
- then the introduction of the ice crystals distributed spatially like an exhaust tracer species is done.

In Lewellen (2020), a 300-s young contrail is simulated for a smaller aircraft based on the method developed in 2014 (same step sequence and periodic copies with smaller domains and higher resolution).

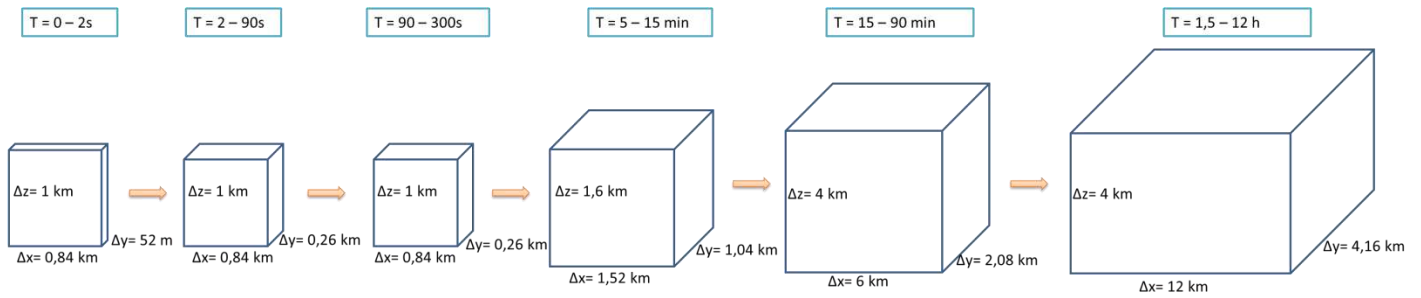


Figure 1-20 : Sketch of the simulations succession of 6 domains realized by Lewellen et al. (2014).

Table 2 : Grid parameters according to the time period used in Lewellen et al. (2014). Source: table 1 of Lewellen et al. (2014).

Grid	Time period	Domain ( $x \times y \times z \text{ km}^3$ )	Fine grid spacing ( $\Delta x \times \Delta y \times \Delta z \text{ m}^3$ )
1	0 – 2 s	$0.84 \times 0.052 \times 1$	$0.4 \times 0.4 \times 0.4$
2	2 – 90 s	$0.84 \times 0.26 \times 1$	$0.6 \times 2 \times 0.6$
3	90 – 300 s	$0.84 \times 0.26 \times 1$	$1.25 \times 1.6 \times 1.25$
4	5 – 15 min	$1.52 \times 1.04 \times 1.6$	$5 \times 4.8 \times 5$
5	15 – 90 min	$6 \times 2.08 \times 4$	$16 \times 16 \times 16$
6	1.5 – 12 h	$12 \times 4.16 \times 4$	$25 \times 28 \times 25$

#### 1.4.1.2.2.4. Simulations with Méso-NH

Several studies have been led to model. Most of the studies that simulate the aging of a contrail with Méso-NH used the NTMIX code (Paugam (2010), Picot et al. (2015), final report of TC2 project (2015), Paoli et al. (2017)) to simulate the vortex regime. The simulation outputs obtained are then used to initialize the Méso-NH model and simulate the far-off field and the contrail dissipation over a period of one hour.

An illustration of the works done by the CERFACS team is detailed through the TC2 project (final report of TC2 project (2015)). One of the aims of this project was to study the aging of the contrails from the vortex regime to the dissipation and diffusion regime. To simulate the vortex phase until the diffusion stage, the simulations are realized in two successive stages as illustrated on Figure 1-21. The first step focuses on the vortex and dissipation regime (around 5 first minutes of the wake evolution after the jet regime), and the second step focus on the diffusion regime (wake evolution during the following hour).

The first step involves the simulation of the 5 first minutes of life of the contrail (from a few seconds after its formation). The first stage of this step is to extract a field of background atmospheric turbulence simulated with Méso-NH on a domain of 10 km along x and y axis (x being along the aircraft trajectory) and 4 km along the vertical axis, with a 10 m resolution. This background field is combined with an output field of a vortex from NTMIX model, with supersaturation of 130 % and a temperature of 218 K, to initialize the Méso-NH model on a domain of 400 m along x axis, 1 km along y and z axis, with a spatial resolution of 2 m. For the second step, the fields obtained in output of the 5 minutes lifetime contrail simulation are reintroduced as input to the first Méso-NH domain, containing the troposphere. As in Gierens and Jensen (1998), the data from the first step are copied using a periodic continuation along the contrail axis to fill the axial length of the first Méso-NH domain (Paugam (2008), Paoli et al. (2017)).

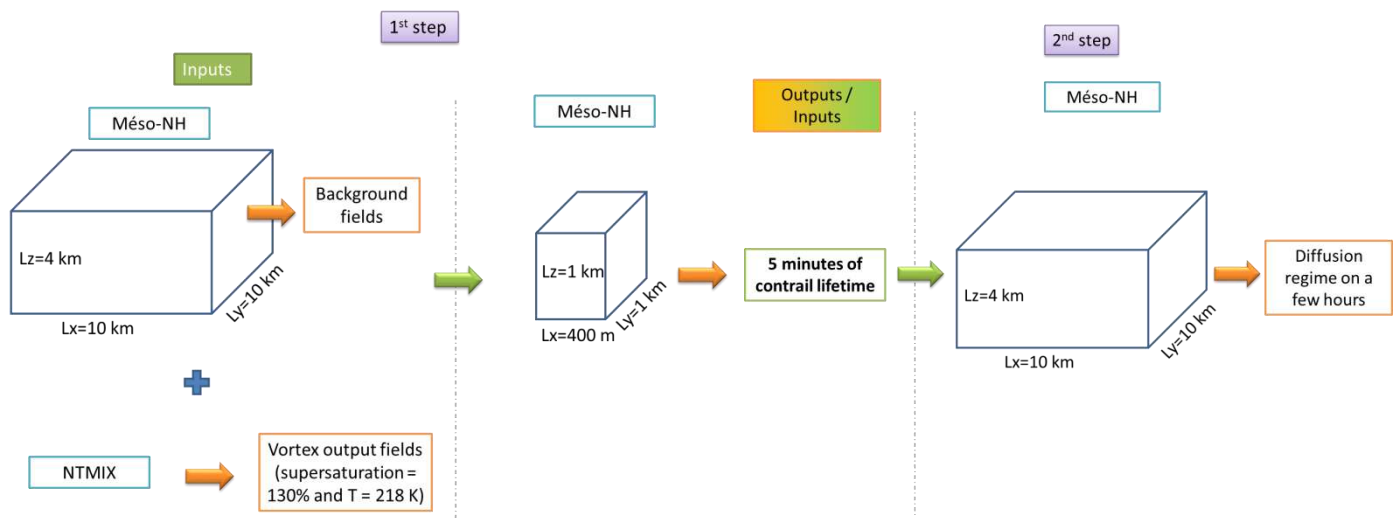


Figure 1-21 : Sketch of a simulation realized in the TC2 project to represent: in the first step the first 5 minutes of a contrail lifetime (vortex and dissipation regimes) and in the second step the diffusion regime (on a few hours of the contrail lifetime) (TC2 project, final report (2015)).

Some tests have been realized to test the influence of some process on the contrail evolution. For instance, to test the turbulence impact, the forcing scheme used is a method to generate a synthetic and stationary turbulence, with given statistic properties. This method is based on a spectral approach developed for the direct simulation of the turbulence (Eswaran et al. (1988), Paoli and Shariff (2009)). To obtain stable stationary conditions and avoid a decrease of the kinetic energy in time, the turbulence is maintained by exciting the bigger mods through the stochastic differential equations of kind of “Langevin”. The fluctuations of the smallest scales are then generated by an energy nonlinear cascade. This scheme has been coupled to the Mésos-NH model by introducing a force field in the Navier-Stoke equations. These forces are composed by sinusoidal waves of which the components evolve according to the Ornstein-Uhlenbeck process. This force field is also constrained to have a null divergence. The simulation domain is of  $4 \text{ km}^3$  with spatial resolution going to 2 to 10 m. The environment is stratified with a buoyancy frequency of 0.012 rad/s. The state of reference corresponds to an altitude of 11 km, typical of cruise flights of commercial aircrafts. In this configuration, 3 levels of turbulence have been tested and the results show that for low to moderate energy levels, a resolution of 4 m is necessary for that the energy spectrum does not depend on the spatial resolution. For high level of turbulence, a spatial resolution of 10 m is sufficient.

After 5 minutes of contrail evolution, the dissipation regime starts where the dynamic is led by the atmospheric turbulence. To represent this process, the domain used (in which the contrail is influenced by the stochastic turbulence) has to be bigger and the resolution has to be larger. For this phase, a domain of  $4 \text{ km}^3$  with a resolution of 10 m is used. The atmospheric turbulence has been created in this domain and the perturbation of the dynamic, chemical and ice crystals fields after 5 minutes are extracted from the small domain. After one hour of simulation, the vortex is transformed into laminar layers.

Based on a similar method, in Paoli et al. (2017), a 3D-simulation chain of contrail aging has been established based on the Mésos-NH model. The simulation focuses on the first hour of the lifetime of the contrail. The jet and vortex phases were computed in a small section of the simulation domain using ambient turbulence data and the contrail data at the end of the jet phase as initial conditions (Paoli et al. (2013), Picot et al. (2015)). The data of the vortex phase at the age of 5 min are copied using a periodic continuation along the contrail axis and interpolated back in the largest domain. Two runs of capability are done on the small domain ( $L_x = L_y = L_z = 4 \text{ km}$  with a resolution of 4 m) by using full 3D scheme to simulate the early phase of contrail-to-

cirrus transition with resolved atmospheric turbulence on a uniform grid resolution. Several runs of sensitivity are done on the larger domain ( $L_x = L_y = 10$  km and  $L_z = 5$  km with a uniform resolution of 10 m) to analyze how the radiative transfer and the atmospheric turbulence impact the contrail evolution.

#### 1.4.1.3. Summary of the different methods for the diffusion and dissipation stage

The Table 3 contains the summary of different key points of the simulations of contrail-to-cirrus transition discussed in section 1.4.1.2.

Table 3 : Summary of key points of existing simulation of contrail-to-cirrus transition.

Contrail stage of life covered by the simulation	Name of the method or model	References	Dynamics	Microphysics
From the vortex to the dissipation phase, corresponding to a simulation from 5 minutes to 40 min in Paugam (2010) and 1 h in Paoli et al. (2017).	Méso-NH	Paugam (2010), Paoli (2017)	Non-hydrostatic, anelastic model.	Different microphysics schemes are available.
From the vortex phase to the dissipation phase (from 5 min to 8 h)	EULAG-LCM	Unterstrasser (2020)	Non-hydrostatic LES model	Bulk ice microphysics.
All stage, until 4 h in the contrail lifetime.	LES Wake model	Lewellen (2014)	Quasi 3D fluid mechanism 3D finite difference Navier Stokes incompressible	Size resolved microphysics based on the CARMA code of the NASA.
From vortex to the dispersion phase (from 150 s to 30 min)	MESOSCOPI	Gierens and Jensen (1998)	2D-hydrodynamic code coupled with the Ames Aerosol Model	Ames Aerosol Model

This summary highlights that a lot of studies use the same model for the different stages of the contrail lifetime. Most of the models described here are based on LES schemes with different level of complexity. The important point is the difficulty to go from the simulation of the vortex regime to dissipation then diffusion regime. In most of these methods, data from the early stage are compressed, extrapolated, or smoothed from one stage to the other. The different methods assume that after the vortex regime, smoothing to a bigger resolution does not affect the results because the dynamic induced by the aircraft vanishes after the vortex phase (Gierens and Jensen (1998), Paugam (2008)).

#### 1.4.1.4. Towards simulating contrails at the intermediate stage

The simulation of contrails at the diffusion and dissipation stage is planned to be done in different steps. In a preliminary time, a chain of the simulation will be defined and tested, with idealized wind field. Then the output of the near-field RANS simulation will be used to simulate a more realistic contrail.

To test and establish the way to build the simulation, two idealized vortices will be simulated based on the Lamb-Oseen equations, which resolves the Navier-Stokes equations. It has been demonstrated that these

equations simulate well the vortex regime in the contrail life (Garnier et al. (1997), Hölzapfel (2002)). The simulation of these idealized vortices is then done by applying the method developed by Paugam (2008; 2010) where a small geographical domain is defined around the two vortices, with dimension less than 1 km in the three dimensions. The characteristics of the vortices are based on the reference case often used: the hypothesis of a B747 aircraft cruising at an altitude of 11 km. At the end of this preliminary test, we have an estimation of the state of the atmosphere where two counter rotating vortices are defined. At this step, we can assume that we are at the end of vortex regime in the contrail lifetime.

In a second step, one of the LAMs mentioned above will be used to simulate the evolution of the state of the atmosphere. First, a reference state of the atmosphere will be simulated based only on the LAM model used in real case with information from global model (like GFS) for the boundary conditions. This state will cover the whole troposphere in altitude and a few degrees in latitude and longitude. Then, a coupling will be done between the selected LAM and the vortices simulation obtained in the preliminary stage. At this stage, we will assume that the output containing the simulation of vortices corresponds to an area in the upper troposphere (around 10-13 km for middle latitude), corresponding to the altitude of flight of an aircraft.

In a final step, a grid-nested simulation is established. The nesting process available in the LAM will be used to simulate the contrail at different stages of its lifetime. Multiple runs will be done, using the principle of restart, where a child domain with specific parametrization and space and time resolution will be applied. These multiple simulations (one run after another) will be done to consider the specific evolution of the contrail and space and time resolutions for each phase of the contrail. The principle is illustrated on the Figure 1-22.

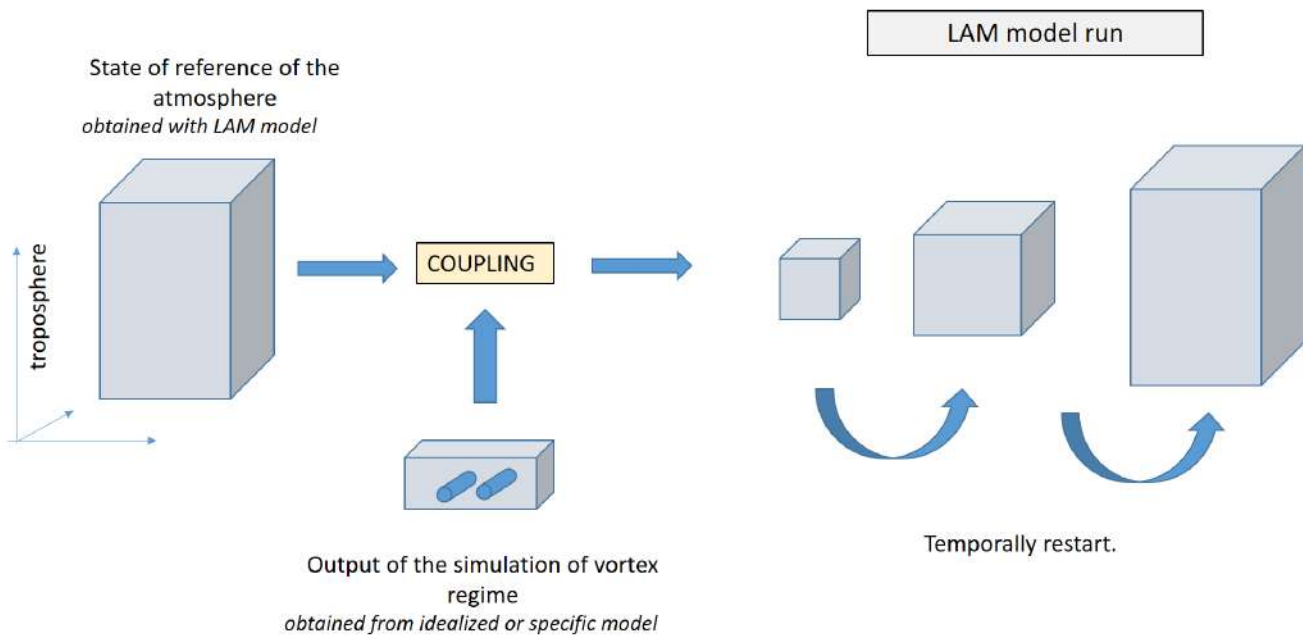


Figure 1-22 : Considered principle of the simulation of a contrail at dissipation stage.

Once the whole chain of simulation has been established, a second part of the work will focus on the coupling with the outputs of the RANS simulation, covering the first stage of the contrail lifetime (the jet and a part of the vortex regime) instead of the idealized vortex regime used until now (based on the Lamb-Oseen equations).

To realize this coupling, the outputs of one model will need to be converted to inputs of the next, including a mesh accepted by the LAM and all the essential meteorological parameters. Méso-NH does not accept an irregular horizontal grid. Moreover, a great attention should be given to the physical consistency between both simulations' codes. Different tests will be done to find the best time and the best discretization for the coupling. The RANS simulation input will at a minimum contain information on the velocity field, temperature, pressure, and information on different species. Special attention will be given to the ice mixing ratio and its evolution. The whole chain of simulation will be adapted in function of the results obtained during the first step.

#### 1.4.2. *Development of a simulation methodology for contrail ageing*

In addition to the tools presented in the previous section, the use of the ONERA's CEDRE code is also considered. This section describes the preliminary work and the first results that have been obtained.

##### 1.4.2.1. *Computational method*

As mentioned previously, the vortex phase is usually simulated assuming an idealized vortex pair such as Lamb-Oseen vortices with ice particle number and spatial distribution coming either from a dilution law (e.g., Unterstrasser and Sölch (2010), Unterstrasser et al. (2014)) or from a temporal LES simulation of the jet/vortex interaction (e.g., Paoli et al. (2013)). In these computations, different atmospheric effects are considered. For example, Unterstrasser and Sölch (2010) show the importance of relative humidity and temperature of the atmosphere on the surviving ice crystals in 2D simulations. Then Unterstrasser et al. (2014) show with 3D LES simulations the importance of stratification, turbulence and vertical wind shear on both surviving ice crystals number and their spatial distribution. Therefore, these parameters must be taken into account in our computations.

The first objective of this task is to simulate the vortex phase of a contrail. In this phase, the flow consists of two contra-rotating vortices as shown in Figure 1-23.

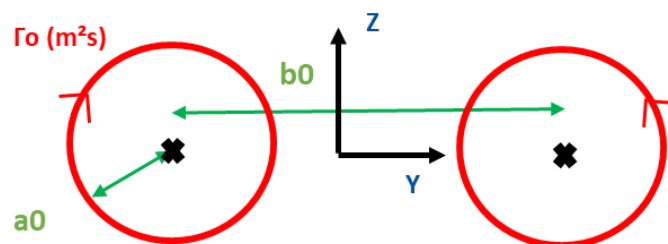


Figure 1-23 : Schematic view of a contra-rotating vortex pair.  $\Gamma_0$  is the circulation of a vortex  $a_0$  its radius and  $b_0$  the distance between the two vortices.

The methodology usually found in the literature (e.g., Unterstrasser and Sölch (2010), Unterstrasser et al. (2014), Paoli et al. (2013)) consists in 2D or 3D temporal LES simulations of a Lamb-Oseen contra-rotating vortex pair around which ice crystals will evolve. The ice crystals are tracked using a Lagrangian approach.

The following computations are made using the multiphysics code CEDRE that contains a multispecies reactive solver called CHARME and a dispersed phase Lagrangian solver SPARTE. These two solvers can be coupled to compute the sublimation or the growth by condensation of the ice crystal. Agglomeration of ice crystals can also be taken into account in SPARTE. However, this option has not been activated this year.

During this year the different phenomenon have been introduced one after each other beginning with a simple simulation of a contra-rotating vortex pair in a stratified atmosphere with or without shear. Then the humidity and ice crystal dynamic have been taken into account. The atmospheric turbulence has not yet been introduced therefore 2D DNS computations can be made.

#### 1.4.2.2. Computational domain and boundary condition

The computational domain is decomposed in two regions has shown in Figure 1-24. The first (in red) has a fine mesh with a cell size determined by the radius of the vortices and the Brunt Väisälä frequency  $\Delta y = \Delta z = \frac{a_0}{10}$  for low stratification to  $\Delta y = \Delta z = \frac{a_0}{40}$  for higher stratifications. Its height may depend on the Brunt Väisälä frequency, the descend velocity of the vortex pair and the wanted final time of the computation. This zone is surrounded by a zone where the cell size increases with increasing distance from the red zone. Its size has been chosen in order to guarantee the independence of the results with the boundary condition.

Boundary conditions are chosen as inflow boundary conditions with a recirculation option that can transform the inflow condition to an outflow one. Then the pressure and temperature are imposed as given by the hydrostatic solution at a given altitude. The velocity is almost zero far from the vortices, so it has been set to zero on the boundaries.

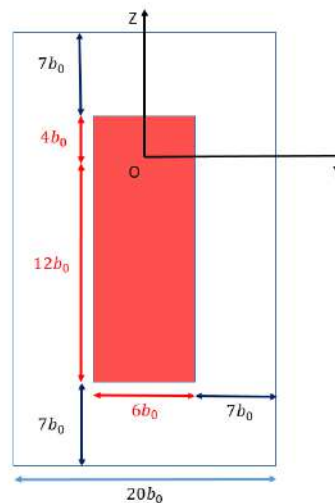


Figure 1-24: Computational domain

#### 1.4.2.3. Initialization

The stratification has been introduced in CEDRE computation by introducing the gravity field and by choosing the temperature and pressure field of the initial condition. These two fields can be found in Paoli et al. (2013) and in equations (1) and (2) below respectively. The velocity field of the vortices have been taken as Lamb-Oseen vortices which are represented by the first two right hand side terms of equation (3) and (4).

The shear effect has been introduced by superposition of the two Lamb-Oseen vortices velocity field and a small crosswind velocity with constant gradient. This perturbation is the third term in the right-hand side of equation (3). The left and right boundary conditions on velocity have been changed accordingly if the shear is not zero.

Finally, the initial condition reads:

$$T(z) = T_{ref} \left[ \frac{g^2}{N_{bv}^2 c_p T_{ref}} + \left( 1 - \frac{g^2}{N_{bv}^2 c_p T_{ref}} \right) e^{\frac{N_{bv}^2}{g}(z-z_{ref})} \right] \quad (1)$$

$$p(z) = p_{ref} \left[ \frac{g^2}{N_{bv}^2 c_p T_{ref}} + \left( 1 - \frac{g^2}{N_{bv}^2 c_p T_{ref}} \right) e^{\frac{N_{bv}^2}{g}(z-z_{ref})} \right]^{\frac{\gamma}{\gamma-1}} e^{-\frac{\gamma}{\gamma-1} \frac{N_{bv}^2}{g}(z-z_{ref})} \quad (2)$$

$$v(y, z) = -\frac{\Gamma_0}{2\pi} \frac{(z - z_1)}{(y - y_1)^2 + (z - z_1)^2} \left( 1 - e^{-\frac{(y-y_1)^2 + (z-z_1)^2}{2r_c^2}} \right) + \frac{\Gamma_0}{2\pi} \frac{(z - z_2)}{(y - y_2)^2 + (z - z_2)^2} \left( 1 - e^{-\frac{(y-y_2)^2 + (z-z_2)^2}{2r_c^2}} \right) + S(z - z_{ref}) \quad (3)$$

$$w(y, z) = \frac{\Gamma_0}{2\pi} \frac{(y - y_1)}{(y - y_1)^2 + (z - z_1)^2} \left( 1 - e^{-\frac{(y-y_1)^2 + (z-z_1)^2}{2r_c^2}} \right) - \frac{\Gamma_0}{2\pi} \frac{(y - y_2)}{(y - y_2)^2 + (z - z_2)^2} \left( 1 - e^{-\frac{(y-y_2)^2 + (z-z_2)^2}{2r_c^2}} \right) \quad (4)$$

where  $r_c$  and  $\Gamma_0$  are the radius and circulation of the vortices,  $(y_1, z_1)$  and  $(y_2, z_2)$  the position of right and left vortices respectively,  $z_{ref}$  the reference altitude with  $p_{ref}$ ,  $T_{ref}$  the pressure and temperature at the reference altitude.  $N_{bv}$  is the Brunt Väisälä frequency,  $g$  the gravity and  $S$  the shear coefficient. Humidity has been introduced as a constant water mass fraction:  $Y_{H_2O}(z) = Y_{H_2O}(z_{ref})$  where  $Y_{H_2O}(z_{ref})$  is computed with respect to a given ice relative humidity. Another choice could be made. One can impose that the relative humidity is constant in altitude for example. The first solution has been used for its simplicity. The second solution should be tested next year.

Finally, the initial spatial distribution of ice crystals is less consensual. For example, Unterstrasser and Sölch (2010) and Unterstrasser et al. (2014) initialized the ice crystal concentration with a uniform law in two discs centered around the vortex cores or with Gaussian distribution representing the jet. Unterstrasser and Sölch (2010) shows significant discrepancy between the two initialization methods whereas Unterstrasser et al. (2014) shows little difference. Another way to initialize the ice crystal spatial distribution is to use the result of a jet/vortex mixing simulation as shown by Picot (2013). This last method has not been used since the mixing jet/vortex will be done by a RANS computation in the final approach.

In the following, the ice crystals are initialized assuming a log-normal size distribution and a Gaussian spatial distribution centered on a circle around the vortex centers.

#### 1.4.2.4. Results without ice crystals

This part is dedicated to the validation of the vortex dynamic. Therefore, there are no ice crystals nor water vapor. The results from CEDRE have been compared with simulations made previously at ONERA with the Nek5000 code. It has to be emphasized that CEDRE solves the compressible Navier Stokes equation whereas Nek5000 solves the anelastic equation with Boussinesq approximation. Therefore, one can expect some

differences at higher time between the results. The Nek5000 computation will be referred to as the reference computation hereafter.

In this section, the vortex parameters are set to  $\Gamma_0 = 387.6 \text{ m}^2\text{s}^{-1}$ ,  $b_0 = 53.4 \text{ m}$ ,  $a_0 = \frac{b_0}{10}$ . With these conditions the vortex descent velocity is  $W_0 = 1.15 \text{ ms}^{-1}$ . The vortex time scale is  $\tau = 46.2 \text{ s}$ . The atmospheric conditions at the reference altitude follow ISA conditions at 11 km of altitude  $P_{ref} = 26437.25 \text{ Pa}$  and  $T_{ref} = 223.15 \text{ K}$ . The stratification has been varied from  $N_{bv}\tau = 0.1$  to  $N_{bv}\tau = 1$  which means from  $N_{bv} = 2 \cdot 10^{-3} \text{ s}^{-1}$  to  $N_{bv} = 2 \cdot 10^{-2} \text{ s}^{-1}$ .

Finally, different meshes have been tested to find the mesh convergence. Only the results on the fine mesh part cell size will be shown. Mesh characteristics are summarized in Table 4.

Table 4: Cell size for different meshes

Mesh Name	Mesh3	Mesh4	Mesh5	Mesh7
Cell size	$\frac{a_0}{10}$	$\frac{0.8a_0}{10}$	$\frac{a_0}{20}$	$\frac{a_0}{40}$

In the following, the results will be given in dimensionless quantity. The reference length is  $b_0$  and the reference time is  $\tau$ . The altitude of vortex center through time for different meshes alongside with the reference computation are shown in Figure 1-25, Figure 1-26 and Figure 1-27 for  $N_{bv} = 0.1$ ,  $N_{bv} = 0.5$  and  $N_{bv} = 1$  respectively. For the weaker stratification, there is a mostly linear vortex descend through time. For the first time, the CEDRE computation shows a good agreement with the reference computation. The curves then separate at higher time. However, the overall evolution is in qualitative agreement. One can also see that the first Mesh (Mesh3) has already converged. For a medium stratification, the vortices follow a linear descent for the first characteristic time. Then the descent velocity decreases slightly for 2-2.5 characteristic time before it grows significantly for the rest of the computation. The comparison with the reference computation shows a rather good agreement for the first characteristic times before the difference between the two computations increases. In that case, Mesh3 is close to convergence; however, it is more accurate to use the Mesh4 which has converged. Results for  $N_{bv} = 0.8$  are not shown as they lead to the same results in term of both vortices behavior and mesh convergence.

For higher stratifications, the descend velocity is firstly linear before it decreases. The vortices begin to go upward at about 2.5 characteristic time. These velocities once again change sign at 3.5 characteristic time. Then the vortices lose altitude quicker than at the beginning of the computation. However, mesh convergence has not yet been reached for this case.

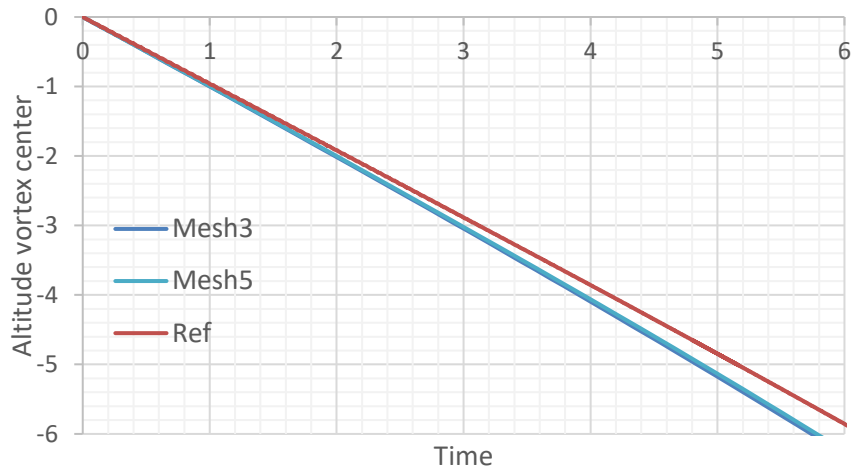


Figure 1-25 : Vortex vertical position through time for several meshes and  $N_{bv} = 0.1$ . The red curve is the data for the reference computation.

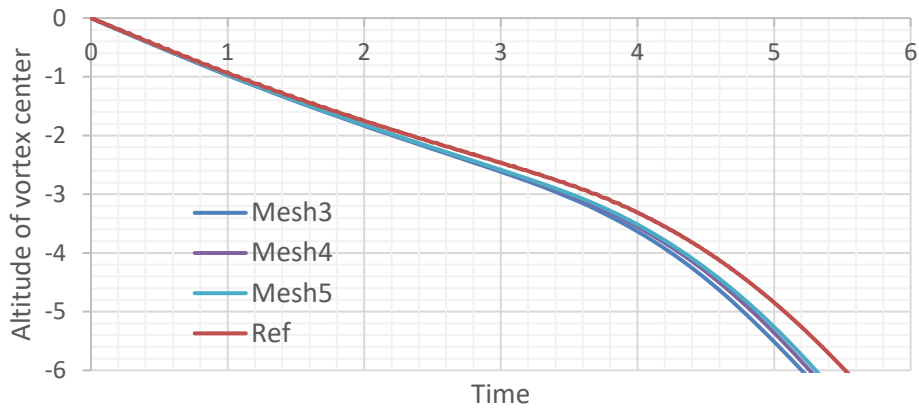


Figure 1-26 : Vortex vertical position through time for several meshes and  $N_{bv} = 0.5$ . The red curve is the data for the reference computation.

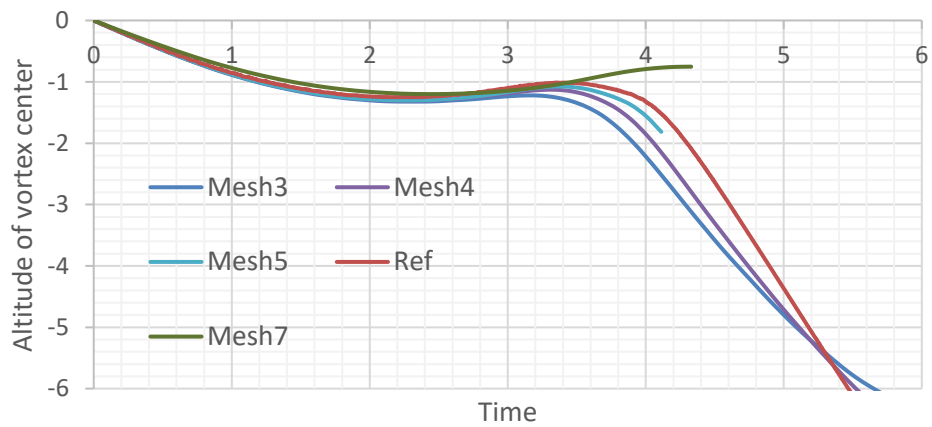


Figure 1-27 : Vortex vertical position through time for several meshes and  $N_{bv} = 1$ . The red curve is the data for the reference computation.

These computations validate the vortex computation for weak and average stratification (up to  $N_{bv} = 0.8$ ). However, the case  $N_{bv} = 1$  requires further investigation.

### 1.4.2.5. First results with ice crystals

A first case with ice crystal has recently been performed. For this computation, the vortex parameters have been set to values corresponding to an A320. The values are given by Unterstrasser et al. (2014).  $\Gamma_0 = 240 \text{ ms}^{-1}$ ,  $b_0 = 27 \text{ m}$  and  $a_0 = 3 \text{ m}$ . The reference pressure has been set to  $P_{ref} = 25000 \text{ Pa}$  and  $T_{ref} = 217 \text{ K}$ . Moreover, the relative humidity with respect to ice has been set to  $RH_i = 140 \%$  at flight altitude.

Ice crystals have been initialized as follow.  $3.4 \times 10^{12}$  ice crystals have been spread over  $10^5$  numerical particles. Each numerical particle contains  $3.4 \times 10^7$  particles of the same radius. For each numerical particle, a lognormal random variable has been drawn to find the mass of the particles. The mean value of the law corresponds to a particle of  $2.2 \text{ }\mu\text{m}$  diameter. Its variance is  $\sigma = 3.246$ . Then a normal random variable has been drawn to find the distance of the particle with the vortex center and a uniform law has been drawn to find its azimuthal position. The initial velocity and temperature of the crystals were chosen as the gas temperature and velocity at the drawn position. Half of the numerical particles have been set around each vortex. The mean radius of the spatial distribution was set to  $2a_0$  with a variance of  $\sigma = 2$ .

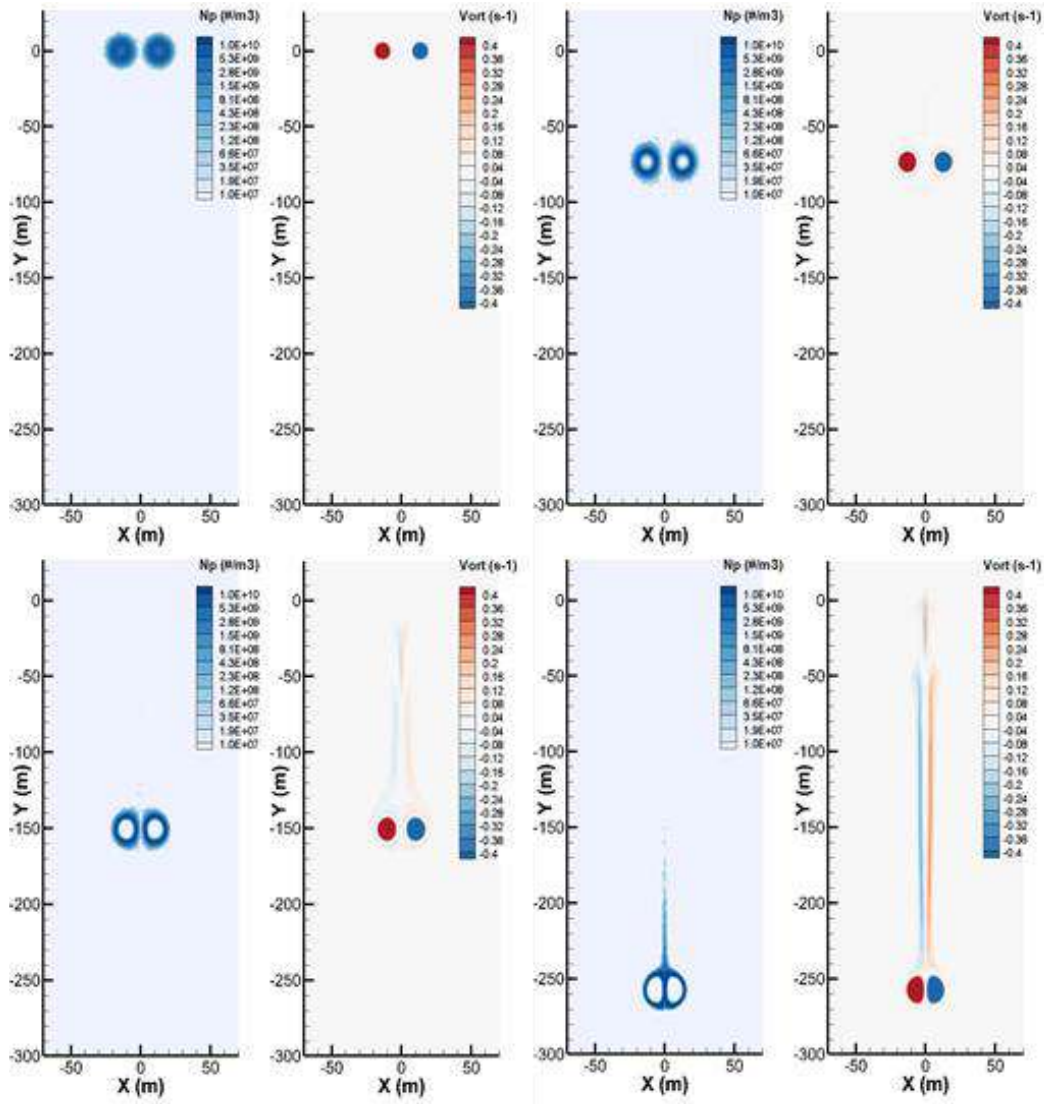


Figure 1-28: Ice crystals number concentration alongside the vorticity field for (left to right)  $t = 0 \text{ s}$ ,  $50 \text{ s}$ ,  $100 \text{ s}$  and  $150 \text{ s}$

The ice crystals number concentration and the vorticity field of this computation are shown in Figure 1-28 for  $t = 0, 50, 100$  and  $150$  s. One can see that the center of the vortices have some ice crystals at  $t = 0$  s, but they disappeared early in the computation since the vortex centers are almost free of ice crystals at  $t = 50$  s. The secondary vortex begins to form between  $t = 50$  s and  $100$  s however few ice crystals are following this motion at first. However, when the vortices get closer from each other, between  $t = 100$  and  $150$  s, the ice crystals begin to follow the vorticity leak. The interpretation of this last phenomenon is that at first almost all ice crystals are inside the Kelvin oval formed around the vortex pair. When the vortices get closer from each other, the Kelvin oval width reduces meaning that, at some point some ice crystals are outside of this oval and can now follow the vorticity leak. This scenario has to be confirmed with further simulations.

### 1.4.3. *Interface between the near field (jet regime) and the intermediate field*

The Jet phase will be computed using a RANS approach as described by Khou (2016) whereas the vortex phase is computed using a 3D temporal LES as described previously. The aim is to initialize the LES computation with data given by the RANS computation such as the velocity field, the temperature of the jet, the turbulence, and the ice crystals properties.

The method consists in extracting a 2D plan from the 3D RANS computation and initializing the 3D temporal LES with it. In practice, the 2D slice field is extruded on the LES mesh. Only the temperature, pressure, velocity, and ice crystals properties are used at this step. One can also use the turbulence variable in order to initialize the disturbance of the mean flow.

The disturbance will be determined using a random flow generation technique such as the one presented by Smirnov et al. (2001) or Auerswald and Bange (2014). This technique allows to scale the random field using the RANS turbulence variables. Smirnov et al. (2014) assumes a Gaussian spectrum whereas Auerswald and Bange (2014) allows to choose the spectrum. Both methods are ready for non-homogeneous, non-isotropic turbulence which will be the case for large structures of the atmospheric turbulence and if a RSM model is used for RANS computation. No pressure or temperature fluctuations are introduced at this stage; however, some evolutions of Smirnov et al. (2001) proposed these fluctuations.

This year the Smirnov et al. (2001) method has been chosen because it presents the basic steps for other techniques like the one proposed by Auerswald and Bange (2014) but is simpler. It has been tested on a simplified case where spatial LES, experimental results and a RANS computation are available. The available numerical results can be found in Chmielarski (2021) and the experimental results in Jacquin et al. (2007). It consists in a Naca 12 airfoil with jets. A schematic view is shown in Figure 1-29.

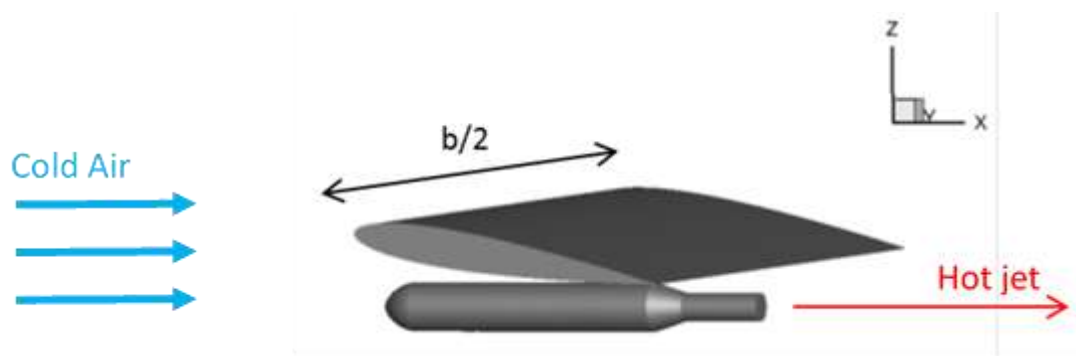


Figure 1-29: schematic view of the RANS numerical set up.

A 2D slice of the RANS field from Chmielarski (2021) has been extracted at 0.5 span and extruded on a 3D LES mesh. Then the perturbation of Smirnov et al. (2001) has been introduced. The computation has been done up to reaching the end of the RANS, spatial LES, and experimental domain (8 span). The relative temperature ( $T_r = \frac{T-T_i}{T_i}$  where  $T_i = 300$  K) for this computation alongside with experimental results from Jacquin et al. (2007) and RANS and ZDES results from Chmielarski (2021) are shown in Figure 1-30. For the LES results a mean flow has been derived by a streamwise integration of the temporal result. One can see a good qualitative agreement between the LES computation and both the ZDES and Experimental results. However, the cooling seems slightly late in the LES computation. This might be due to the Gaussian spectrum used to initialize the turbulence, which could lead to a wrong mixing of the jet, or to the streamwise uniformity hypothesis necessary to its approach, which neglects the streamwise conduction. However, the rolling up of the jet around the vortex is better captured by the temporal LES than by the RANS computation.

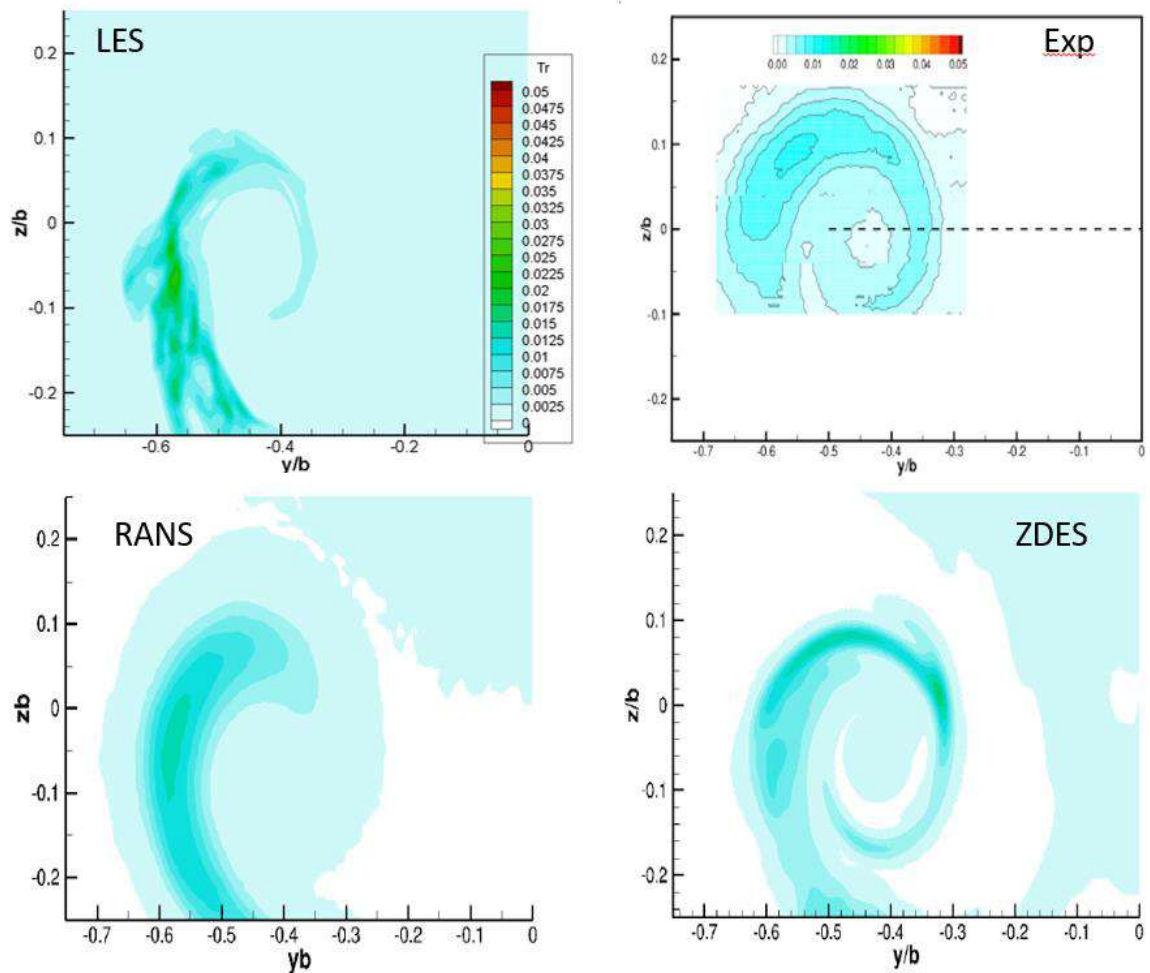


Figure 1-30 : Relative temperature at  $\frac{x}{b} = 8$  for temporal LES (upper left), experimental data from Jacquin et. Al (2007) (upper right), RANS (lower left) and ZDES (lower right) results from Chmielarski (2021).

## 1.5. WP 1.5: Evolution of contrails on climatic scales

Contributors: Audran Borella (Masters intern, IPSL), Olivier Boucher (IPSL)

The objective of work package 1.5 is to simulate the evolution of contrails at the synoptic scale. The atmospheric general circulation model LMDZ, which is a component of the IPSL climate model, will be used to do so.

### 1.5.1. Parametrization of ISSR in LMDZ

We build on the existing cloud parametrization of the LMDZ model (Madeleine et al. (2020)) to include the possibility of forming an Ice-Supersaturated Region (ISSR) in a fraction of the gridbox (Figure 1-31). For this, we use a generalized log-normal to predict the distribution of the total water in the gridbox and divide the gridbox in three areas (Figure 1-32). We keep memory of i) the cloudy fraction and ii) the ratio between the ISSR and cloudy fractions from one timestep to the next. This is required because the transfers are asymmetrical: they are possible in both directions between the subsaturated and the supersaturated fractions of the gridbox, however they are only possible from ISSR to the cloudy fraction and from the cloudy fraction to the subsaturated clear-sky fraction. The three fractions and their water content can vary according to physical processes such as large-scale condensation (from one timestep to the other) or turbulent mixing (within a timestep). Clouds can only form through the ISSR, and clouds can only evaporate into the subsaturated clear-sky fraction. The maximal clear-sky supersaturation beyond which a cloud forms by homogeneous nucleation is a function of temperature:  $\gamma_{ss} = 2.583 - T / 207.83$  with T in K (Kärcher and Lohmann (2002)).

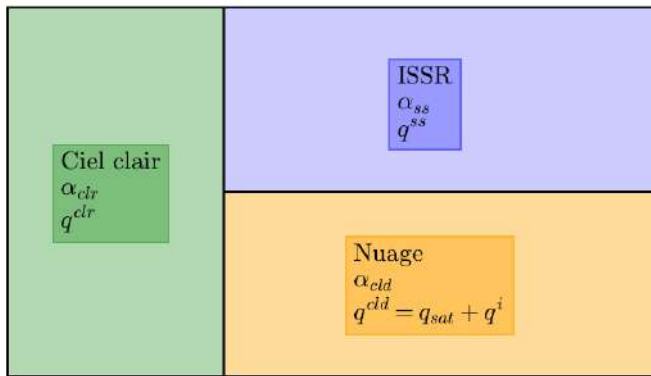


Figure 1-31. Model gridboxes are divided into three fractions: a subsaturated clear-sky fraction (in green), a supersaturated clear-sky fraction (ISSR, in blue), a cloudy fraction (in yellow). Humidity is assumed to be at saturation in the cloud.

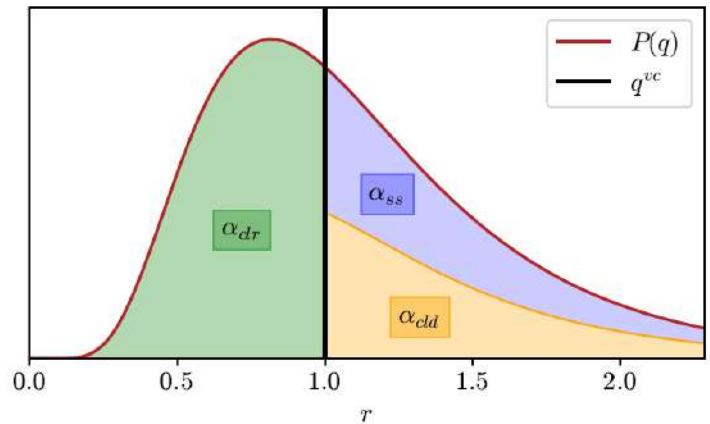


Figure 1-32. PDF of the subgrid scale total water in a grid-box. The relative ISSR and cloudy fractions evolve in time according to cloud processes.

The full details of the new ISSR parametrization can be found in the MSc report of Borella (2021). There are four different parameters that can be used to tune (calibrate) the model against some observations. These include: the ratio in the tail of the PDFs for ISSR and cloudy fractions, the width of the PDF, the turbulent mixing length around the cloud and an aspect ratio parameter for the cloud boundaries with the ISSR and the clear-sky fractions of the gridbox. Figure 1-33 shows the PDF of the relative humidity in the North Atlantic Flight Corridor in the IAGOS observations. With some preliminary parameter tuning, the model is able to

represent reasonably well the PDF of RH in the subsaturated and supersaturated regions. The model simulates a strong mode for  $RH_{ice} = 100\%$  because all cirrus clouds are assumed to be at thermodynamic equilibrium (i.e., ice crystals are in equilibrium with their environment) whereas this is known not to be the case. Furthermore, measurement uncertainties from IAGOS probably contribute to flatten the distribution mode. This said it is likely that the model simulates too flat a PDF as a function of  $RH_{ice}$  between 100 and 140%, which needs to be understood and corrected.

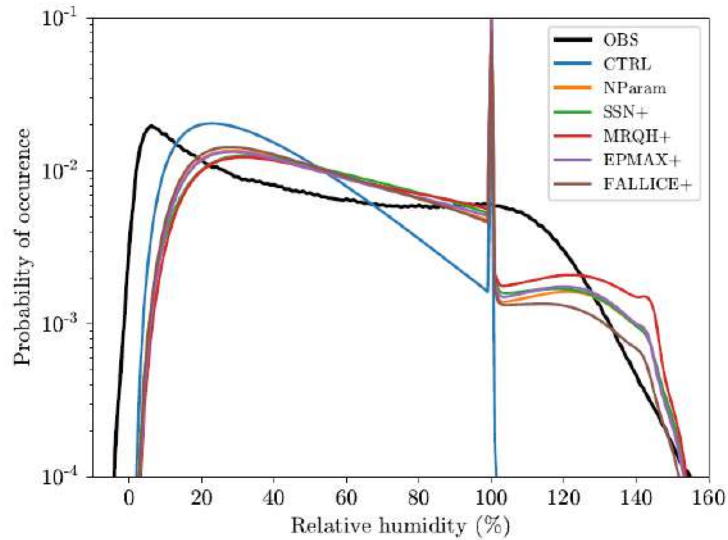


Figure 1-33. PDF of the relative humidity in the North Atlantic Flight Corridor in the IAGOS observations (solid black curve) and in sensitivity experiments with the new ISSR parametrization using different set of parameters.

### 1.5.2. Calibration of ISSR in LMDZ

The next stage of the work will consist in calibrating the new ISSR parametrization in the context of the other cloud parametrizations. Indeed, parametrizations do interact between them, and it is meaningful to proceed to such model tuning (Hourdin et al. (2017)). The new ISSR parametrization has deteriorated some aspects of the model climatology while it has improved others. A preliminary set of sensitivity experiments has been performed to infer the sensitivity of key model outputs to the input parameters. As an initial step to this tuning, which will be done in 2022/2023, we show in Figure 1-34 how the gridbox fractions of supersaturated clear sky and cloudy sky vary with key parameters. Table 5 lists the tuning parameters that have been tested in sensitivity experiments.

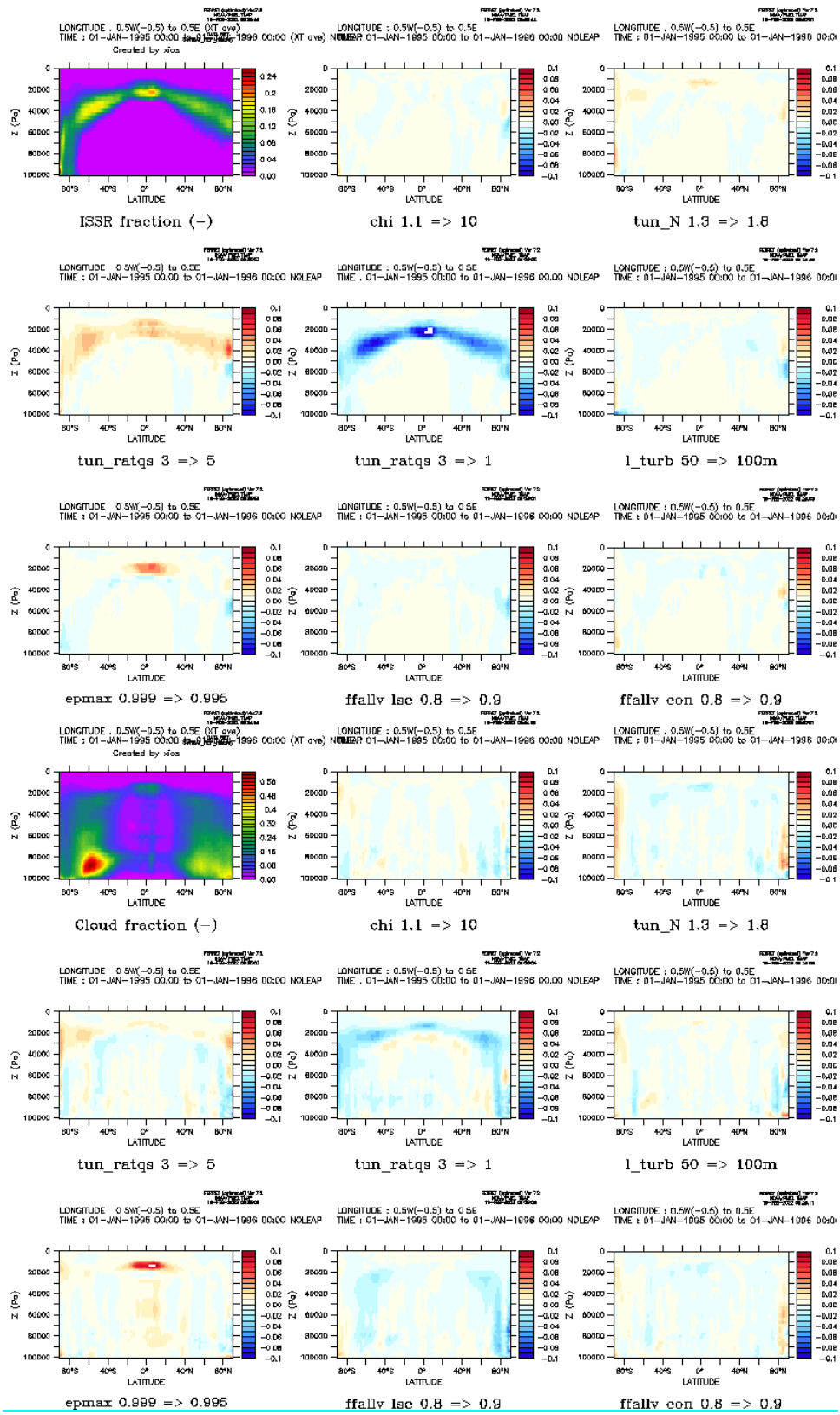


Figure 1-34: Supersaturated clear-sky fraction (top 9 panels) and cloudy sky fraction (bottom 9 panels) in the LMDZ model for the baseline configuration (top left panel) and 8 sensitivity studies to some tuning parameters as per Table 5.

Table 5: List of tuning parameters that have been tested in sensitivity experiments.

Parameter	Meaning	Reference value	Tested value
flag_chi	aspect ratio parameter for the cloud boundaries with the ISSR and the clear-sky fractions of the gridbox	1.1	10
tun_N	ratio in the tail of the PDFs for ISSR and cloudy fractions	1.3	1.8
flag_tun_ratqs	width of the total water PDF	3.0	5.0
flag_tun_ratqs	width of the total water PDF	3.0	1.0
flag_l_turb	turbulent mixing length around the cloud	50 m	100 m
epmax	Fraction of total water being lost in convective tower (1-epsmax is detrained at top)	0.999	0.995
ffallv_lsc	Scaling parameter for the ice crystal fall velocity for stratiform clouds	0.8	0.9
ffallv_con	Scaling parameter for the ice crystal fall velocity for convective clouds	0.8	0.95
ratqsp0	Pressure level for the bottom of the layer where ratqs varies	45000	35000
ratqshaut	Width of the total water PDF at the top of the later where ratqs varies	0.4	0.5
oicemax	Maximum ice crystal mixing ratio in cirrus clouds	0.0015 kg/kg	0.0010 kg/kg
rei_min	Minimum ice crystal size in cirrus clouds	16 $\mu\text{m}$	10 $\mu\text{m}$
rei_max	Maximum ice crystal size in cirrus clouds	61.29 $\mu\text{m}$	70 $\mu\text{m}$

## 1.6. WP 1.6: Detailed study of the radiative impact of contrails

Contributors: Christophe Bellisario (ONERA), Claire Malherbe (ONERA), Lionel Tessé (ONERA), Olivier Boucher (IPSL), Julie Carles (PhD student, IPSL), Jean-Louis Dufresne (IPSL), Nicolas Bellouin (IPSL)

The objective of Work Package 1.6 is to compare several numerical methods for solving the radiative transfer equation on accurate radiative transfer calculations at the scale of a contrail and/or cirrus cloud. The limitations of each of these methods will be evaluated, especially in terms of their ability to consider spatial heterogeneities. Then, we will check if the assumptions made in the global models of the IPSL are appropriate, in order to improve or correct, if necessary, the parameterization on which these global models are based.

During this first year, many meetings have been organized between IPSL and ONERA to know each other and start working together. The work programme has been jointly defined and written and the activities of the first step of the work programme have started. The radiative transfer codes available at IPSL and ONERA have been identified, characterized, and their abilities compared (Sections 1.6.1 and 1.6.2). Moreover, a benchmark test case has been defined (Section 1.6.3) to compare quantitatively all the identified codes. The work of IPSL PhD student Julie Carles on the impact of cloud heterogeneities on radiative forcing is summarized in subsection 1.6.4.

### 1.6.1. Codes description

Six radiative transfer codes have been identified:

- two at IPSL: ecRad and htrdr ;
- four at ONERA: MODTRAN, MATISSE, CERAMIC and ASTRE.

The six codes are described below. MODTRAN is not developed at ONERA, but it is available and often used in the Optics Department (ONERA/DOA).

#### 1.6.1.1. *htrdr* - The Monte-Carlo radiative transfer simulator

*htrdr* evaluates the intensity of radiation at any position (probe) of the scene, in any direction, in the presence of surfaces and an absorbing and scattering semi-transparent medium, both for radiation sources that are internal to the medium (longwave) or external to the medium (shortwave). Intensity is calculated using the Monte-Carlo method: several optical paths are simulated backward, from the probe position and into the medium. Various algorithms are used, depending on the specificities of the nature and shape of the radiation source. For atmospheric radiative transfer, the clear-sky atmosphere is vertically stratified, cloud thermodynamic data is provided on a regular 3D rectangular grid, and surface optical properties can be provided for an arbitrary number of materials. Internal and solar radiation are taken into account.

The algorithms that calculate the radiance are used for computing various quantities:

- *Images* on a camera sensor, in a given field of view. In atmospheres, both visible and infrared images are possible: CIE (International Commission on Illumination) colorimetry is used for visible images, while an infrared image is in fact a temperature map of luminosity, over the required spectral interval.
- *Flux density maps*, on a grid of sensors, integrated over an entire hemisphere. Spectrally integrated flux density maps (both on the visible part of the spectrum and on the infrared) are possible for atmospheric applications.

Villefranque et al. (2019) and Sans et al. (2021) describe two examples of application of htrdr. More information about htrdr can be found at <https://www.meso-star.com/projects/htrdr/htrdr.html>

#### 1.6.1.2. *ecRad - ECMWF atmospheric radiation scheme*

ecRad is a radiation scheme suitable for use in atmospheric weather and climate models. The code is designed to be extensible and flexible (Hogan and Bozzo (2018)). The gas optics, cloud optics and solver are completely separated. Five solvers are currently available:

1. The Monte Carlo Independent Column Approximation (McICA). This is a now widely used method for treating cloud structure efficiently.
2. The Tripleclouds scheme. This represents cloud structure by dividing each layer into three regions, one clear and two cloudy with different optical depth.
3. The Speedy Algorithm for Radiative Transfer through Cloud Sides (SPARTACUS). This is a method for efficiently treating 3D radiative effects associated with clouds. It is extended to the longwave and incorporates the Tripleclouds methodology to represent cloud inhomogeneity.
4. A homogeneous (plane parallel) solver in which clouds are assumed to fill the gridbox horizontally. This is useful for computing Independent Column Approximation benchmarks.
5. A “cloudless” solver for clear skies.

One gas optics model is provided: The Rapid Radiative Transfer Model for GCMs (RRTMG). More information about ecRad can be found at <https://confluence.ecmwf.int/display/ECRAD/ECMWF+Radiation+Scheme+Home>

#### 1.6.1.3. *MODTRAN*

The MODTRAN (MODERate resolution atmospheric TRANsmission, Berk et al. (2014)) computer code has been developed in the USA for about 30 years, by both Spectral Sciences Inc. (SSI) and the Air Force Research Laboratory (AFRL). It is used worldwide, and is a reference code for the main atmospheric codes developed at ONERA/DOTA. Moreover, MODTRAN is used at ONERA/DOTA for the prediction and analysis of optical measurements through the atmosphere.

The MODTRAN software computes line-of-sight (LOS) atmospheric spectral transmittances and radiances over the ultraviolet through long wavelength infrared spectral regime ( $0 - 50\,000\text{ cm}^{-1}$ ). The radiation transport (RT) physics within MODTRAN provides accurate and fast methods for modelling stratified, horizontally homogeneous atmospheres. The core of the MODTRAN RT is an atmospheric "narrow band model" algorithm. The atmosphere is modelled via constituent vertical profiles, both molecular and particulate (aerosols and clouds), defined either using built-in models or by user-specified radiosonde or climatology data. The band model provides resolution as fine as  $0.2\text{ cm}^{-1}$  from its  $0.1\text{ cm}^{-1}$  band model. MODTRAN solves the radiative transfer equation including the effects of molecular and particulate absorption/emission and scattering, surface reflections and emission, solar/lunar illumination, and spherical refraction.

MODTRAN sources are not distributed and the need to develop own tools for atmospheric modelling is obvious as it is shown in subsection 1.6.2. MODTRAN presents a lack of features for some applications. As an example, 3D simulations are not available with MODTRAN. More information about MODTRAN can be found at <http://modtran.spectral.com/>

#### 1.6.1.4. *MATISSE*

*MATISSE* (Advanced Modelling of the Earth for the Imagery and the Simulation of the Scenes and their Environment) has been developed at ONERA for about fifteen years (Labarre et al. (2011)). Many research laboratories (IREENA, IRIT, LMD, LOA, Météo-France/CNRM, RDDC...) have been involved for collaborate to the development of the code. The code is supported by DGA (French Defense Agency). *MATISSE* has been selected as a reference code for DGA applications.

The radiative transfer code *MATISSE* can help to design/realize optronic sensor and develop detection algorithm in spectral bandwidth ranging from 0.25 (LOS) / 0.4 (IMG) to 14  $\mu\text{m}$ . It provides:

- spectral images of natural backgrounds as clear atmosphere, water and ice altitude clouds, geo-located land and sea, as seen by spaceborne, airborne or shipborne sensors.
- path transmission and radiances along a line of sight, with special care of mirage effect at very low altitude above sea surface.
- contribution to the evaluation of target / background contrast (line by line).
- sky radiance or local illumination around a target point for signature computation.
- turbulence characterization for VIS, IR imaging.

*MATISSE* manages a whole collection of global geo-located and complementary databases: atmospheric profiles, aerosols, digital terrain elevation and biome, optical parameters of clouds, ground spectral reflectivity, etc. A graphical user interface (GUI) helps to define the computational cases. Nowadays, 3D clouds are not yet available, but a new version including 3D Cirrus is being developed. Validation is included in *MATISSE* development by periodic comparisons with measurements (example: MIRAMER field campaign for the sea surface model). More information about MODTRAN can be found at <https://matisse.onera.fr/>

#### 1.6.1.5. *CERAMIC*

The *CERAMIC* package (Cloudy Environment for RAdiance and Microphysics Computation, Bellisario et al. (2016)) combines cloud microphysical computation and 3D radiance computation to produce a 3D visible or infrared radiance scene in attendance of clouds.

The input of *CERAMIC* starts with an observer with a spatial position and a defined field of view (by the mean of zenithal and azimuthal angles). A 3D cloud generator is introduced; it is provided by the LaMP (Laboratory of Physical Meteorology) for statistical and simplified physics. The cloud generator is implemented with atmospheric profiles including heterogeneity factor for 3D fluctuations. *CERAMIC* also includes a cloud database from the CNRM for a physical approach. Molecular optical properties are provided by *MATISSE*. Aerosols are not yet implemented in *CERAMIC*.

The 3D radiance is computed with the model LUCI (for “LUminance de CIrrus” in French, Cirrus Radiance). It takes into account 3D microphysics with a resolution of  $5 \text{ cm}^{-1}$ , from 0.4  $\mu\text{m}$  to 12  $\mu\text{m}$ . LUCI has now been extended to another types of clouds in low and middle levels.

To have a fast computation time, most of the radiance contributors are computed with analytical expressions. The multiple scattering phenomena are more difficult to model. A discrete ordinate method (DOM) with correlated-K precision to compute the average radiance is used. A 3D fluctuations model is added (based on a behavior model).

Spatial images are produced, with an actual dimension of 10 km x 10 km and a vertical resolution of 0.1 km, with each contribution of the radiance separated.

### 1.6.1.6. *ASTRE*

ASTRE is a radiative transfer code based on a Monte Carlo method (Tessé and Lamet (2011)). ASTRE was first designed to compute radiative transfer in atmospheric turbulent sooty flames by taking into account turbulence-radiation interactions. Various radiative property models have been then implemented in ASTRE to deal with high pressure combustion chambers, atmospheric re-entries, glass forming, high altitude plumes... but ASTRE has never been applied to the atmosphere.

Three kinds of gas radiative property models are available: Correlated-K, Statistical Narrow Band and Box models. Parameters of the gaseous species H<sub>2</sub>O, CO<sub>2</sub>, CO and HCl are available. These species are the main radiating species present in combustion chambers or plumes behind motors.

Three types of particles can be treated: soot, alumina (liquid/solid) particles and water droplets. During the first year of Climaviation, the ice optical index model of Warren and Brandt (2008) has been implemented to deal with ice clouds.

A hybrid MPI-OpenMP parallelization is implemented in ASTRE to track a large number of independent energy bundles involved in a Monte Carlo simulation.

### 1.6.2. *Comparison of code characteristics*

Table 6 to Table 10 summarize several aspects of the comparisons between radiative transfer models. Within each table, “Need further work” means that models do not have the listed ability, but it could be implemented within the timeframe of the project. In Table 6, “local but can be extended” means that although computations are performed on a column with a given vertical atmospheric profile, one can vary the atmospheric profiles to calculate fluxes worldwide.

*Table 6: Features of the different codes regarding solving the radiative transfer equation.*

	htrdr	ecRad	MODTRAN	MATISSE	CERAMIC	ASTRE
Flux ready for use	Yes	Yes	Yes	Need further work	Need further work	Yes
Solver	Monte Carlo	2-flux	2-flux & DOM	2-flux & DOM	DOM	Monte Carlo
Number of streams	N/A	2	2 & multi	2 & multi	2 & multi	N/A
Vertical atmospheric profile	Yes	Yes	Yes	Yes	Yes	Need further work
Worldwide spatial distribution	Need further work	Local but can be extended	Need further work			

Table 7: Features of the different codes regarding physical processes.

	htrdr	ecRad	MODTRAN	MATISSE	CERAMIC	ASTRE
Molecular scattering	Yes	Yes	Yes	Yes	Yes	Need further work
Gaseous absorption	Yes	Yes	Yes	Yes	Yes	Yes
Polarization	No	No	No	No	No	No
Thermal ground module	No	No	No	Yes	No	No
Surface type	Several possibilities	Albedo	Albedo	Several possibilities	Albedo	Grey and spectral isotropic emissivity, diffuse and specular reflections

Table 8: Features of the different codes regarding atmosphere composition.

	htrdr	ecRad	MODTRAN	MATISSE	CERAMIC	ASTRE
Gaseous molecules	Yes	Yes	Yes	Yes	Yes	H <sub>2</sub> O, CO <sub>2</sub> , CO and HCl only
Clouds (all types)	Water clouds only	Yes	Yes	Yes	Yes	Water clouds only
Aerosols	Need further work	Yes	Yes	Yes	Need further work	Soot only

Table 9: Features of the different codes regarding ice clouds.

	htrdr	ecRad	MODTRAN	MATISSE	CERAMIC	ASTRE
3D	Yes	SPARTACUS	No	No	Yes	Yes
Changeable microphysics	Need further work	Need further work	?	Yes	Yes	Yes
Variable altitude	Yes	+McICA	Yes	Yes	Yes	Yes
Kext variable	Yes	Yes	Yes	Yes	Yes	Yes
Crystal phase function (method)	Henyeey Greenstein	Asymmetry	Mie (possible update)	Mie (possible update)	Mie (possible update)	Mie (possible update)
Alternate phase function	Offline	Offline	?	Offline	Need further work	Offline

Table 10: Features of the different codes regarding spectral characteristics.

	htrdr	ecRad	MODTRAN	MATISSE	CERAMIC	ASTRE
0.2 to 100 $\mu\text{m}$	Yes	Yes	Yes	Need further work (< 40 $\mu\text{m}$ )	Need further work	Yes
Solar spectrum	CK	CK	LBL/CK	LBL/CK	LBL	CK/SNB/Box model
Infrared band	CK	CK	LBL/CK	LBL/CK	LBL	CK/SNB/Box model
Resolution	Specific spectral intervals	Specific spectral lines	$> 1 \text{ cm}^{-1}$	$> 1 \text{ cm}^{-1}$	Resolution from refractive indexes	$> 25 \text{ cm}^{-1}$

### 1.6.3. Benchmark test case definition

As a first step for the radiative transfer code benchmark, a test case defined by a previous intercomparison of contrail radiative transfer (Myhre et al. (2009)) has been chosen to compare the codes described in subsection 1.6.1 to previous results available in the literature. It is a simple case. The selected atmospheric profile is the mid-latitude summer AFGL profile (Anderson et al., 1986), which provides vertical profiles of pressure, temperature, and concentrations of key optically active atmospheric constituents like ozone, water vapor, and carbon dioxide. (See for examples of mid-latitude summer profiles the green temperature profile in Figure 1-35 and the green ozone profile in Figure 1-36). Surface albedo is equal to 0.2 for all wavelengths. Three solar zenith angles have been selected ( $30^\circ$ ,  $60^\circ$  and  $75^\circ$ ). An optically thin ice cloud (cloud optical depth varying between 0.1, 0.3 and 0.52) is located between 10 and 11 km. Cloud cover is 1. The ice crystal asymmetry parameter is set to 0.8 at all wavelengths and their single-scattering albedo is 1 at solar wavelength and 0.6 in the terrestrial spectrum.

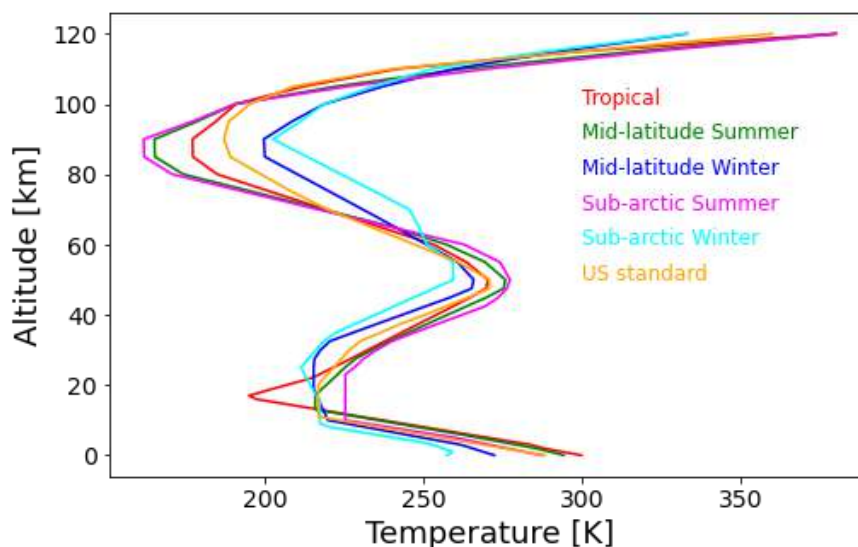


Figure 1-35 : temperature profiles from the six AFGL profiles.

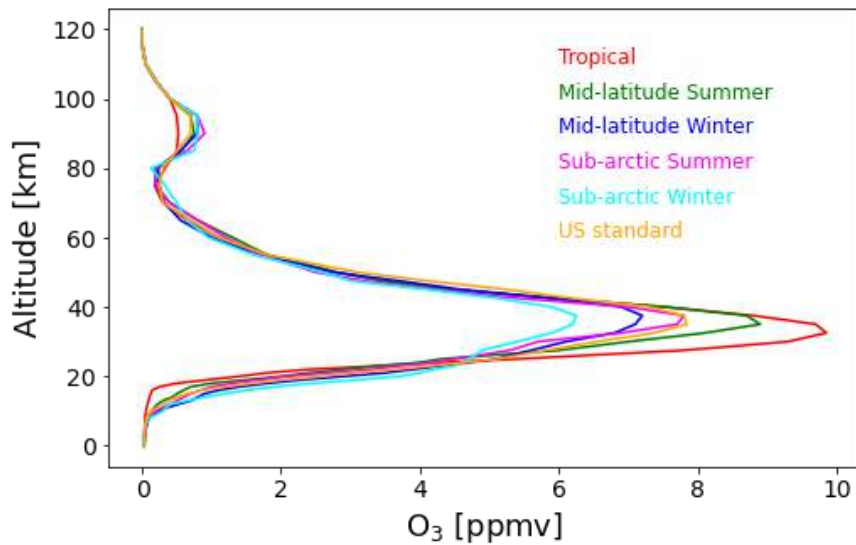


Figure 1-36:  $O_3$  profiles from the six AFGL profiles.

The first results of this simple benchmark test are available for htrdr and shown in Figure 1-37. Calculations have also been done for comparison with the libradtran (Emde et al. (2016)) radiative transfer code by Kevin Wolf, a Climaviation post-doctoral researcher at IPSL. Both codes give very similar results, within the range of Myhre et al. (2009). They compare particularly well with the line-by-line calculations with the University of Oslo code (UO\_LBL in Figure 1-37, which was the reference code in that paper. Computations with other codes will be done as soon as possible in function of the capabilities of each code and the developments that have to be done in each code. Based on the results, benchmark tests will then be made more complex and realistic.

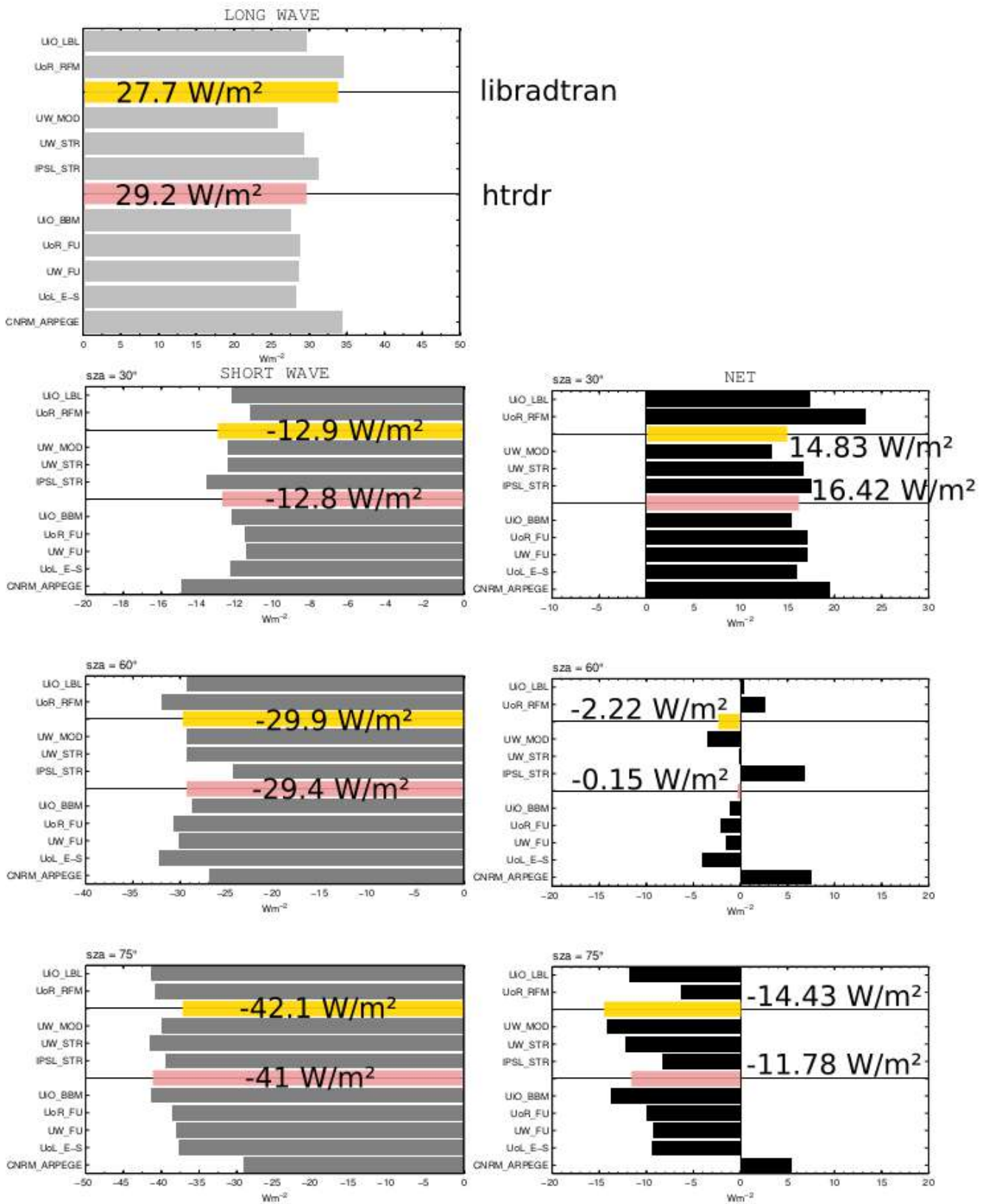


Figure 1-37: Figure adapted from Figure 2 of Myhre et al., showing the results of their intercomparison of radiative forcing of a contrail of optical depth 0.3 in the longwave (light grey, top panel), the shortwave (dark grey, for three values of solar zenith angle), and net longwave+shortwave (black, for three values of solar zenith angle). Results with libradtran and htrdr have been overlaid in yellow and pink, respectively.

#### 1.6.4. *Impact of 3D effects of the cloud field*

Julie Carles started a PhD at IPSL in October 2021, on the study of the radiative effects of contrails and cirrus clouds taking into account the 3D effects of the full cloud scene, including the effects of inhomogeneities, side effects and the interaction with surrounding clouds. To follow this goal, an accurate representation of contrails and surrounding cloud scenes in a radiative transfer (RT) code is needed. A first step of the study was the handling of htrdr, a radiative transfer code (Villefranque et al (2019), see also Section 1.6.1.1) using the Monte-Carlo method, which performs the rendering of 3D cloudy atmospheres and evaluates radiative transfer in the visible and in the infrared domains of the spectrum. Its abilities allow the study of the radiative forcing (RF) of clouds taking into account 3D effects and horizontal and vertical inhomogeneities.

Inputs that are needed by htrdr are an atmospheric profile (temperature, pressure profiles and optical properties of a gas mixture), a three-dimensional cloud (temperature, pressure, water vapor and liquid water content inside the cloud), the description of a surface and the optical properties of the cloud droplets.

An example of visible rendering of a cloud by htrdr is shown in Figure 1-38. The scene represents a cirrus cloud simulated by large eddy simulation (LES) for Axis 3 (see Section 3) and shows the kind of spatial heterogeneities that will be studied in the PhD project. Originally, htrdr was not built to evaluate the radiative effect of ice clouds. But Julie Carles has now added support for different parametrizations of ice crystals scattering properties (Baran et al. (2016) and Yang et al. (2000)), and the cloud shown in Figure 1-38 uses the parametrization by Baran et al. (2016).

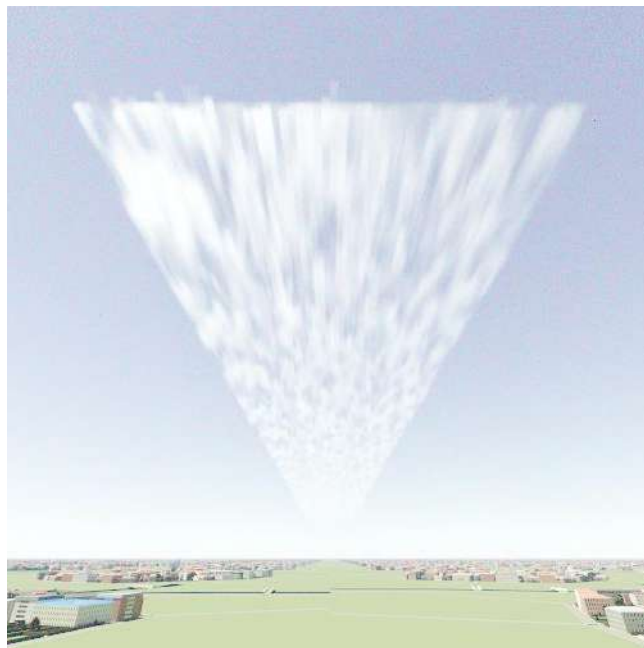


*Figure 1-38: Image rendered with htrdr, the Monte-Carlo radiative transfer simulator, representing a scene composed of a surface (a generic city), an atmospheric profile and a 3D cloud field from a large eddy simulation. The cloud was repeated several times in the x direction.*

Results obtained with the default water droplet optical properties calculated from a Mie code (Mishchenko et al. (2002)) have also been compared to cases using parametrizations of ice optical properties. The resulting radiative forcing is shown in Figure 1-39, for three different solar zenith angles ( $30^\circ$ ,  $60^\circ$  and  $75^\circ$ ) and four representations of optical properties of cloud particles. The net radiative forcing associated to a cloud

composed of liquid water spherical droplets (“Mie”) is higher than that of a cloud whose optics are represented by a parametrization of ice crystals (“Halifax”, “Baran 2017” and “Baran 2016”). The difference is higher for a small solar zenith angle, with a difference larger than 20 W/m<sup>2</sup> between the “liquid” and the “ice” clouds for a 30° solar zenith angle.

These differences do not yet account for horizontal and vertical variations of the optical properties of the cloud droplets/ice crystals. That raises the question of the radiative effects of heterogeneities inside the cirrus cloud. The associated technical goal is therefore to implement in htrdr a parametrization of ice crystals scattering properties that varies spatially, to evaluate the radiative effects associated to inhomogeneous ice clouds.

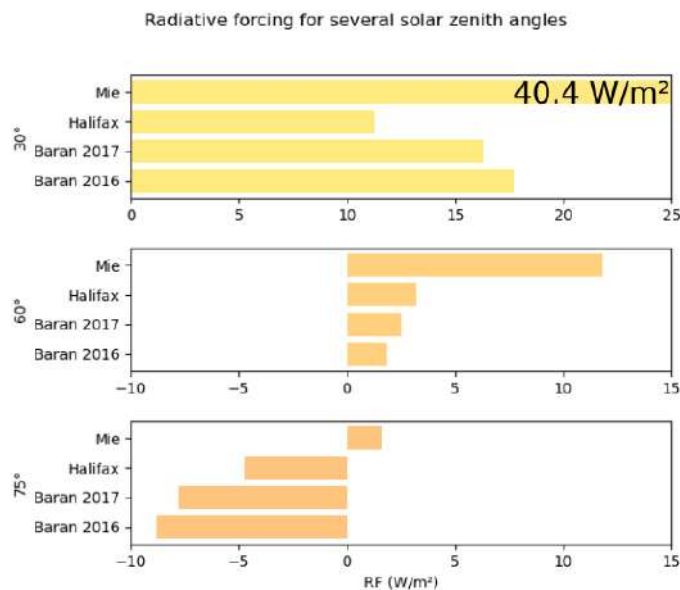


Figure 1-39 : Radiative forcing exerted by a cloud with an average ice water content of  $1.4 \cdot 10^{-5}$  kg/kg and an average temperature of 229 K. The top row corresponds to a scene with a solar zenith angle of 30°, 60° for the second row and 75° for the last row. On each row, the radiative forcing of the first line (“Mie”) is associated to a cloud whose droplets optical properties are obtained from a Mie code for an effective radius of  $10^{-6}$  meters. The second line radiative forcing is calculated for a parametrization of ice crystals scattering properties from Yang et al. (2000). The third- and fourth-line parametrizations are from Baran et al. (2016), calculated for the cloud averaged ice water content and temperature. The first line of the first row (“Mie” for a 30° solar zenith angle) has a radiative forcing of 40.4 W/m<sup>2</sup>, which has been cut to keep to a 25W/m<sup>2</sup> scale on all rows.

## 2. AXIS 2: ATMOSPHERIC CHEMISTRY

The objective of this axis of research is to study the chemical mechanisms that occur in the upper atmosphere and involve aircraft engine emissions. Particular attention is paid to the impact of NO<sub>x</sub>, ozone, and aerosols.

### 2.1. WP 2.1: Effective emission index

Contributor: Etienne Terrenoire (ONERA)

The objective of this work package is to calculate the chemical evolution of engine emissions (NO<sub>x</sub>, SO<sub>2</sub>, sulphate, nitrate) in the plume downstream of the aircraft to provide climate models with inputs relevant to climate scales. This will improve the accuracy of large-scale chemical mechanism assessments.

During the first year of the project, work has focussed on the literature review of existing aircraft plume parametrisation such as the one described in Cariolle et al. (2009). In this approach, a method is presented to parameterize the impact of the nonlinear chemical reactions occurring in the plume generated by concentrated NO<sub>x</sub> sources into large-scale models.

The review shows that two key parameters are necessary to establish the parametrisation: the mass time evolution and the reactivity of the emitted species (e.g., NO<sub>x</sub>) within the plume. The aim of the review was to understand how we could adapt this methodology using the ONERA 3D plume CEDRE model and the 0D INCA chemistry model. Different options are currently in discussion. One possibility is to use CEDRE in a first step to model with details the emission at the engine exit (Figure 2-1). Then, in a second step, the 0D INCA model would be used to calculate the evolution of the plume over several minutes. In this configuration, INCA0D would be initialised with the CEDRE outputs. As a first guess, the plume dilution will be taken from typical parametrisation found in the literature although the plume dilution as calculated by CEDRE could also be used especially in the first few seconds of the emission. In this case, the subgrid scale parametrisation parameters would then be deduced from the INCA 0D calculations.

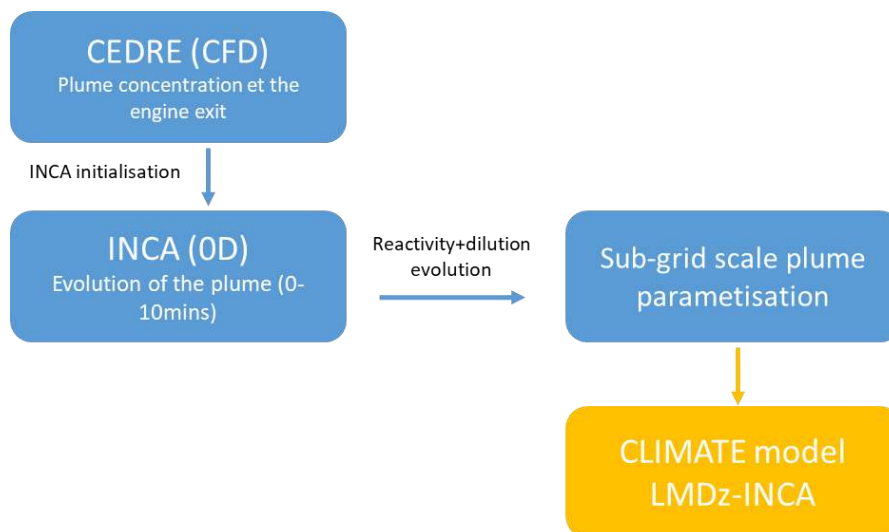


Figure 2-1 : Example of a workflow used to calculate the parameters of the subgrid-scale aircraft plume parameterisation

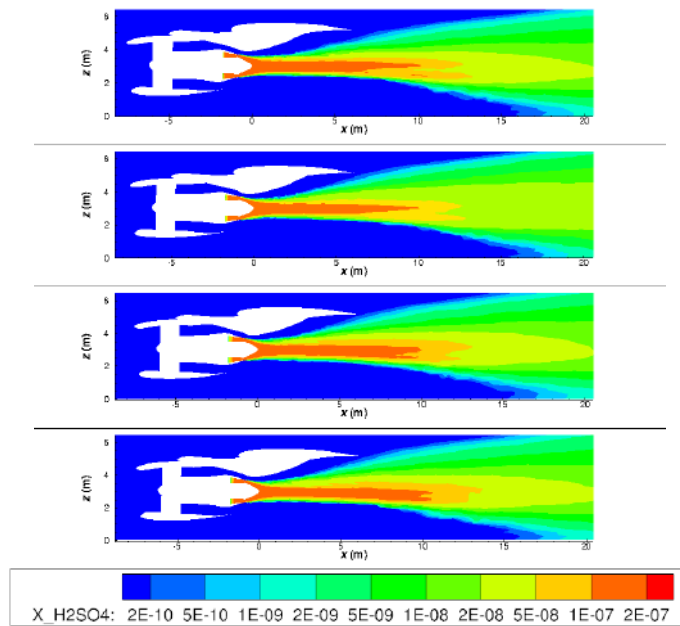


Figure 2-2 :  $H_2SO_4$  molar fraction side cross section for four thrusts as modelled by CEDRE for a typical long-haul type of engine. From top to bottom: 7%, 30%, 85% and 100%.

As an example, we show in Figure 2-2 the  $H_2SO_4$  concentration evolution for a typical long-haul type of engine plume as modelled by CEDRE. We modelled a rapid decrease of  $H_2SO_4$  concentration and the  $H_2SO_4$  molar fraction is divided by 50 only 20 m behind the engine exit. It is also noticed that despite a different mass flow for each thrust, the molar fraction fields are equivalent for all thrusts. Interestingly, one can notice that  $H_2SO_4$  is produced quasi instantaneously in the core nozzle before the actual release to the environment. Figure 2-3 presents the sulfur species and the relative temperature along a streamline from the core exit to the outlet of the domain for four different thrusts (7, 30, 85 and 100 %). For all thrusts, the  $H_2SO_4$  starts to be produced in the core nozzle when  $x < 1$  m (with  $x = 0$  corresponding to the combustion chamber exit). In this phase, the temperature remains constant.  $SO_3$  and  $SO_2$  are produced in the first instants ( $x < 3$  cm) but then  $SO_3$  is converted into  $H_2SO_4$ . Afterward, as distance increases from the engine exit ( $x > 10$ m), the molar fraction of those species decreases due to the dilution of the plume with the “clean” background ambient air. A decrease of temperature is observed when the core flow gets out from the nozzle ( $x = 1$ ). The temperature drop is minor for the lower thrust (−2% decrease) but much stronger for the highest thrusts (−23%).

The results are showed for the first few seconds of the plume lifetime. Next steps will include the development of a numerical approach (e.g., temporal approach) that will allow simulating the plume chemical evolution over several minutes after the engine emission (e.g., 10-15 mins).

The discussion will continue in the first part of the second year to select the best approach to develop a parametrization of the engine emissions, which could be implemented in a climate model like the LMDZ INCA climate model.

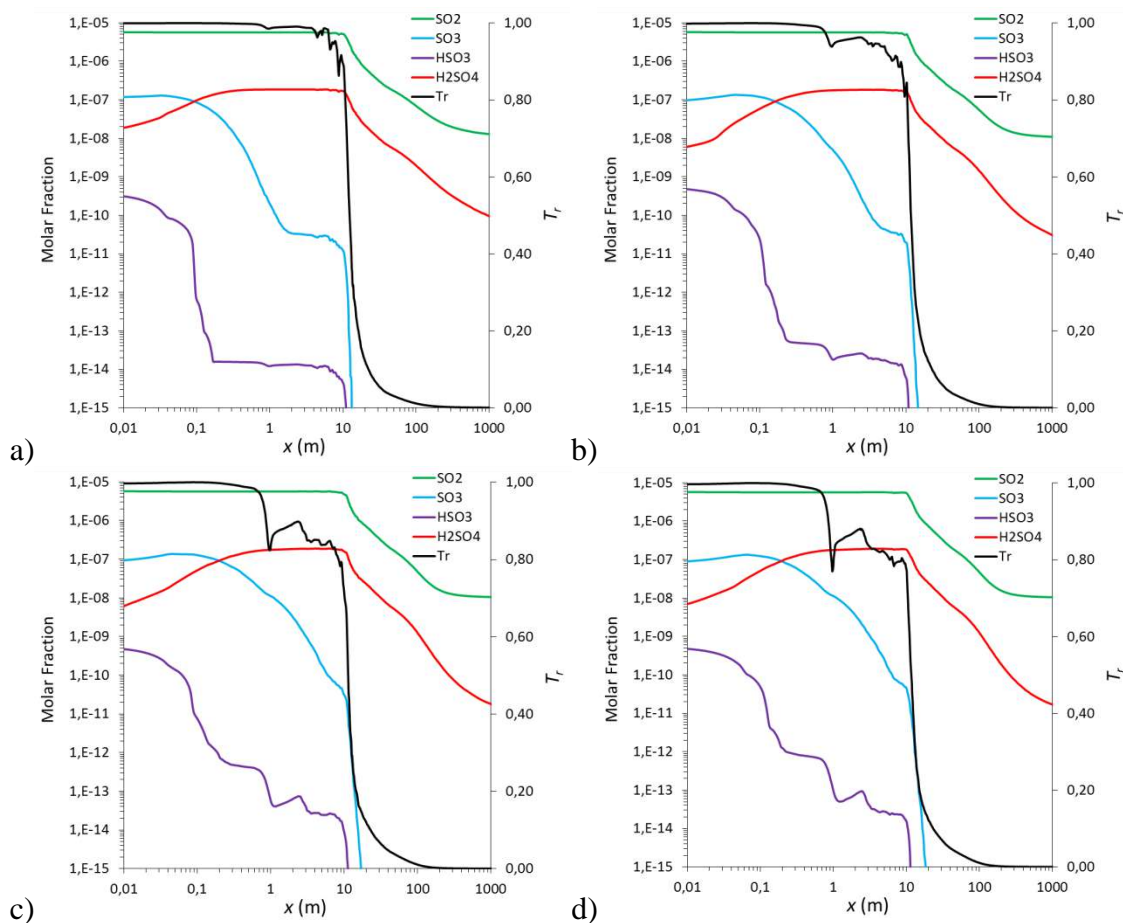


Figure 2-3. Molar fraction of sulfur species and normalized temperature  $T_r$  along a streamline from the core nozzle to the box outlet for four thrusts: a) 7%, b) 30%, c) 85% and d) 100%

## 2.2. WP 2.2: Improvement of the overall model

Contributor: Didier Hauglustaine and Yann Cohen (LSCE)

The objective of the work package is to implement a new version of the LMDZ-INCA global model, more complete and including the parameterization of the chemistry in the plumes in order to better quantify the  $\text{NO}_x$  forcing.

The development of a new version of the LMDZ-INCA model has started. This version of the model uses the new version of the IPSL CM6 model atmospheric component. It includes 79 levels (instead of 39 in the former CM5 model version), a new radiation scheme and new convection and boundary-layer parameterizations. The use of the new version of this model with chemistry has involved the refinement of the lightning parameterization and the scaling of the total annual flash rate to the observed OTD/LIS instruments values. In addition, the scavenging of soluble species (nitric acid and aerosols in particular) needed to be updated with the new convection scheme.

Test simulations with this version of the model have been performed and evaluated against ozone soundings data and IAGOS data in the upper troposphere and lower stratosphere. Simulations with this new version of the model will be reported in future reports.

### **2.3. WP 2.3: Impact of emissions on ozone and oxidizing capacity**

Contributor: Didier Hauglustaine (LSCE) and Etienne Terrenoire (ONERA)

The objective of this work package is to evaluate the atmospheric chemistry simulations by the LMDZ-INCA model with the IAGOS database, to identify improvements that can be made on the existing emissions and/or parameterizations, and to use the new version of the model to evaluate the impact of aviation emissions.

Before using the new version of the LMDZ-INCA model (WP2.2), simulations performed with a former version of the model and based on the previous REACT4C and QUANTIFY aircraft emission inventories have been analyzed and interpreted in order to serve as a benchmark before running the new model. The results have been summarized in a submitted manuscript (Terrenoire et al., submitted). This manuscript aims to quantify the impact of nitrogen oxides ( $\text{NO}_x$ ) and aerosols from the aviation sector on the chemical composition of the atmosphere as well as the associated direct radiative forcing (RF) of climate. We show that the net  $\text{NO}_x$  radiative forcing is largely affected by the revised  $\text{CH}_4$  radiative forcing formula which increases the total  $\text{CH}_4$  negative forcing by 15%. As a consequence, the ozone positive forcing and the methane negative forcing largely offset each other resulting in a slightly positive  $\text{NO}_x$  forcing for the present-day, smaller than the forcing due to  $\text{CO}_2$  emissions. In the future, the net forcing turns to negative due essentially to higher methane background concentrations.

We also stress the role of additional radiative forcing involving particle formation arising from an enhanced conversion of  $\text{SO}_2$  to sulfate particles by an increase in OH. Sulfate competes with nitrate for ammonium to form ammonium sulfate rather than ammonium nitrate. Therefore, the sulfate increase from  $\text{NO}_x$  emissions has the consequence of decreasing nitrates in the upper troposphere and reduce their negative forcing. In contrast, nitrate aerosols increase in the lower troposphere, exerting a negative forcing. When these aerosols radiative forcing are considered, the total  $\text{NO}_x$  forcing turns from a positive value to a negative value even for present-day conditions. Hence, total radiative forcing from aircraft emissions associated with changes in atmospheric chemistry and direct aerosols forcing is negative for both present-day and future (2050) conditions.

Several mitigation options involving flight aircraft operation and cruise altitude changes, traffic growth, engine technology, and fuel type, exist to reduce the climate impact of aircraft  $\text{NO}_x$  emissions. However, the climate forcing of aircraft  $\text{NO}_x$  emissions is likely to be small or even switch to negative (cooling) depending on atmospheric future background concentrations or when the  $\text{NO}_x$  impact on sulfate and nitrate particles is considered. Our results suggest that reducing aircraft  $\text{NO}_x$  emissions is primarily beneficial for improving air quality. For climate consideration, one option to reduce uncertainties in mitigation strategies might be to prioritize the reduction of  $\text{CO}_2$  aircraft emissions which have a well-established and long-term impact on climate.

### **2.4. WP 2.4: Impact of emissions on methane**

Contributor: Didier Hauglustaine (LSCE)

The objective of this work package is to simulate the response of methane to aviation emissions and in particular its residence time to aviation emissions and to estimate the indirect perturbations ( $\text{O}_3$ ,  $\text{H}_2\text{O}$ ). Simulations have been performed in order to calculate the methane indirect forcing associated with changes

in tropospheric ozone, stratospheric water vapor and CO<sub>2</sub>. The total methane forcing can be broken down into four distinct forcings. The methane decrease associated with enhanced oxidation by OH, is responsible for a long-term methane direct radiative forcing that we calculate at equilibrium based on the change in the methane photochemical lifetime, and including the methane feedback on its own lifetime. According to this methodology the steady-state methane mixing ratio decrease due to aircraft emissions is given by:

$$q_{CH_4} = q_{CH_4}^0 (1 + f \Delta\tau_{CH_4}) \quad (1)$$

where  $q_{CH_4}$  is the new steady-state methane mixing ratio,  $q_{CH_4}^0$  is the reference methane mixing ratio,  $f$  denotes the methane feedback on its own lifetime and  $\Delta\tau_{CH_4}$  (%) is the change in the methane lifetime due to aircraft emissions and subsequent OH perturbation. The feedback factor has been recalculated for the current version of our model based on a reference simulation and a 10% perturbation in methane surface mixing ratio simulation. Based on this set of simulations we recalculated a methane feedback factor  $f$  of 1.36, in agreement with the previous estimates. This factor is then used in Eq. (1) in order to derive the change in methane mixing ratio due to aircraft emissions and the associated radiative forcing of climate.

The indirect forcing associated with this change in methane mixing ratio through long-term tropospheric ozone and stratospheric water-vapor adjustments were recalculated with the LMDZ-INCA global model as well. This was done by imposing the new methane steady-state surface mixing ratio  $q_{CH_4}$  calculated from Eq. (1) in the 3D model and running for a period of 10 years in order to determine the associated change in ozone and stratospheric water vapor by comparing to a reference simulation using  $q_{CH_4}^0$  as methane surface mixing ratio. In this case, we calculated a change in ozone after 10 years of  $-0.93$  Tg (0.085 DU) and a change in stratospheric water vapor of  $-2.12$  Tg. We then calculated for these perturbations, an ozone radiative forcing of  $-2.82$  mW/m<sup>2</sup> and a stratospheric water vapor radiative forcing of  $-0.65$  mW/m<sup>2</sup>. This provides an indirect long-term ozone forcing of 116 mW/m<sup>2</sup>/ppmv of CH<sub>4</sub> and an indirect long-term stratospheric water vapor forcing of 27 mW/m<sup>2</sup>/ppmv of CH<sub>4</sub>. These numbers were then used to derive the indirect long-term ozone and water vapor forcing for the other aircraft emission scenarios based on a simple scaling with the methane mixing ratio change calculated with Eq. (1) for all simulations (Terrenoire et al., submitted).

Carbon dioxide is the end-product of the methane atmospheric oxidation. The production of CO<sub>2</sub> is hence an indirect radiative forcing resulting from the change in methane mixing ratio due to increased oxidation by OH resulting from aviation NO<sub>x</sub> emissions. Since intermediate carbon containing methane oxidation products are subject to dry and wet deposition, not every oxidized methane molecule results in a produced CO<sub>2</sub> molecule. In this study, we assume that 1 mole of change in CH<sub>4</sub> oxidation leads to 0.6 mole of CO<sub>2</sub> produced. The decrease in CH<sub>4</sub> due to enhanced oxidation is then translated into a change in CO<sub>2</sub> and converted to a radiative forcing based on the simple formula.

The sum of these four components provides the total methane radiative forcing associated with aircraft NO<sub>x</sub> emissions.

### 3. AXIS 3: IMPACT OF AEROSOLS ON NATURAL CLOUDS

The objective of the third axis of research is to investigate the mechanisms by which aerosol emissions from aircraft modify the formation and evolution of liquid and ice clouds, and to quantify the resulting radiative forcing.

#### 3.1. WP 3.1: Competition with background aerosols

Contributors: Jhaswantsing Purseed (postdoctoral researcher, IPSL), Nicolas Bellouin (IPSL)

The objective of this work package is to understand, model, and predict the competition between aerosols emitted by aviation and pre-existing aerosols in the atmosphere in terms of their contribution to the populations of condensation nuclei and ice nuclei.

The work uses the Met Office NERC Cloud (MONC) model. It is the successor to the Met Office Large Eddy Model (LEM) and is a three-dimensional Large Eddy Simulation (LES)-cloud model. MONC was chosen because of previous experience with the model during the EU-funded ACACIA project, and because the model has been extensively used for atmospheric process research in the past for various liquid, mixed, and ice cloud regimes (e.g., Abel and Shipway (2007); Yang et al. (2012); Hill et al. (2014)). MONC integrates Boussinesq-type equations in time. The Boussinesq equations are linearized momentum equations about small perturbations from a reference base state. If the reference base state is invariant with respect to the height, one obtains the classical incompressible Boussinesq formulation. If the reference base state is height-dependent, the quasi-Boussinesq anelastic approximation is obtained.

MONC is a 3-D model with constant spatial discretization in the horizontal direction, though the discretization can be different in the x and y directions. Vertical spacing can vary with height which allows for higher resolution in specific areas, for example, where turbulent scales are smaller. Periodic boundary conditions are used in the horizontal directions. At the top and bottom, rigid and impenetrable boundary conditions are used.

MONC uses the standard 3-D velocity field ( $u, v, w$ ), the potential temperature perturbation  $T'$  and so-called “q fields” as prognostic variables. The latter can be passive tracers, mass mixing ratios or higher order moments of the water and hydrometeor species (vapor, cloud, ice, snow and graupel). One option to simulate those cloud microphysical variables is to use the CASIM (Cloud AeroSol Interacting Micro-physics) scheme (Miltenberger (2018); Brown et al (2020); Hill (2018)). It is a double-moment (mass and number) cloud microphysics scheme with five hydrometeor classes (cloud liquid, rain, ice, snow and graupel). A gamma distribution is used to describe each hydrometeor size distribution. To transfer mass between the different hydrometeor classes and water vapor, the model represents cloud droplet activation (Abdul-Razzak et al. (1998); Abdul-Razzak and Ghan (2000)), condensation, primary ice formation from cloud droplets (DeMott et al. (2010); DeMott et al. (2015)), freezing of rain drops (Bigg (1953)), secondary ice formation from rime splintering, vapor deposition, evaporation, sublimation, collision-coalescence (between the hydrometeors) and finally sedimentation of all hydrometeors (except for cloud droplets).

In addition, CASIM also represents aerosol activation, ice nucleation processes and in-cloud mechanical processing of aerosol. When aerosol processing is selected, once activated or nucleated, a new prognostic is created which allows for the transport of in-cloud aerosol by cloud dynamics or sedimentation. Furthermore, the representation of the aerosols is made through three soluble modes and one insoluble mode. These modes are described by log-normal size distributions. For each mode, aerosol and number mass mixing ratios are represented.

Previous work with MONC in ACACIA used fixed ice number concentrations (Section 3.3) but since that configuration does not resolve the chain from aerosol to droplet to crystal, it is not appropriate to study the competition between background and aviation aerosols. So a significant effort at the start of Climaviation is to build a configuration where aerosol activation, cloud droplet nucleation, and ice nucleation work together to form a cirrus cloud. MONC represents three modes of soluble aerosols (Aitken, accumulation and coarse) and one insoluble mode (coarse dust). Based on Abdul-Razzak and Ghan (2000), droplets are activated by considering the different soluble aerosol modes while water-supersaturated conditions are required to activate the insoluble aerosol mode. Ice crystals are then formed by homogeneous freezing of cloud droplets, or by heterogeneous ice nucleation (immersion and impact freezing) from insoluble aerosols, as formulated by DeMott et al. (2015).

At the date of this report, two preliminary configurations were built based on the use of coarse soluble mode aerosols initialised with constant mass mixing ratio and number concentration. These profiles are not realistic and are used purely for the sake of testing the aerosol to ice crystal process chain. Four distinct configurations lead to the formation of a stable gravity-wave cirrus cloud. The difference between the configurations lies in the initialisation (or lack thereof) of cloud liquid droplet or aerosol profiles. The different cases are:

1. Fixed cloud case (or control simulation): Cloud droplet number is fixed at  $50 \text{ cm}^{-3}$ . There is no aerosol activation and aerosol processing.
2. Coarse soluble case: The domain is initialized with constant profiles of mass mixing ratio and number concentration of coarse soluble mode aerosol. Aerosol activation and processing are allowed.
3. Cloud liquid case: The domain is initialized with constant profiles of mass-mixing ratio and number concentrations of cloud liquid droplet. For this case, aerosol activation and processing are allowed but all aerosol modes are initialized to zero. This case can be used to add aerosols to a simulation that originally excluded them.
4. Cloud liquid and coarse soluble case (CL + CS or combined case): For this configuration, we combine the coarse soluble case and the cloud liquid case by initialising both the cloud liquid droplet and coarse soluble mode aerosol profiles.

The results of the simulations of each configuration are shown above in Figure 3-1. All configurations lead to the formation of a stable gravity wave cirrus cloud, which is already an achievement. However, several differences can be seen between these different configurations. Firstly, cloud persistence varies (Figure 3-1(a)) with the fixed cloud case being the least persistent and the combined case being the most persistent. This longer persistence is due to smaller ice crystals being created in the combined case (CL + CS) compared to all other configurations (Figure 3-1(b)). Smaller crystals take longer to reach sizes where sedimentation occurs. Despite these differences, the growth rate of ice crystal size and the rate of decrease in ice number concentration (Figure 3-1(c)) are similar in all cases.

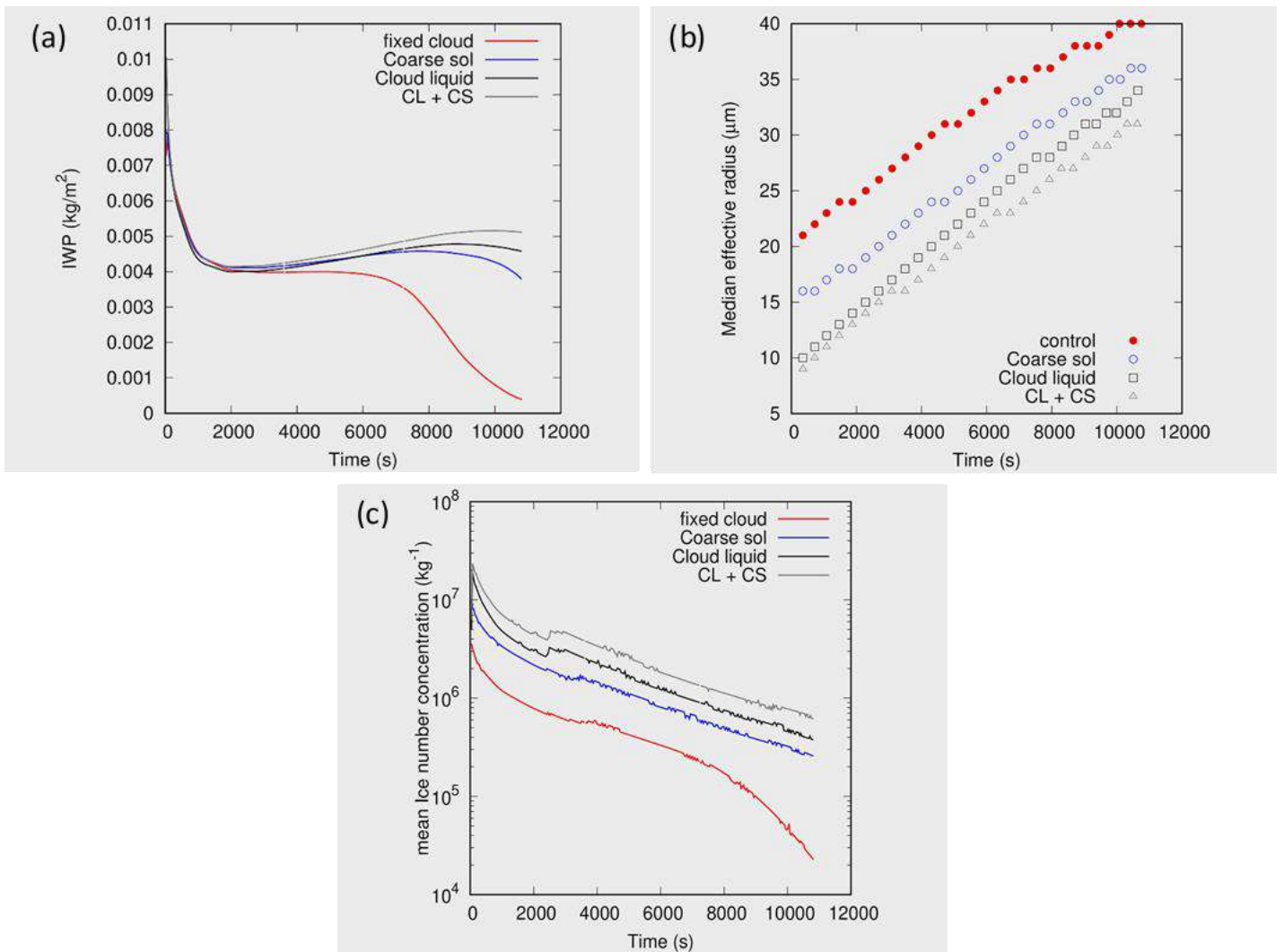


Figure 3-1: (a) Time series of ice water path, in  $\text{kg m}^{-2}$ , for four different initialisations that lead to the formation of a gravity wave cirrus cloud. (See text for details. CL stands for cloud liquid and CS for coarse soluble mode aerosol) (b) Same, but for median effective crystal radius, in  $\mu\text{m}$ . (c) Same, but for ice number concentration, in  $\text{kg}^{-1}$ .

We are now working at identifying possibilities for perturbing clouds simulated by different configurations. Preliminary simulations suggest that adding cloud liquid droplets, which then freeze homogeneously, result in an increase in ice number concentration. In contrast, adding water vapour increases ice crystal sizes through water vapour deposition, without creating new ice crystals. Adding coarse soluble mode aerosol has no effect on the simulated ice cloud. We do not yet know if that lack of response is due to a lack of water vapour or if the sudden addition of aerosols is not being correctly processed by MONC.

### 3.2. WP 3.2: Aerosol transport from aviation

Contributors: Nicolas Bellouin (IPSL), Nicolas F evrier (Masters intern, IPSL)

The objective of this work package is to understand, model, and quantify the time scales that govern the horizontal and vertical transport of aerosols from aviation.

The ability of aviation aerosols to influence pre-existing clouds relies on the hydrophilic properties of these aerosols, which for soot are affected by successive freezing-sublimation cycles in contrails and cirrus clouds (e.g., Mahrt et al. 2020). But to exert a radiative forcing by interacting with clouds, aviation aerosols obviously need to be able to reach pre-existing clouds, either by horizontal transport at the flight altitudes, or by vertical transport to the lower atmosphere. However, particulate and gaseous transport is difficult to simulate properly in the large-scale climate models that provide the radiative forcing estimates (e.g., Gettelman and Chen, 2013; Penner et al., 2018; Righi et al., 2013). Climate models tend to be too diffusive. Unfortunately, it is also difficult to compare to observations. Radioactive particles emitted by nuclear accidents have provided some ways to validate modelled aerosol transport (Kristiansen et al., 2012), but they (fortunately) do not span all regions and seasons. They are also emitted at the surface, thus not representative of aircraft emissions.

This work package is based on simulations by the LMDZ climate model (Hourdin et al. 2020). LMDZ developers have put effort in improving modelled convective transport (updraft, downdraft, tracer release during rain re-evaporation), so it should be a strong point of the model. In a first step, however, the model is run at the coarse horizontal resolution of 5° by 5°. Twenty-four passive tracers have been added to LMDZ. Twelve of these tracers have aerosol characteristics and are removed by dry deposition and by nucleation (in-cloud) and impaction (below-cloud) scavenging. Those wet deposition processes dominate total deposition, as seen many times in climate models. The other twelve tracers have characteristics of an insoluble gas, so are only removed by dry deposition. Their removal is very slow, as expected, and their characteristics are not especially relevant to aviation emissions, so gaseous tracers will not be discussed further. Each aerosol and gas tracer are emitted on 1<sup>st</sup> January at three altitudes (450, 250, and 200 hPa) to represent typical flight altitudes for medium and long-haul flights; as a single pulse or continuous emissions of 1 kg of tracer; and emitted over the North Atlantic or North Pacific flight corridors. Note that the following results are preliminary.

Figure 3-2 shows the time evolution of tracer mass for the aerosol tracers in the case of pulse and continuous emissions. Perhaps unsurprisingly, aerosols emitted lower in the atmosphere are removed more quickly than aerosols emitted higher up. But residence times remain sizeable in all cases: around 20, 50, and 60 days for aerosols emitted at 450, 250, and 200 hPa, respectively. Residence times are increased by emitting directly in the stratosphere, or by transport of emitted tracer into the stratosphere.

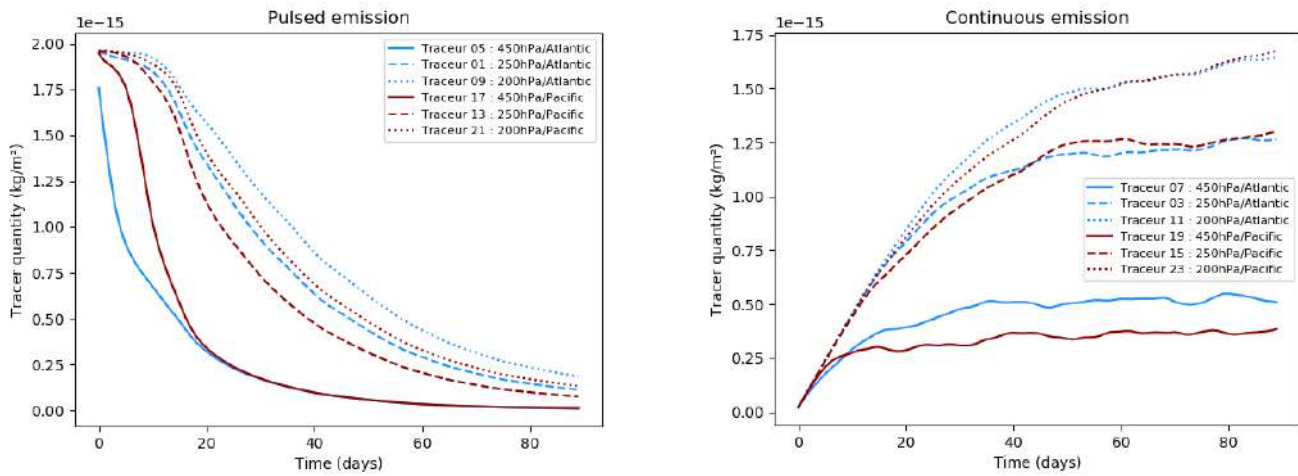


Figure 3-2: Time evolution of globally averaged aerosol tracer burden, in  $\text{kg m}^{-2}$ , in LMDZ climate model simulations with pulse (left) and continuous (right) emissions of 1 kg of tracer on 1st January. Blue and red lines indicate emissions over the North Atlantic and North Pacific flight corridors, respectively. Solid, dashed, and dotted lines indicate the height of the emissions, at 450, 250, and 200 hPa, respectively.

During that time, aerosols are transported over long horizontal and vertical distances. Figure 3-3 shows where the top 95% of aerosol mass is located in the horizontal and vertical after the first day, week, fortnight, and month in the case of an aerosol tracer emitted over the North Atlantic flight corridor at 250 hPa. The tracer goes around the globe several times and after a month cover a sizeable fraction of the North Hemisphere and the whole atmospheric column. Within two weeks it would potentially be interacting with warm clouds in the lower atmosphere. The descent happens within the relatively dry subtropical subsidence zone, which is associated with boundary layer clouds, including stratocumulus decks. These clouds have a large contribution to planetary albedo, so changing their microphysical properties could potentially translate into a large radiative forcing. However, recall that total tracer mass strongly decreases in time, as shown in Figure 3-3, so co-location between tracer and cloud does not imply substantial interactions.

The next step in that analysis is to sample different meteorological conditions by varying the emission date and year, and implement soluble gaseous tracers, which may reach the lower atmosphere to be oxidised into aerosols more easily than primary aerosol emissions. In the coming months, we will also compare model simulations with ensemble forward trajectories with the HYSPLIT model, to try and quantify whether atmospheric transport simulated by the climate model is reasonable.

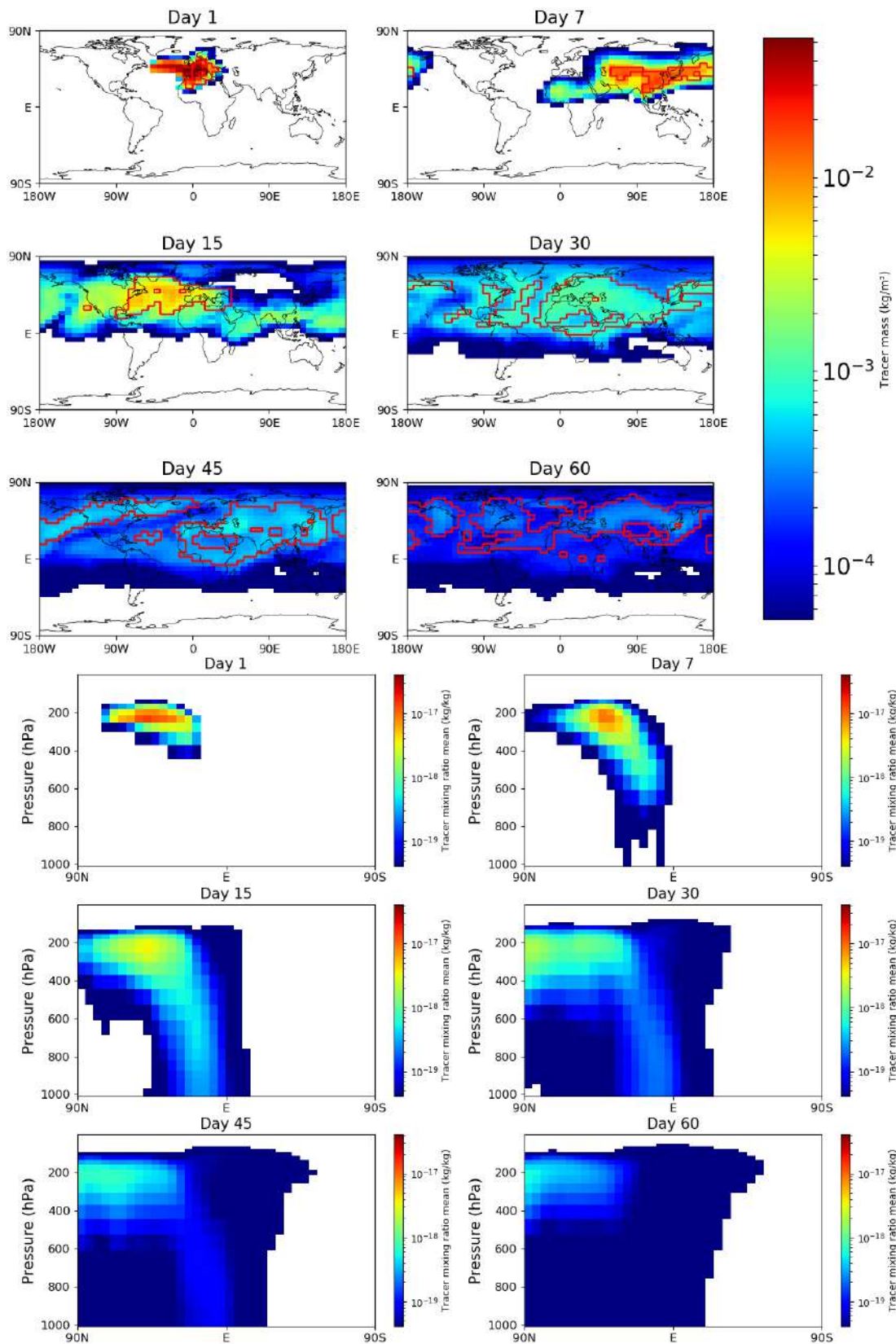


Figure 3-3: Horizontal (top four panels) and vertical (bottom four panels) tracer distributions after 1, 7, 15, and 30 days in a LMDZ climate model simulation. Here, the tracer is an aerosol emitted in the North Atlantic flight corridor on 1st January at 250 hPa. Red contours indicate where the top 95% of tracer mass is located.

### 3.3. WP 3.3: Cloud response

Contributors: Jhaswantsing Purseed (postdoctoral researcher, IPSL), Nicolas Bellouin (IPSL), Beatrice Altamura (Masters intern, IPSL)

The objective of this work package is to understand, model, and predict the response of liquid, ice, and mixed clouds to a perturbation of their droplet and/or crystal numbers.

Activities in the first year of Climaviation have focused on cirrus clouds, using a MONC configuration with fixed ice crystal number. Work done by Dr Ella Gilbert of the University of Reading as part of the EU-funded ACACIA project was replicated to benchmark the porting of MONC to Linux, which was done with some pain at the start of Climaviation. The numerical domain is 6 km x 6 km x 22.5 km with a grid spacing in the horizontal directions of 100 m. Grid spacing in the vertical is 117.8 m, with 191 levels starting at the surface. Profiles for the potential temperature, horizontal velocity and water vapor are initialised according to measurements of a “gravity wave” cirrus by Yang et al. (2012). That cirrus is characterised by fast updrafts velocities (larger than  $10 \text{ cm s}^{-1}$ ), leading to lifting and homogeneous freezing of supercooled droplets (Krämer et al., 2020). Although it is unlikely that an aircraft would fly through such a cirrus cloud, it can still be influenced by aviation aerosols transported from flight corridors. Simulations of a different type of cirrus, called warm conveyor belt cirrus following Krämer et al. (2020) are available from ACACIA, based on initial conditions from Spichtinger et al. (2005). Warm conveyor belt cirrus is associated with slow updraft velocities and dominated by heterogeneous nucleation of ice crystals. The results obtained from this type of cirrus are shown and discussed in Section 3.3.2. Those results replicate perfectly those obtained during ACACIA, giving confidence that our port of MONC to Linux is scientifically valid. Response studies will now move to the aerosol-activation configuration of MONC discussed in Section 3.1.

#### 3.3.1. *Gravity Wave cirrus*

The gravity wave cirrus case simulates 11000 seconds. Heterogeneous ice nucleation occurs in the first few seconds and is followed by a spin-up phase until mass fluxes into and out of the ice reservoir get stable. This is shown by the red curve in Figure 3.4(a), where ice water path reaches a stable solution at about  $t = 1800 \text{ s}$  and persists until approximately  $t = 6000 \text{ s}$ . After that, crystals have reached sedimentation sizes and the cloud begins to dissipate. The simulated cirrus is located between 8 and 9.5 km.

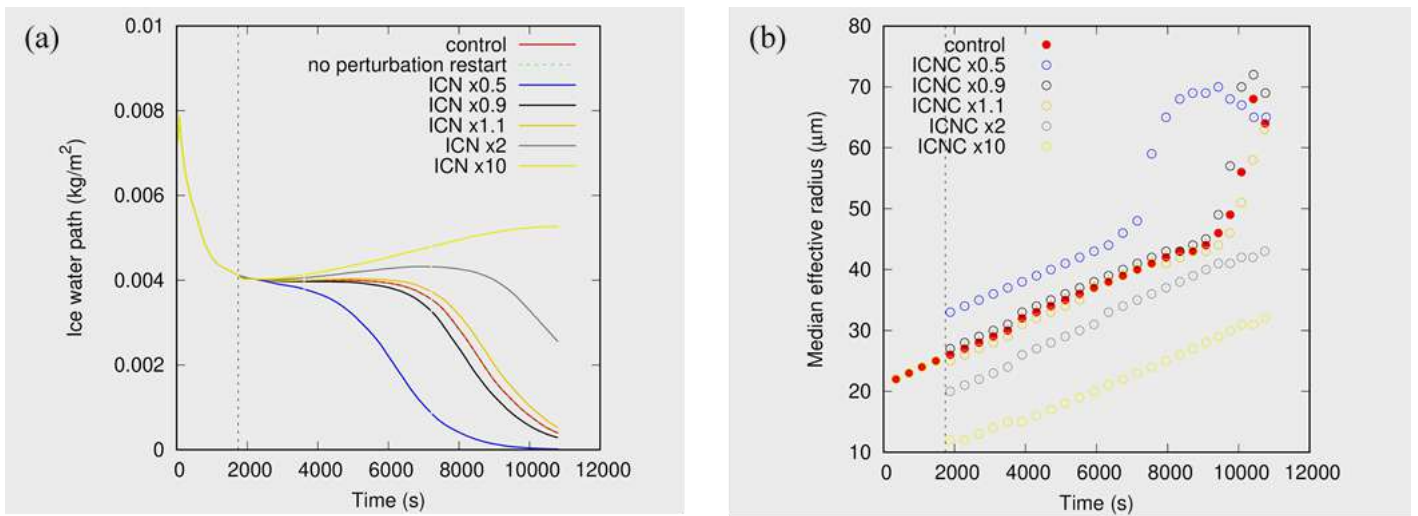


Figure 3-4: MONC simulations of a gravity wave cirrus cloud. The control (unperturbed) cloud is shown in red, and perturbations of 1.1, 2, 10, 0.9 and 0.5 times the initial ice crystal number concentrations are shown in orange, grey, yellow, black and blue respectively. Panel (a) shows the ice water path, in  $\text{kg m}^{-2}$ , as a function of time. Panel (b) shows the median of the ice crystal effective radius as a function of time. The dotted line shows the end of the spin-up phase when perturbations are applied.

The simulated cirrus cloud is then perturbed by either increasing or decreasing the ice crystal number concentration. The perturbation is applied instantly at the end of spin-up phase, by editing the checkpoint file (which stores flow dynamics and micro-physical cloud dynamics variables) created by the control simulation at that time. Ice crystal number concentrations (ICNC) are multiplied by 0.5, 0.9, 1.1, 2 and 10 throughout the simulated cloud. The consequences of these perturbations are shown in Figure 3-4. For the cases where the ICNC is increased, an increase in the ice water path is seen, with a delay in the dissipation of the cloud. Inversely, when the ICNC is decreased, the rate of dissipation of the cloud is increased. Figure 3-4(b) shows the median value of the ice crystal effective radius as a function of time. The offset seen at the time when the perturbations are applied is a direct consequence of increasing or decreasing the ICNC. Since ice water content has not (yet) changed, increasing (decreasing) the ICNC instantaneously results in smaller (larger) ice crystals. Ice crystal size then drives subsequent evolution, where the more numerous but smaller ice crystals take on more water vapour, increasing ice water path, but sediment more slowly, delaying the dissipation of the cloud. The ice water path response seems proportional to the initial ICNC perturbation, as discussed in Section 3.3.3. Decreasing ICNC has the opposite impact of accelerating sedimentation rates, leading to the dissipation of the cloud before the end of the simulation. The growth rate of the ice crystal effective radius seems to be unaffected by the perturbations (Figure 3-4 (b)), probably because water vapor is not a limiting factor in those simulations.

### 3.3.2. Warm conveyor belt cirrus

In this section, simulations are for a warm conveyor belt cirrus based on the initial conditions given by Spichtinger et al. (2005). The procedure used for these simulations is similar to that described in the previous section on the gravity-wave cirrus. Here, the domain is 6 km x 6 km x 16 km with a grid spacing of 100 m in the horizontal directions and a vertical spacing of 116.75 m with 136 levels starting from the surface. The cirrus is run for a total time of 11000 s with the spin-up phase lasting for approximately 4000 s, as in Figure 3-49(a). The cloud persists till  $t = 8000$  s then dissipates as ice converts to snow and snow to graupel increases. The simulated cirrus is situated between 9.5 and 10 km. By comparison, the gravity wave cirrus forms between 8.5 and 10 km.

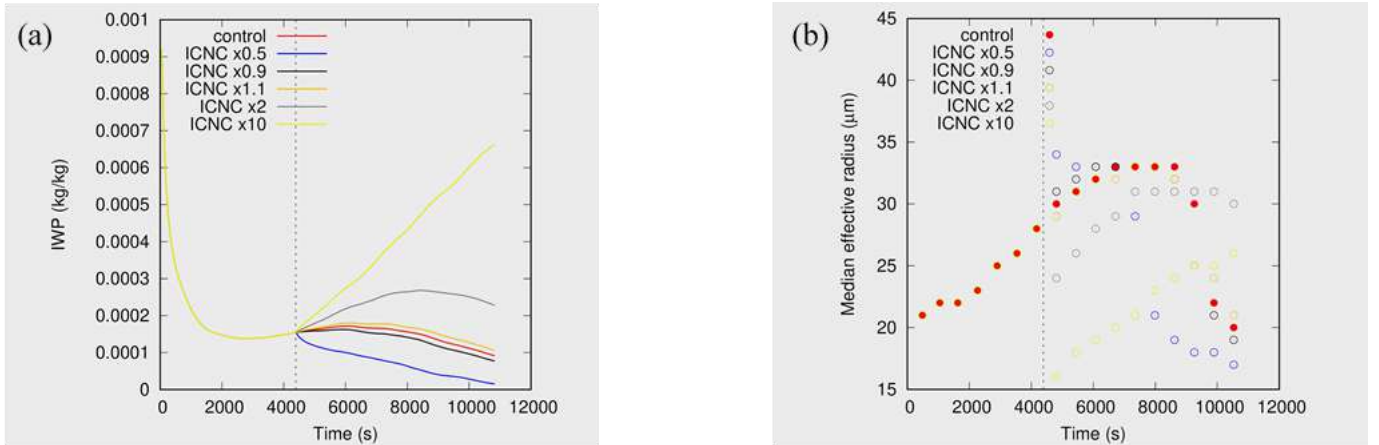


Figure 3-5: MONC simulations of a warm conveyor belt cirrus cloud. The control (unperturbed) cloud is shown in red, and perturbations of 1.1, 2, 10, 0.9 and 0.5 times the initial ice crystal number concentrations are shown in orange, grey, yellow, black and blue respectively. Panel (a) shows the ice water path, in  $\text{kg m}^{-2}$ , as a function of time. Panel (b) shows the median of the ice crystal effective radius as a function of time. The dotted line shows the end of the spin-up phase when perturbations are applied.

As done in the gravity-wave cases, the warm conveyor belt cirrus is perturbed by either increasing or decreasing the ice crystal number concentration. The consequences of these perturbations are shown in Figure 3-5(a) and Figure 3-5(b). The responses of the ice water path and the median effective radius are similar to the gravity-wave case and are qualitatively explained by the same mechanisms.

### 3.3.3. Response of gravity-wave and warm conveyor belt cirrus

Figure 3-6 shows the changes in ice water path and ice crystal number between perturbed and control simulations. The post-perturbation phase of the clouds' evolution differs quantitatively between each case. The warm conveyor belt cirrus response is characterised by a  $d \ln IWP / d \ln N_i = -20$  approximately. The gravity-wave cirrus response is more muted, at  $d \ln IWP / d \ln N_i = -2$  approximately. The reasons for this difference will be explored in the next steps of the work. At the end of the simulation, there is a striking similarity between the dissipation phase of the perturbed clouds in both cases. They follow a  $d \ln IWP / d \ln N_i = \frac{5}{3}$  approximately.

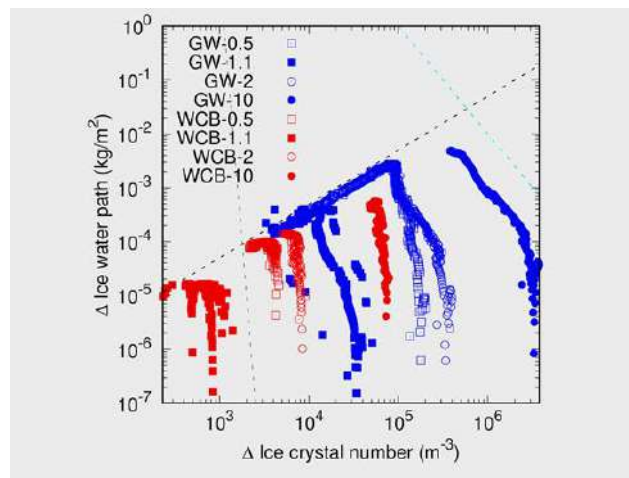


Figure 3-6: Change in ice water of path, in  $\text{kg m}^{-2}$ , as a function of the change in ice crystal number, in  $\text{m}^{-3}$ , due to initial perturbations of ice crystal number. The gravity-wave cirrus case is shown in blue, and the warm conveyor belt cirrus is in red. Initial ice crystal number if multiplied by 0.5 (squares), 1.1 (filled squares), 2 (circle), 10 (filled circles). The black, blue sky and grey dotted lines represent the power laws  $\sim x^{5/3}$ ,  $\sim x^{-2}$  and  $\sim x^{-20}$  respectively.

## 4. AXIS 4: OBSERVATIONS

The objectives of the fourth axis of research are to gather existing data and acquire additional observations to extract information that will allow an evaluation and a recalibration of the mainly numerical results on which the study of atmospheric mechanisms is based.

### 4.1. WP 4.1: Use of existing data

Contributors: Kevin Wolf (postdoctoral researcher, IPSL), Nicolas Gourgue (research engineer, IPSL), Sylvain Cros (contractor, FX-Conseil)

The objective of this work package is to survey existing observational data on contrails and to develop algorithms for large-scale processing to create a database that can be used to evaluate and recalibrate the results obtained by numerical simulation to describe the evolution of contrails at different scales.

#### 4.1.1. Radiosonde observations

Twice-daily radiosonde observations are used to investigate the frequency of potential contrail and contrail cirrus occurrence. The vertical distributions of potential contrail formation are separated for seasons, contrail type, propulsion efficiency, and fuel type. At the time of writing this report, the radiosonde analysis is based on an 8-year dataset of temperature and humidity profiles from Palaiseau, France, in the greater Paris region. The observations and statistics are compared with re-analysis data from ERA 5 provided by the European Centre for Medium-Range Weather Forecasts (ECMWF).

Figure 4-1 shows the spatial distribution of the radiosonde dataset. Focusing on the upper troposphere, the heatmap in Figure 4-1(b) is of particular importance. The map shows that the majority of the measurement are obtained east of the launching site (marked by the black dot), which is related to predominantly westerly winds. On average, the radiosondes are advected between 1° to 1.5° (70 to 100 km) eastward from Palaiseau. Individual observations can reach further.

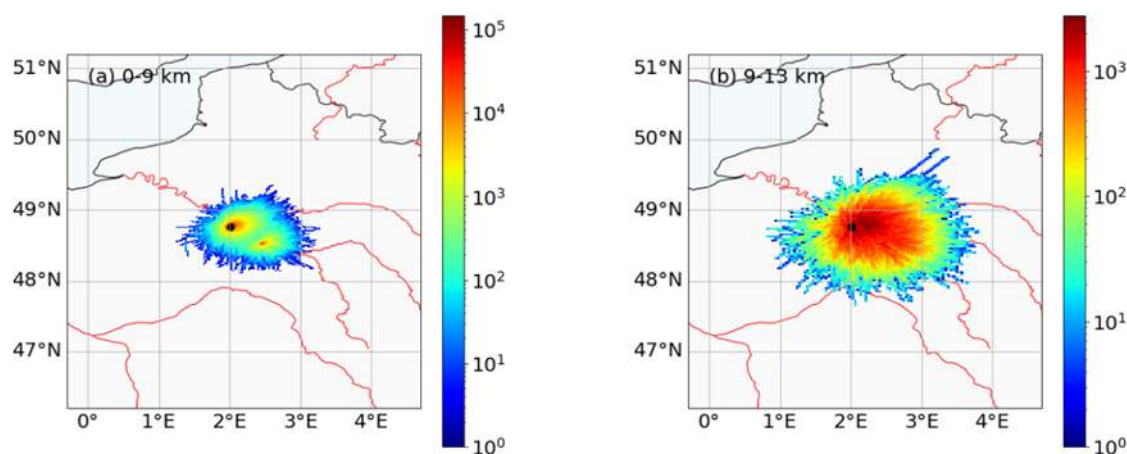


Figure 4-1: Spatial distribution of the 8-year radiosonde dataset for altitudes between (a) 0-9 km and (b) 9-15 km.

Before September 2011 the Meteomodem “M2K2-DC” radiosonde was used, before being replaced by the “M10” model. Measurements are corrected for the relative humidity bias due to solar heating of the sensor and for sensor time-lag.

After corrections, the individual radiosondes profiles are flagged for non-persistent (NP) and persistent (P) contrails. The categorization is based on the Schmidt-Appleman criterion (S-A-c, Schumann (1996)). The S-A-c provides threshold values for temperature and humidity depending on the ambient pressure as well as engine-specific parameters. For cases when the ambient air is below the temperature threshold and the ambient humidity is above the humidity threshold, a layer is flagged as a NP contrail. If a layer fulfills the S-A-c and is additionally supersaturated with respect to ice (ice-supersaturated regions short ISSR) the measurement point is categorized as a P contrail. Unless otherwise stated, the profiles are derived for kerosene (JetA1) powered engines and a common value of propulsion efficiency  $\eta = 0.3$ .

Based on the S-A-c and ISSR constrain, three distinct regions in the saturation-pressure-temperature diagram are assigned. These regions are indicated in Figure 4-2. Region 1 (R1) represents ice-supersaturated atmospheric conditions fulfilling the S-A-c. These are considered as potential formation regions for P contrails. Region 2 (R2) are conditions not fulfilling the S-A-c but the requirement for ice-supersaturation, while region 3 (R3) only satisfies the S-A-c. R2 and R3 are both potential formation regions for NP contrails.

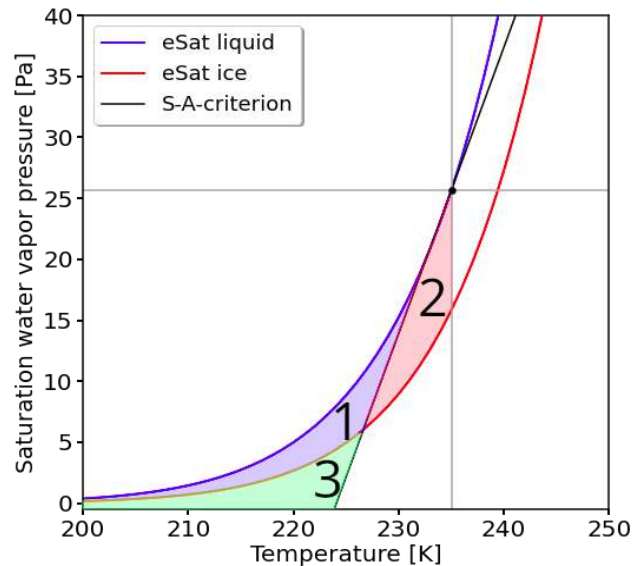


Figure 4-2: Saturation-pressure-temperature diagram. Saturation water vapour pressure over ice (red line) and over liquid water (blue line) as a function of the absolute temperature. Regions of potential contrail formation are indicated by the coloured areas. Critical temperature and relative humidity, determined by the Schmidt-Appleman-criterion, are indicated by the black line.

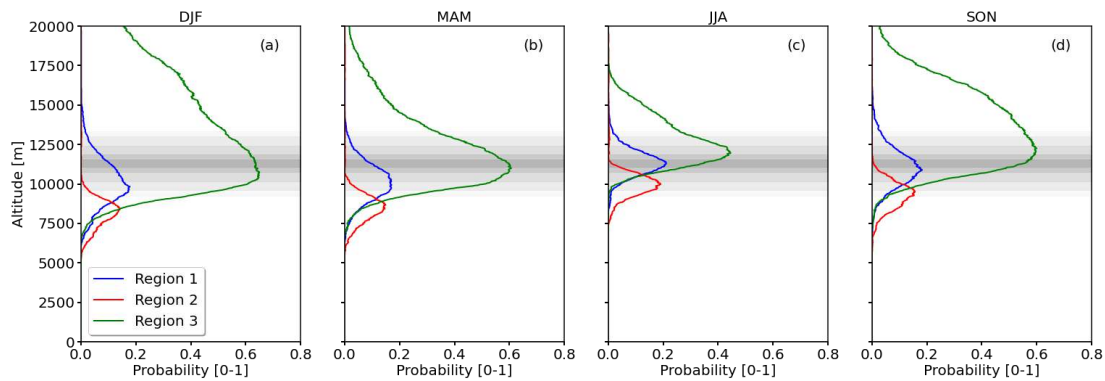


Figure 4-3: Seasonal vertical probability distribution of potential non-persistent (region 2 and 3) and persistent contrails (region 1). The flight altitude distribution is provided by the grey shading indicating the 25, 50, and 75% quantile.

Figure 4-3 shows the resulting vertical distributions of potential NP and P contrail formation separated for seasons of the year. R3 conditions occur most frequently with a maximum of 60% between 10 and 12.5 km altitude. Fewer occurrences are determined for R2 and R1 at around 20%. A seasonal variation is observed with generally highest occurrences in winter, followed by autumn, and spring. Lowest occurrences appear in summer.

Using Automatic Dependent Surveillance–Broadcast (ADS-B) data recorded at Palaiseau the vertical, mean flight altitude distribution (FAD), i.e., mean cruising altitude, of air traffic is derived. In Figure 4-3, the 25, 50, and 75% quantile of the FAD are indicated by the gray shading. Figure 4-3 shows that the maxima of the FAD and the occurrence of R1 as well as R3 overlap. Thus, there is a high probability for contrail formation at these altitudes. To determine occurrence of contrails, the distributions from Figure 4-3 are convoluted with the FAD. The resulting distributions are shown in Figure 4-4.

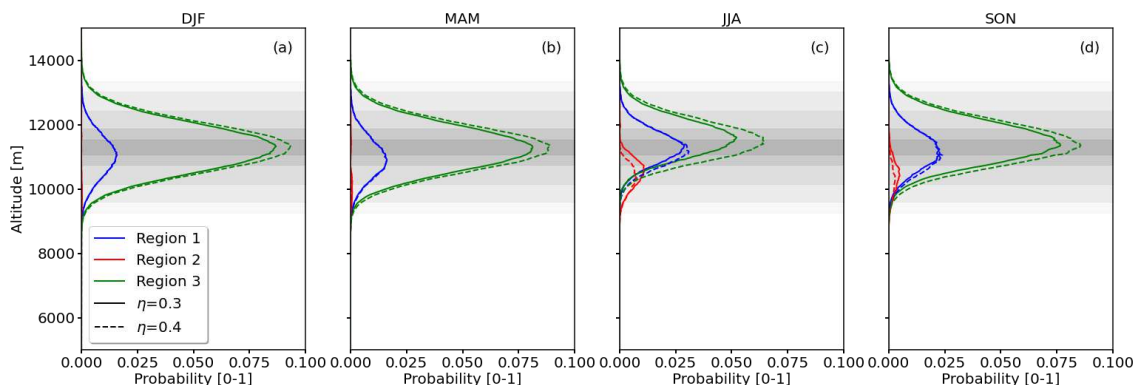


Figure 4-4: Seasonal vertical probability distribution of potential non-persistent (R2 and R3) and persistent contrails (R1) weighted by the flight altitude distribution. The flight altitude distribution is shown by the grey shading indicating the 25, 50, and 75% quantile. Variations in propulsion efficiency of  $\eta = 0.3$  (solid) and  $\eta = 0.4$  (dashed) are indicated.

After weighting the distributions, the vertical profiles are still dominated by R3 contrails. The FAD is invariant in time and, hence, the maximum occurrence of R3 is detected for winter and the minimum in summer. Generally lower probabilities are determined for R1 and R2 contrails, with P contrails being more frequent in summer and almost nonexistent in winter.

Within the last decades the efficiency of jet engines and the related propulsion efficiency  $\eta$  has increased. This process is likely to continue in the future. The increase in efficiency is mainly achieved by converting a larger fraction of the chemical energy from the fuel into kinetic energy instead of thermal energy. Consequently, the exhaust plume of the engine gets colder and super-saturation is reached earlier and more frequently. Therefore, the chance for NP and P contrail formation increases.

Figure 4-4 shows a scenario for a propulsion efficiency of  $\eta = 0.4$ . It indicates that the frequency of NP contrails increases throughout the year with the largest gain in summer, which is partly related to the transition from R2 to R3 type contrails. Additionally, a shift of the peak of the distributions towards lower altitude is detected. For P contrails no significant change is seen. Generally, an increase in propulsion efficiency is likely to cause more contrails in the future.

Another approach to turn into more environmental-friendly aviation and to become independent from fossil fuels are alternative combustibles like hydrogen or bioethanol. Both combustibles have in common that they release more water vapor per unit energy during the combustion process than kerosene. This will alter the likelihood of contrail formation and their vertical distribution.

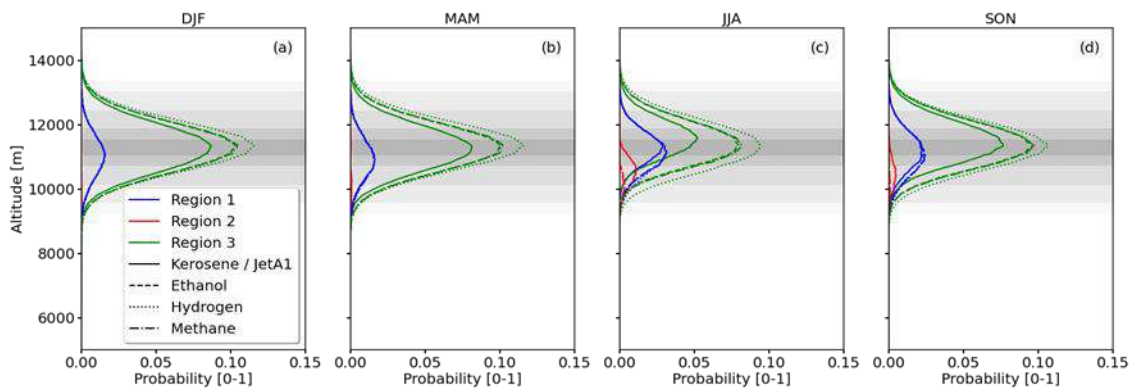


Figure 4-5: Seasonal vertical probability distribution of potential non-persistent (R2 and 3R) and persistent contrails (R1) weighted with flight altitude distribution. The flight altitude distribution is shown by the grey shading indicating the 25, 50, and 75% quantile. Distributions are shown for kerosene (solid), ethanol (dashed), hydrogen (dotted), and methane (dashdot).

Figure 4-5 shows vertical distributions of R1 to R3 of resulting from ethanol (dashed), hydrogen (dotted), and methane (dash-dot). For reference, the distribution of kerosene (solid) is given. While a transition to hydrogen or purely ethanol-powered engines is unlikely in the short term, flight tests with mixtures of kerosene and ethanol are already underway. The distributions shown in Figure 4-5 show the maximum effects of a full fuel-transition on contrail occurrence.

The analysis and resulting Figure 4-5 indicate that the occurrence of contrails will increase when a transition to ethanol and hydrogen takes place. In general, hydrogen causes the largest increase in NP and P contrail formation and is followed by methane and ethanol. The largest gain is detected for NP contrails independent of fuel type. A smaller increase is detected for P contrails. Even though the increase in P contrails appears marginal, these types of contrails have the largest radiative effect, causing so call “big hits” (Teoh, 2020), as they can persist over several hours or days. However, flying with bioethanol and hydrogen avoids the emission

of carbon dioxide, which impacts the climate on time scales of decades. This leads to a trade-off, which has to be evaluated especially during the transition phase of mixed fuels.

One of the overarching objectives of Climaviation is the mitigation of contrail formation. A potential strategy is circumventing ISSR, by adapting flight altitudes according to the seasonal variations of contrail formation shown in Figure 4-5. To estimate the effectiveness of flight deviations, the vertical distributions from Figure 4-3 are shifted vertically against the FAD to reduce the occurrence of actual contrails. Mathematically the area under the graphs shown in Figure 4-5 is minimized. The results are presented in Figure 4-6.

Figure 4-6 shows that flight deviations are seasonally dependent. During summer and autumn, a decrease in average flight altitude is likely to reduce the average number of contrails. Deviations of up to 2 km might be limited by economical operation procedures, but even slight deviations from the standard altitude towards lower levels will decrease the average contrail occurrence. Smaller effects of flight altitude changes are found for spring and winter. It has to be emphasized that shifting flight tracks upward poses the risk of contrail formation in the lower stratosphere, where residence times can significantly exceed the lifetime of contrails in the troposphere (Gierens 1999, Irvine 2013). It can also affect the lifetime of NOx and aerosol emissions, and their radiative impacts.

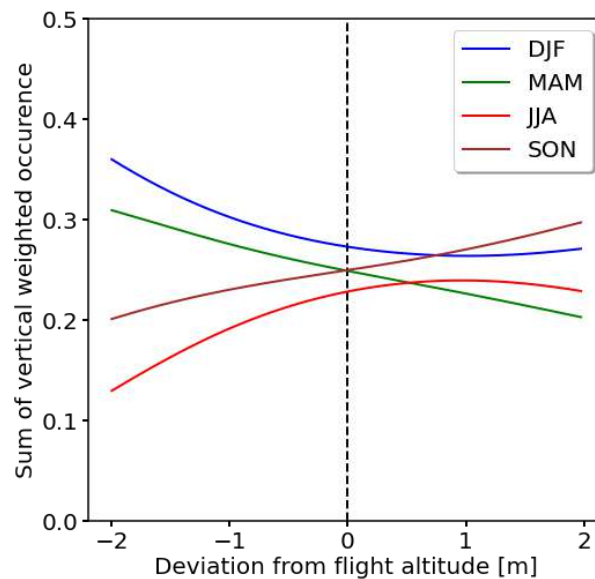


Figure 4-6: Minimization of the contrail occurrence by shifting average flight altitude. Colours represent the seasons of the year.

In addition to the statistical occurrence of contrails it is of interest for flight planning to detect potential contrail formation on a day-to-day basis. It is known from previous studies that contrails are likely to be present in proximity of the thermal tropopause layer (TTL) and around the jet stream (Spichtinger, 2003; Irvin, 2012; Diao, 2015). Both can be regarded as proxies to identify the location of contrail formation.

The location of the TTL is determined by following the definition of the World Meteorological Organization, which defines the location of the tropopause layer on basis of the vertical temperature profile, i.e., the lapse-rate  $\gamma$ , which is calculated by:

$$\gamma = \frac{dT}{dz} = \frac{T_2 - T_1}{z_2 - z_1}$$

with  $T_1$  and  $T_2$  the lower and upper temperature of an infinitesimal layer, respectively, and  $z_1$  and  $z_2$  the corresponding altitudes. The lower boundary of the TTL is located, where  $\gamma$  decreases to  $2 \text{ K km}^{-1}$  and the average  $\gamma$  of the overlying 2 km of atmosphere do not exceed  $2 \text{ K km}^{-1}$  (WMO, 1957). The jet stream altitude is determined by detecting the layer where the highest wind speed occur and are higher than  $30 \text{ m s}^{-1}$  (WMO, 1958). For profiles that does not meet the above criteria and the TTL or the jet stream are undetectable the entire profile is excluded from the analysis.

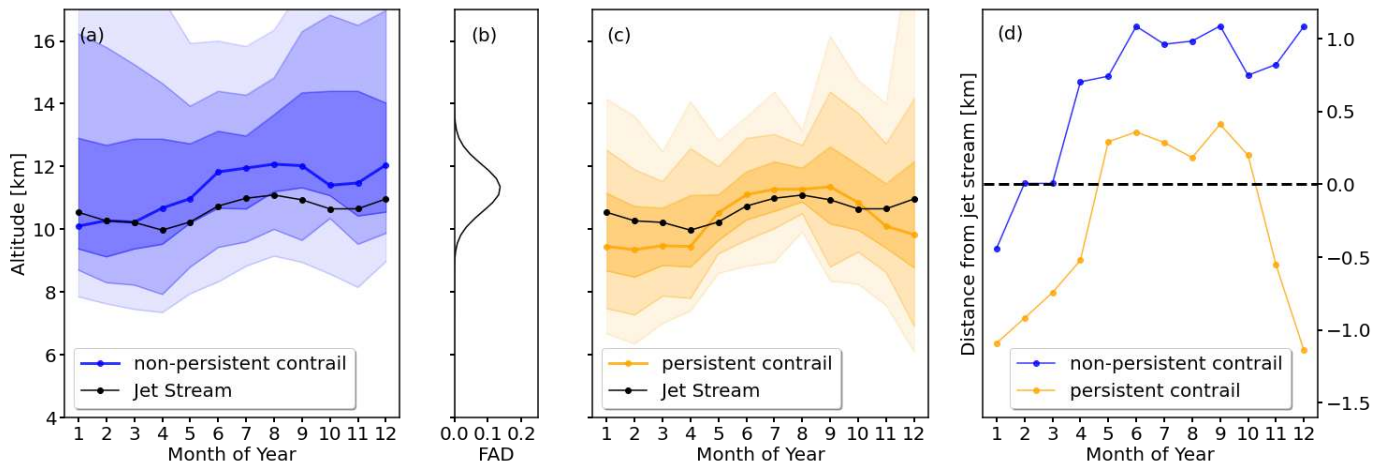


Figure 4-7: (a) Monthly vertical distribution of potential non-persistent contrails with median altitudes (solid, blue line) and quantiles (shaded areas). The mean altitude of jet stream is given in black. (b) Vertical flight altitude distribution. (c) Monthly vertical distribution of potential persistent contrails with median altitudes (solid, orange line) and quantiles (shaded areas). (d) Distance between median jet stream altitude and the non-persistent and persistent contrail regions.

Figure 4-7a shows the median altitude of NP contrails (blue, solid) and the 25, 50, and 75% quantiles. The median altitude of the jet stream is indicated in black. Figure 4-7b shows the distribution for P contrails. The distance between median contrail and jet stream altitude is given in Figure 4-7d.

The analysis indicates that NP contrails are likely to form between 0.5 and 1 km above the jet stream. Persistent contrails appear closer to the jet stream, located between 1 km below and 0.5 km above. Within the given boundaries the formation of contrails follows the position of the jet stream throughout the year. The close spatial correlation poses a problem as aircraft frequently use the jet stream to minimize fuel consumption on eastbound flights and are, as the analysis suggest, therefore flying in the region with the highest chance for contrail formation.

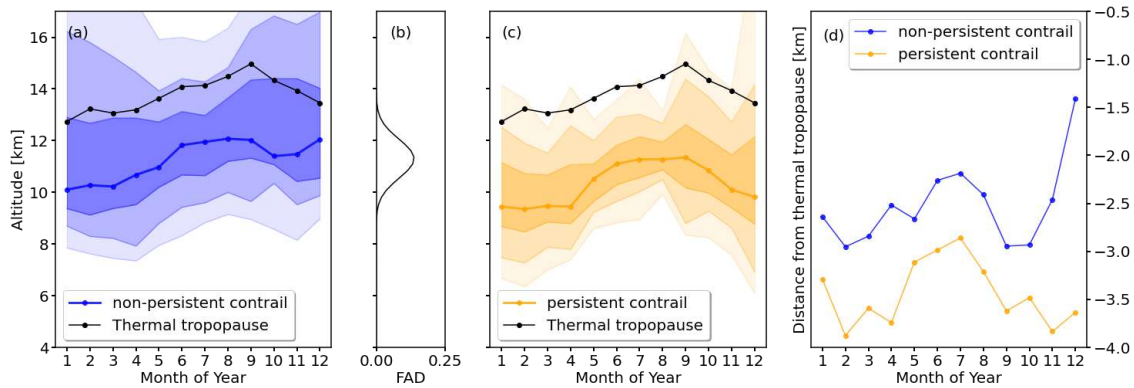


Figure 4-8: (a) Monthly vertical distribution of potential non-persistent contrails with median altitudes (solid, blue line) and quantiles (shaded areas). The mean altitude of TTL is given in black. (b) Vertical flight altitude distribution. (c) Monthly vertical distribution of potential persistent contrails with median altitudes (solid, orange line) and quantiles (shaded areas). (d) Distance between median TTL altitude and the non-persistent and persistent contrail regions.

While jet stream location is a useful tool in combination with global radiosonde observations, the TTL is suited to detect potential contrail formation in weather and climate models. Figure 4-8 shows vertical distribution of NP and P contrails (analog to Figure 4-7) in relation to the TTL, which is given by the black line. The distance between median contrail and TTL altitude is given in Figure 4-8d. Panels 4-8a and c show median altitudes for TTL and NP and P contrails, respectively. During winter, a continuous increase towards the maximum occurring in September is detected. The distance between TTL and contrail median altitude is almost constant during the year with a variation of around one kilometer. On average, P contrails appear up to 4 km below the TTL and NP contrails are around 3 km below the TTL. This correlation is expected as contrail formation depends on the ambient temperature.

To actively assist in re-routing flights and avoiding contrail regions, weather models must be able to accurately predict these regions in space and time. Using the radiosonde dataset, the performance of the ERA5 model is tested with respect to contrail representation. For comparability, collocated, vertical profiles of temperature and relative humidity are extracted twice-daily from ERA5. To account for the vertical resolution of ERA5, radiosonde observations are interpolated on the vertical grid resolution of the model. The vertical profiles are then categorized into P1-P3 in the same way as the radiosonde observations.

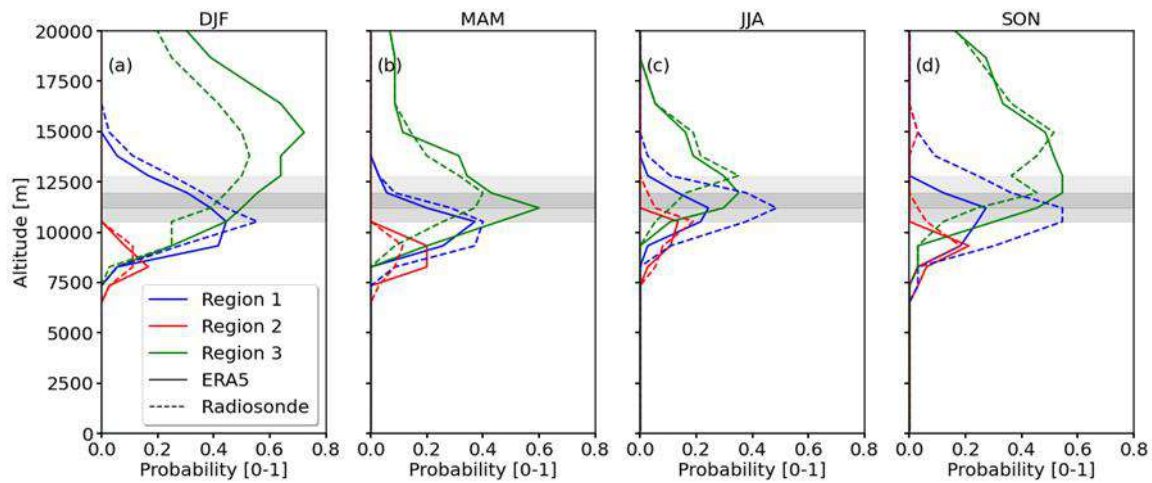


Figure 4-9: Seasonal vertical probability distribution of potential non-persistent (region 2 and 3) and persistent contrails (region 1) from ERA5 (solid) and the interpolated radiosonde observations (dashed). The flight altitude distribution is shown by the grey shading indicating the 25, 50, and 75 quantiles.

Figure 4-9 shows vertical distributions of R1-3 based on ERA5 and radiosondes. In general, the vertical positions of R1-R3 derived from the radiosondes and ERA5 match. For R1-R3 the smallest differences appear in spring. Increased discrepancies are present in summer and autumn with a clear underestimation of R1 by ERA5. The lower frequency of occurrence is likely caused by an underestimation of relative humidity in ERA5, which is a known issue (Lamquin, 2009; Lamquin, 2012). Largest differences for R3 are found during winter, where ERA5 overestimates the occurrence compared to the radiosondes.

The unsystematic discrepancies between radiosonde and ERA5 indicate that multiple intertwined effects are involved, which require a more in-depth analysis in the coming months.

#### 4.1.2. Automatic contrail detection and segmentation

The aim of this task is to automatically detect contrails to create a sufficiently representative database of contrail evolution to improve the numerical models. This task uses a hemispheric camera located at Ecole Polytechnique (Palaiseau, south of Paris) and run by SIRTA. The camera takes a picture every 2 minutes at an image resolution of  $768 \times 1024$  pixels (Figure 4-10). With each image we have a radar file that gives the position of every aircraft in a zone around of Palaiseau. So we know if an aircraft is above SIRTA and the camera. For the beginning of this task, the goal is to detect the planes near the camera and the position of the aircraft. We then look for a contrail behind the aircraft and then we follow the evolution of this contrail.

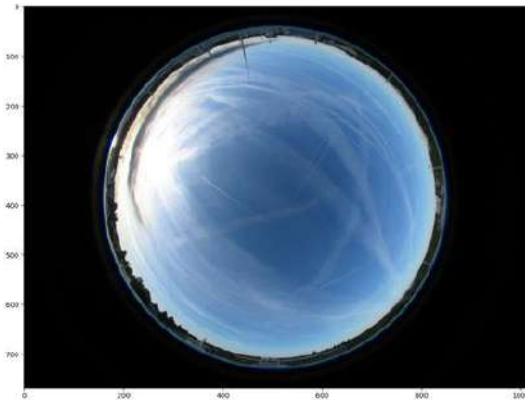


Figure 4-10: Raw image with the SIRTA camera

### Algorithm

To simplify the detection task, we look for the contrail where it is created just behind the aircraft. We have a radar file to know where each aircraft is, but to do a proper search with this information, we need to create a link between the real world and the image coordinates. We call this first step angular calibration. Then, for each plane we use a top-hat algorithm to contrast small bright objects from the darker background. And finally, we search for line shapes using a Hough line transform. Data is saved after each detection to continue the detection with the next image. We then create a metric to evaluate this algorithm.

### Cloud detection

First, we use a cloud detection algorithm (Lothon et al. (2019)). With this we determine the proportion of clouds in the image. If we have more than 90% of cloud, the image is not processed further.

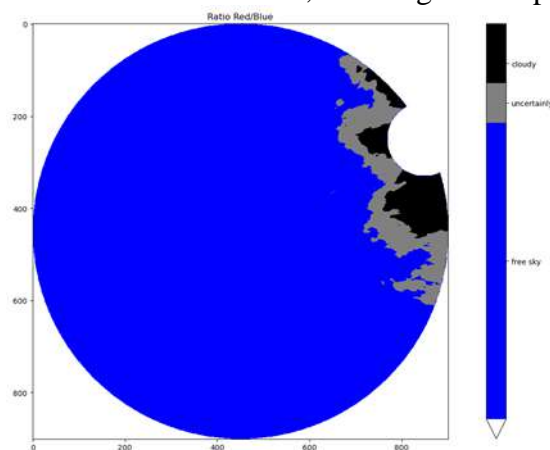


Figure 4-11 : Cloud detection

### Angular Calibration

We use a solar calibration method (Urquhart et al. (2016)). With this method the Sun is the reference, but it only covers a small part of the image. Currently we are looking for a way to use contrail to add references to other parts of the image. At the moment we have a good set of parameters but in some images, we have a discrepancy between the position of the plane and the contrail. So, the calibration needs to be improved.

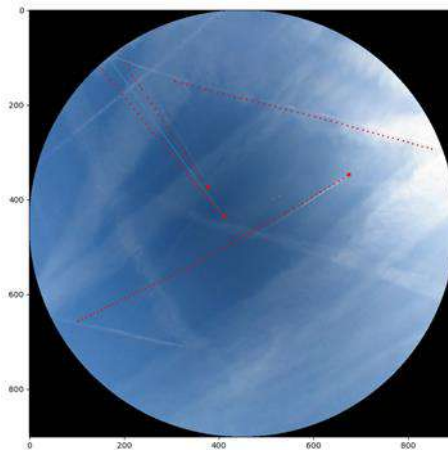


Figure 4-12: Image with plane projection

### Top-hat and filter

With the angular calibration we can approximate the trajectory of the aircraft on the image. We use a weather model to estimate wind speed and direction. With the aircraft trajectory and wind, we determine a small area on the image where contrails can appear. We use a top-hat function to contrast the small bright features of the contrails against the darker background of the sky. A contrail is normally white on a blue background. Top hat works on a grey scale image. We apply a top-hat function on each channel and sum the results, then use a hysteresis filter. We generate a histogram after the top-hat to eliminate artefacts, as contrails are brighter at the beginning but degrade until they disappear. Hysteresis uses all pixels whose value greater than 80% of maximum and keeps the direct neighbours. Each group of pixels is kept only if they have more than 20 pixels and if the length/width is larger than 3, to keep a line shape.

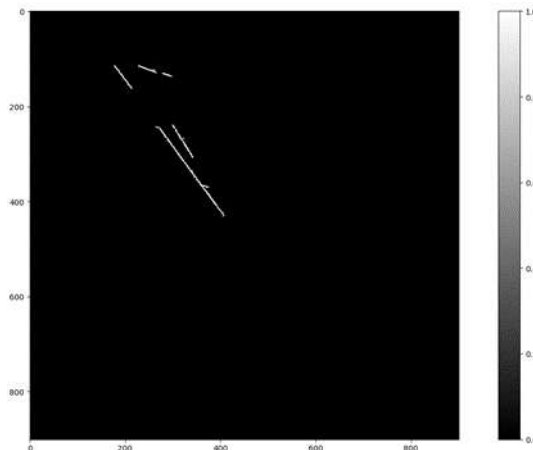


Figure 4-13: Output after TopHat filter on value and filter on form

### Hough line transform

At this stage we normally only have lines. So we look for the line with an angle closest to the plane of the trajectory. If a group of pixels passes all tests it is labelled a contrail. We remove the contrail in the mask and move to the next aircraft.

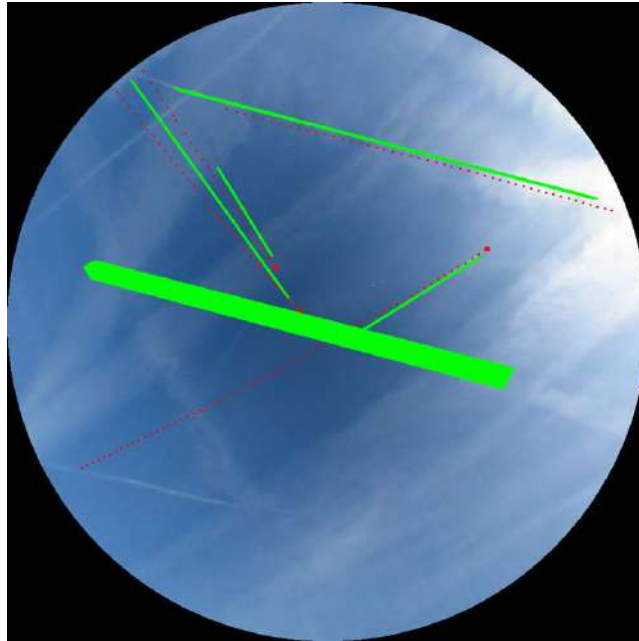


Figure 4-14: Output image. Green contrail detection, red plane trajectory

## Evaluation

To improve the algorithm, we need to devise a way to evaluate it. We therefore set as metric the minimum distance between the algorithm's detection and manual measurement and divide by maximum distance. We make the hypothesis that manual and automatic detections completely overlap. This is verified in most cases. In some cases, automatic detection falls short or detects a longer contrail than the manual measurement. In extremely rare (3 cases out of 130) cases there is no complete overlap, and the metric fails. We only include images where the algorithm detects a contrail so false negatives are underestimated but we sample all false positive cases. The average metric for the moment is close to 0.5.

The next step is to create a dataset to train an artificial intelligence algorithm to make it easier to correct false positive. But we need to filter very precisely the contrail detection.

### 4.1.3. *A survey of high-resolution satellite images available for contrails observation*

In the scope of the work on observation, the Climaviation project uses an external contractor to identify satellite products. The survey of satellite images suitable to observe contrails presence and evolution can be divided into two main sources. A first source are satellite data providers for research purposes. The second source are data providers for commercial applications.

Providers for research purposes take the form of open data hubs accessible through the Internet. A first list of 7 suitable providers has been established and each of them will be tested in term of content and ease of data extraction. A rapid exploration confirmed that data from satellites Landsat, Sentinel-2, CBERS and DAICHI are freely accessible with a decametric resolution and without a cloud decontamination selection. The DINAMIS program aims at providing metric-resolution images from satellites operated by Airbus Defence & Space (SPOT and Pléiades) for research applications at negotiated prices.

Some of the shortlisted data hubs are presented as DIAS (Data Integration and Analysis System). It means that images are available within a computing cloud platform. A DIAS have some advantages: it avoids downloading numerous large images and enables the coding of image processing algorithms conveniently through the cloud. However, some DIAS services are not free of charges and images catalogues may vary from a DIAS to another. DIAS solutions are specifically tailored for intensive computing on massive image datasets but can be convenient for research activities.

A next step will explore data for commercial applications. These are far from being available through centralized platforms. However, such tools as the Earth Observation portal maintained by ESA lists exhaustively the existing missions fulfilling the criteria of Climaviation project. Most of the companies proposing such a service will be directly contacted to have a clear and complete products definition, including the possibility to obtain images before cloud-clearing.

## 4.2. WP 4.2: Data acquisition

The objective of the package is to acquire data additional to that collected in package 4.1.

A new sky imager, reference SteadySun SW-05, has been installed at the SIRTA observatory since the 15th of March 2022 to allow a better monitoring of the sky (Figure 4-15). This sky imager is specifically dedicated to the Climaviation project, and we can configure the system on demand. The main advantages of this sky-imager are the temporal sampling, that we can fix to 1 second or better, and a maximum picture resolution of 2592×1944 pixels. The final setup and software configuration should be fixed at the end of April 2022.

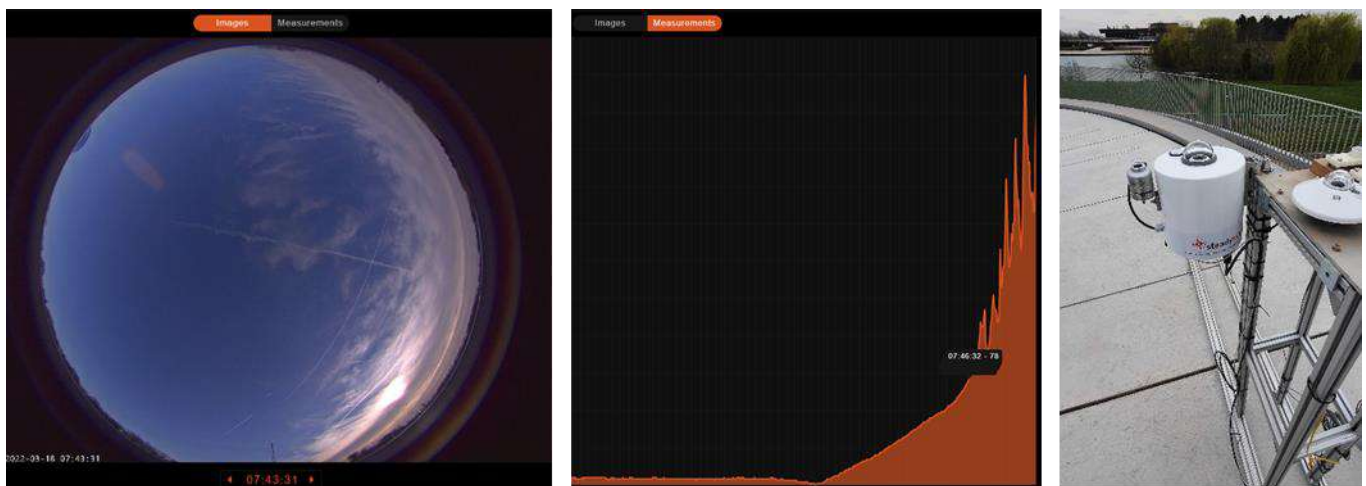


Figure 4-15: From left to right: sky image on 18 March 2022 at 07:43 UTC, time series of shortwave downwelling flux on the same day, and current setup of the new SteadySun SW-05 sky-imager at the SIRTA observatory.

## 4.3. WP 4.3: Model evaluation for contrail prediction

The objective of Work Package 4.3 is to use contrails, clouds, and atmospheric chemistry observations to evaluate models.

There has been no activity in this work package during the reporting period, as the contrail datasets described in section 4.1.2 are being built.

## 5. AXIS 5: CLIMATE IMPACTS OF AVIATION

The fifth axis of research aims to bring together the advances made in the modelling and evaluation of the various contributors to the radiative perturbation generated by aviation, to assess the resulting total impact on global warming.

### 5.1. WP 5.1: Traffic and emission scenarios

Contributors: Claire Sarrat (ONERA), Luis Basora (ONERA), Grégoire Dannel (IPSL), Olivier Boucher (IPSL), Philippe Novelli (ONERA)

The objective of work package 5.1 is to determine air traffic emissions and their spatio-temporal distribution on the globe, and to define plausible scenarios for the evolution of air transport.

#### 5.1.1. *Air traffic databases*

To elaborate a global and annual emissions aviation inventory it is necessary to identify the relevant data of air traffic. In fact, the actual difficulty for such an inventory is the amount of data to deal with to build an as much as possible exhaustive database, at the global and annual scales containing the geo-localisation of flight (latitude, longitude, altitude, date) especially for contrails formation, NO<sub>x</sub> and PM emissions as their impacts depend on location. This work has begun in 2021/2022 with the identification of the various databases. Their main characteristics and limitations in the Climaviation context are described below.

OAG is a global travel data provider for flight information including:

Airlines schedules at the global scale for the 20 last years,

- Flights status,
- Connection times,
- Historical flights data: 2004-present: carrier, flight number, flight departure time and flight arrival data, flight date, departure/destination airports
- Emissions data: 2019-present, global: Fuel burn by tons, flight, flight stage and seat, Carbon emissions by tons, flight, flight stage and seat

The OAG database provides data for scheduled flights but not actual flights nor trajectories (only city pairs). This database is not complete enough for our purpose and cannot be used alone as underlined by Quadros et al., 2022.

EUROCONTROL R&D data archive:

- available for 2015-2019: 4 month/year (March, June, September, and December).
- The data can be used to validate our ATM simulator for specific regions/periods.

Flightradar24:

- global flight tracking mainly based on terrestrial Automatic Dependent Surveillance-Broadcast (ADS-B). Data is not open access.

Flight Aware:

- provides ADS-B data from satellite and terrestrial network (from Aireon space-based data). This database is more complete but more expensive than Flightradar24.

Open sky

- Open Air Traffic Data for Research: open access terrestrial ADS-B data.

The databases made from ADS-B signals are good candidates for the reconstruction of air traffic scenarios but have to be used in conjunction with other data and an air traffic simulator. Therefore, the air traffic database will be build using a combination of databases for regional area (e.g., Europe first) and then will be completed by combining the OAG database (based on city pair data) and ADS-B data from Flightradar24 and/or OpenSky. A reduced model will be adapted from Seymour et al. (2020) (see Section 5.1.2) to compute large quantities of aircraft trajectories and coupled with the ATMLAB, the ONERA’s air traffic simulator for aircraft performance and emissions calculations.

IPSL purchased a FlightRadar24 flight database. To assess its accuracy, we performed a comparison with the OAG database for two particular days. The two databases differ in that FR24 is derived from ground-based monitoring of ADS-B signals while OAG is based on programmed flight schedules. It was found that a significant fraction (in order of 20%) of flights in the OAG database were not in the FR24 database and vice-versa. Another comparison between FR24 and an alternative database built from satellite monitoring of the ADS-B signals showed similar results, some aircraft signals were present in the FR24 database but not in the other and vice-versa.

Besides that, a comparison of the flights arriving and departing from the Parisian airports has been carried out for the month of December 2021. Three databases were used: the FlightRadar24 database, the Eurocontrol data available online that provides historical daily traffic from different airports and the raw data processed with the ADS-B antenna of the IPSL, located at Palaiseau (south of Paris). The comparison shows very similar results in terms of total numbers and day-to-day variations despite some differences on certain days for Charles-de-Gaulle airport. We speculate that the drop during the 3<sup>rd</sup> week for the ADS-B data could be attributed to planes approaching from the north of the airport which could be missed by the antenna.

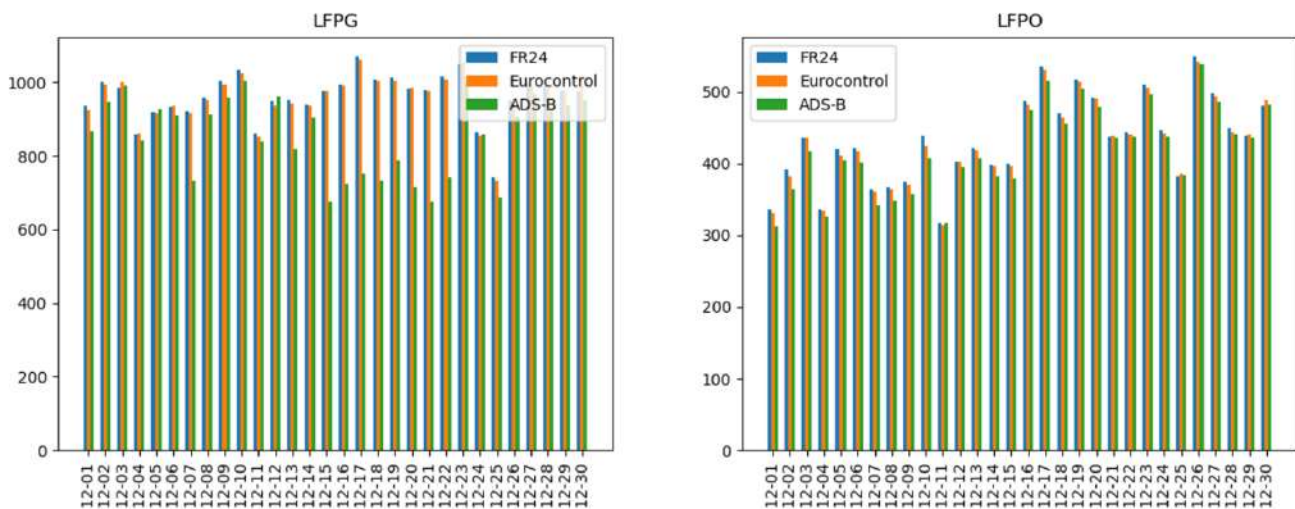


Figure 5-1: Comparison of the number of flights at the Parisian airports with different databases: FlightRadar24 (blue), Eurocontrol (orange) and the ADS-B antenna located at Palaiseau (green). On the left, Paris Charles de Gaulle and on the right, Paris Orly.

A preliminary conclusion is that the FlightRadar24 database greatly facilitates data exploitation since the data are already processed. The data received from the ADS-B contains the identity, position and speed of the aircraft but contains neither its origin nor its destination. The data bought from FR24 provides this information which eases the data processing. However, the data have been filtered during the process: some flights are missing, and we currently lack an estimate of the lack of completeness of the database.

Other data sources were tested. The free API of OpenSky which relies on ADS-B signal could provide a good coverage over Europe and North America. However, since it mainly relies on ground antenna, it does not provide any coverage over the ocean, as can be seen on Figure 5-2, with no planes detected above the Atlantic Ocean. To have the full trajectory of the plane, ADS-B tracking from the ground must be complemented using satellite data. The second difficulty in using a live API lies in the processing of the raw data received. Since the data broadcast by transponders only provides the position of the aircraft, flight departure and destination must be calculated. This is cumbersome but feasible by analysing flight paths, assuming sufficient coverage worldwide.

In conclusion, despite having analysed and compared several databases, it remains difficult to have a single complete database of all air traffic around the globe.

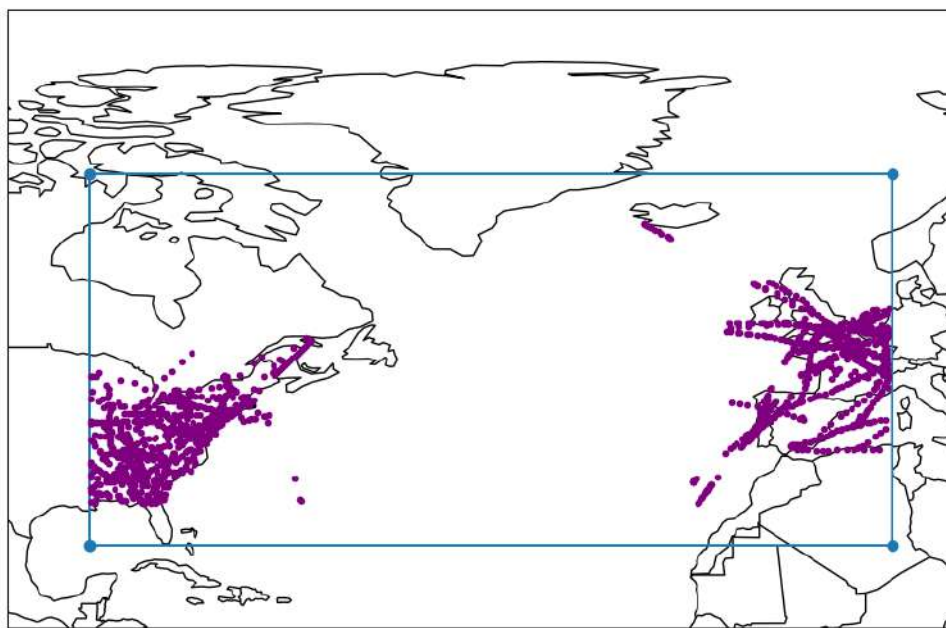


Figure 5-2: 100 aircraft tracked over the north Atlantic on 6 March 2022 with the OpenSky API.

### 5.1.2. *Modelling global fuel consumption of commercial aviation*

The goal of the activity is to develop a framework to estimate fuel consumption of commercial aviation at the global level to assess aircraft emissions (in particular CO<sub>2</sub> through the calculation of fuel consumption). The framework is based on the FEAT method (Fuel Estimation in Air Transportation, Seymour et al (2020)), which leverages a reduced model to compute the global fuel consumption of an entire year (millions of flights) in a few milliseconds. Figure 5-3 presents an overview of the FEAT methodology.

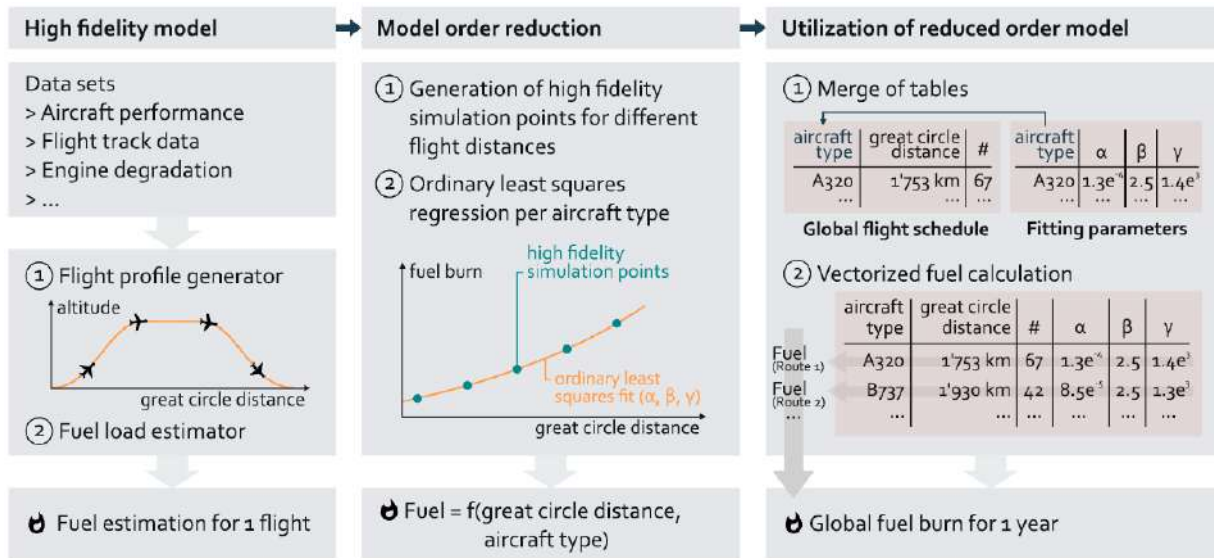


Figure 5-3: FEAT methodology overview. Taken from Seymour et al. (2020).

The original FEAT implementation uses EUROCONTROL BADA (Nuic et al (2010)) as the performance model for the high-fidelity model. We have started the implementation of the framework (using Github of L. Basora) with the objective of using either the OpenAP (Sun et al (2020)) performance model or ADS-B data from OpenSky (Schäfer et al (2014)) to build the flight profiles covering the operational range of each aircraft type. The idea is then to compute the fuel consumption for each flight profile with OpenAP as well. Thus, we will be able to use the resulting fuel consumption points versus the flight profile distances to fit a quadratic model to obtain a reduced model per aircraft type as proposed by FEAT. Finally, we should be able to estimate the global fuel consumption by using the reduced models along with the OAG dataset (OAG Aviation Worldwide) if available. The details of the necessary FEAT algorithms and datasets can be found in Seymour et al. (2020).

The work done so far is the development of the first stage of the FEAT methodology (high fidelity model - flight profile generator) by using OpenAP and integrating the possibility of generating the flight profiles from ADS-B data as an option. In addition, we started testing OpenAP to estimate the fuel flow as a first step necessary to fit the reduced models. There are some issues as the difficulty of getting some datasets (e.g., Planespotters) or enough ADS-B data from OpenSky to cover traffic areas outside European and US airspaces (ADS-B data are also used in the FEAT methodology to correct the great circle distances to take into account ATM inefficiencies).

The next step for fuel consumption estimation (and aircraft emissions) at the global scale will be to compare on a sub-domain (e.g., Europe and for few months) the FEAT methodology using the great circle distances approximation with actual ADS-B data (from Open Sky) or Eurocontrol database (e.g., Eurocontrol R&D Data Archive devoted to research). Moreover, based on these sub-domain estimations several performance models will be used to evaluate air traffic fuel consumption: BADA 3, BADA 4 and Open AP. These comparisons will enable to estimate the uncertainties and the precisions of the different methodologies.

## **5.2. WP 5.2: Integration of all non-CO<sub>2</sub> effects in the climate model**

The objective of work package 5.2 is to extend and improve the LMDZ global climate model by incorporating the parameterizations developed or improved by work packages 1 to 4.

Activities are currently taking place in other work packages. See report on Work Package 1.5 for the implementation of ISSRs in LMDZ, and Work Package 2.2 for work on atmospheric chemistry modelling in LMDZ INCA.

## **5.3. WP 5.3: Estimation of climate impacts**

Contributors : Grégoire Darnet (IPSL), Olivier Boucher (IPSL)

The objective of work package 5.3 is to estimate the CO<sub>2</sub> and non-CO<sub>2</sub> forcing from aviation and their past evolution, and to estimate the resulting climate change.

To estimate the CO<sub>2</sub> emissions of aviation, IPSL uses the FlightRadar24 database available for the years 2019 until 2022. A first computation of CO<sub>2</sub> emissions had been performed using a crude average emission factor of CO<sub>2</sub> per km flown from a previous study by the International Council on Clean Transportation (ICCT) (Graver et al, (2018)). However, it is important to note that the FR24 database contains not only commercial aircraft but also leisure aircraft (used by private individuals), helicopters, some military aircraft, and private jets. Thus, the mix of aircraft is different from that of the ICCT study, and the average emission factor may not be appropriate for our database. Furthermore, it may lead to important discrepancies at the regional level and for the split between domestic and international traffic. To compute the emissions more accurately, the FR24 database has been sorted and aircraft were categorized between commercial planes and business jets based on their technical characteristics.

The methodology from Seymour et al (2020) was used to compute the fuel consumption and subsequent CO<sub>2</sub> emissions. Their approach consists in calculating the consumption for a specific aircraft (ignoring engine changes) as a function of the distance travelled using the assumption of a great circle route between the origin and the destination airports and an additional scaling factor. Unfortunately, Seymour et al (2020) have modelled only about a hundred aircraft (the most used commercial aircrafts). We have complemented their database by grouping together known similar aircraft with similar equipment and for aircraft not included in the study, the average coefficients have been computed (depending on their category, commercial planes or business jets.) to calculate their consumption. As the FR24 database uses ADS-B signals, data for some flights do not contain any indication on the aircraft type. For these specific cases, the average coefficients of all aircraft in the study have been used. Finally, the reliability of the fuel estimation developed by Seymour et al (2020) will have to be studied to know if the model can be used for the rest of the project.

## **5.4. WP 5.4: Development of OSCAR-Aviation**

The objective of work package 5.4 is to develop a version of the OSCAR model adapted to the climate impact of aviation.

Activities in this work package start later in the project.

## **6. AXIS 6: OPTIMISATION STRATEGIES**

The sixth axis of research has the general objective of exploring strategies for minimizing the overall impact of aviation on the climate, considering not only CO<sub>2</sub> but also the other types of impact studied within the framework of the project.

### **6.1. WP 6.1: Assessment and relevance of climate change metrics for aviation**

The objective of this work package is to evaluate different climate metrics and their relevance to several objectives of reducing the climate impact of aviation.

Activities in this work package start later in the project.

### **6.2. WP 6.2: Climate impact of the fleet estimated by OSCAR**

Contributor: Olivier Boucher (IPSL)

The objective of work package 6.2 is to simulate the climate impact of aviation based on different scenarios of future fleet evolution.

The first paper published under the Climaviation umbrella, Boucher et al. (2021), used the OSCAR compact Earth System model and historical CO<sub>2</sub> emissions data to calculate the fraction of CO<sub>2</sub> radiative forcing that can be attributed to the aviation sector. Estimating this fraction is not trivial because CO<sub>2</sub> radiative forcing depends logarithmically on the change in atmospheric concentration and the efficacy of natural sinks of CO<sub>2</sub> changes over time. A popular method, used for example by Lee et al. (2021), is the residual attribution method, whereby the radiative forcing for a particular sector (the aviation sector in this case) is calculated as the difference between the total CO<sub>2</sub> radiative forcing and the CO<sub>2</sub> radiative forcing had that particular sector not existed. However, this method suffers from the major drawback that total radiative forcing from all sectors considered together is not the same as the sum of the radiative forcings from each sector considered individually. Furthermore, aviation started only a few decades ago, so its emissions contribute relatively more to the change in CO<sub>2</sub> concentrations than other sectors, but relatively less to the CO<sub>2</sub> radiative forcing because of its logarithmic dependence.

To address those issues, Boucher et al. (2021) used the proportional, differential, and time-sliced attribution methods. Using OSCAR allows them to account for how CO<sub>2</sub> concentration decreases as natural sinks sequester the emitted CO<sub>2</sub> over time. The more rigorous methods (the proportional, differential, time-sliced methods) lead to an aviation CO<sub>2</sub> radiative forcing that 20%, 13%, and 12% larger than the residual method, which underestimates the true CO<sub>2</sub> radiative forcing by aviation. However, this is compensated by the lower contribution to the increase in CO<sub>2</sub> atmospheric concentration that we estimated using our well calibrated model. Boucher et al. (2021) estimate that aviation contributed 2.2 ppm to the rise in CO<sub>2</sub> atmospheric concentration in 2018, which is less than the values of 2.9, 2.4 and 2.4 ppm used by Lee et al. (2021) to derive their best estimate of aviation CO<sub>2</sub> radiative forcing.

### **6.3. WP 6.3: Quality and relevance of numerical weather prediction for contrail forecasting**

Contributors: Kevin Wolf (postdoctoral researcher, IPSL), Stefan Markovic (Masters intern, IPSL)

The objective of this work package is to quantify the quality of forecasts of water vapor and regions supersaturated with respect to ice.

Stefan Markovic (a student at Météo-France) has started an internship on 21 March 2022 to examine the quality of ECMWF weather forecasts of ISSR compared to ERA5 and radiosondes. His work will be reported in the 2023 annual report.

#### **6.4. WP 6.4: Study of optimisation strategies**

Contributors: Olivier Boucher (IPSL), Claire Sarrat (ONERA), Thomas Chaboud (ONERA)

The objective of the work package is to reflect on the different solutions that could reduce the overall climate impact of aviation, considering the specificity of the different contributors. The conditions for minimizing their impact are not the same for each of these contributors, so compromises must be made.

##### **6.4.1. *Aircraft trajectories optimisation***

In 2021/2022, we have done preliminary work on the topic of optimisation strategies. We eventually aim to present a proof-of-concept of whether and how a flight route can be optimised to minimise its total climate impact under different metrics. As a first step, we wanted to check to which extent a simple optimisation of the flight time for a constant aircraft speed matches the actual route followed by the airline. Here flight time is used as a proxy for fuel consumption and therefore CO<sub>2</sub> emissions as in Wells et al (2021). For this we extract all transatlantic flights in the IAGOS database for years 2019-2021 and identify their counterparts in the FlightRadar24 database. The North Atlantic Flight Corridor is used as a case study because the flights are sufficiently long to get an impact from rerouting and, unlike busy continental regions such as North America and Europe, this region may provide more flexibility in terms of rerouting. For each flight, we extract the beginning and end of the cruising phase in the FR24 database and see how well we can reconstruct the actual trajectory that is provided in IAGOS using these two datapoints and the wind field. Only two IAGOS-equipped planes from Lufthansa fly regularly in the North Atlantic Flight Corridor. These planes fly at a pressure close to 200 hPa, therefore we use only the 200 hPa wind field from ERA5 to optimise the flight route. We assume a constant aircraft speed (relative to the air) and seek to minimize the flight time. We separate eastbound and westbound flights and focus on the years 2018 to 2021.

Figure 6-1 shows on a few examples that we can capture reasonably well the actual trajectories by minimising flight time based on the wind field at 200 hPa. We further show on Figure 6-2 that, for a larger sample of IAGOS flights, the reconstructed IAGOS flight times are generally within 1% of the optimal flight time for our simple metric. This is likely to be within uncertainties of our simple optimisation procedure and various operational constraints not accounted for in the minimisation procedure. Thus, we can consider that such flights are optimal. We find however that for a small number of flights, the reconstructed IAGOS flight time is longer by 1.5 to 4% than the optimal flight time. It is unclear whether these flights were not properly optimized or were subject to other constraints (avoiding a storm, overcrowded optimal flight tracks, ...). At first sight, our preliminary results are consistent with those of Wells et al. (2021) who concluded that “when taking a weighted average across the North Atlantic tracks according to their relative occupation statistics, the average eastbound (JFK=>LHR) flight was 2.5% longer than optimal, and the average westbound (LHR=>JFK) flight was 1.7% longer”.

The next step in our investigation consists in looking at the occurrences of ISSR on such NAFC trajectories. Figure 6-3 shows that the ISSR detected by the IAGOS instrument package corresponds, at least qualitatively, to regions of large RHI in ERA5. Here the ERA5 is not yet interpolated to the flight time so there is a small mismatch in time with the IAGOS sampling, which may explain some of the shift in patterns. ISSR regions can present different patterns. On the left panels, the ISSR are “rivers” that any eastbound or westbound flight

will have to cross. On the right panels, the ISSR are small or larger patches that could be avoided by rerouting. Work will continue to analyse these features in a more quantitative way.

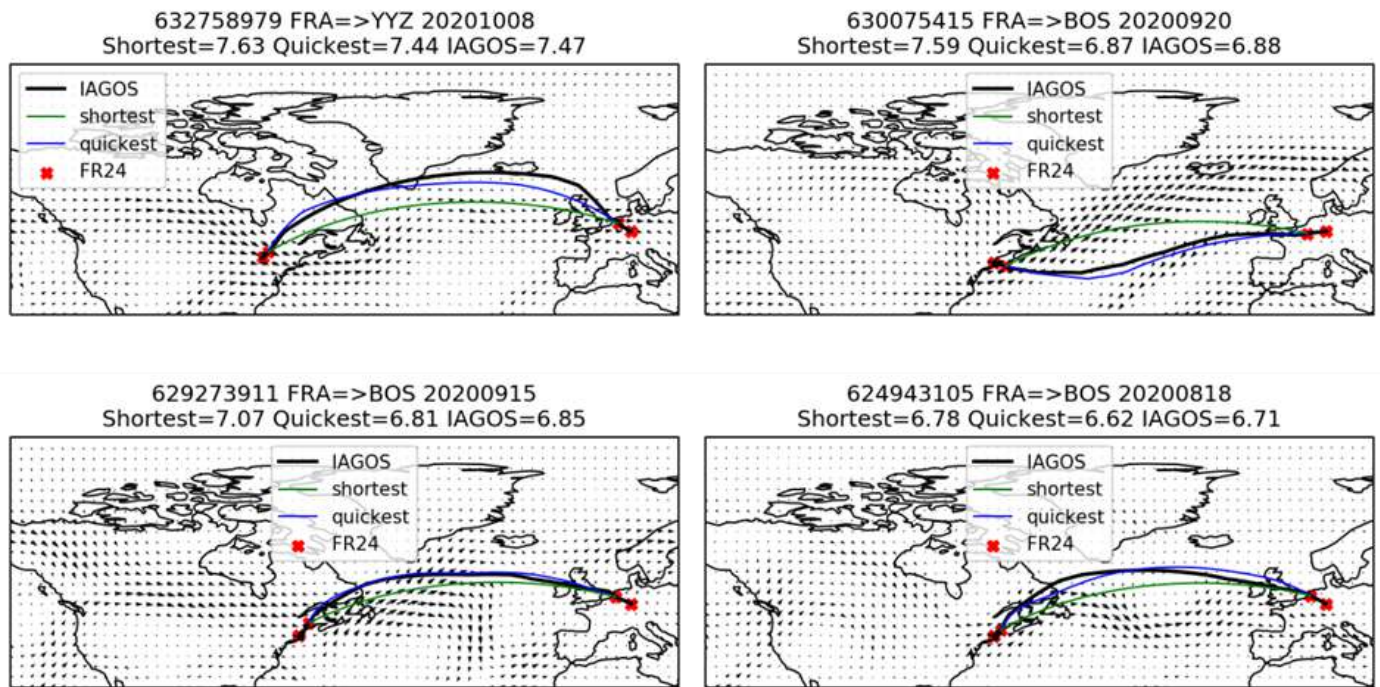


Figure 6-1: Examples of westbound Europe-US flight trajectories. The green curve represents the shortest distance (great circle) between the start and end of the cruising period (as identified in the FR24 database). The blue curve represents a simple estimate of the optimal flight minimising flight time based on the ERA5 wind field at 200 hPa. The black curve represents the actual trajectory by the IAGOS flight.

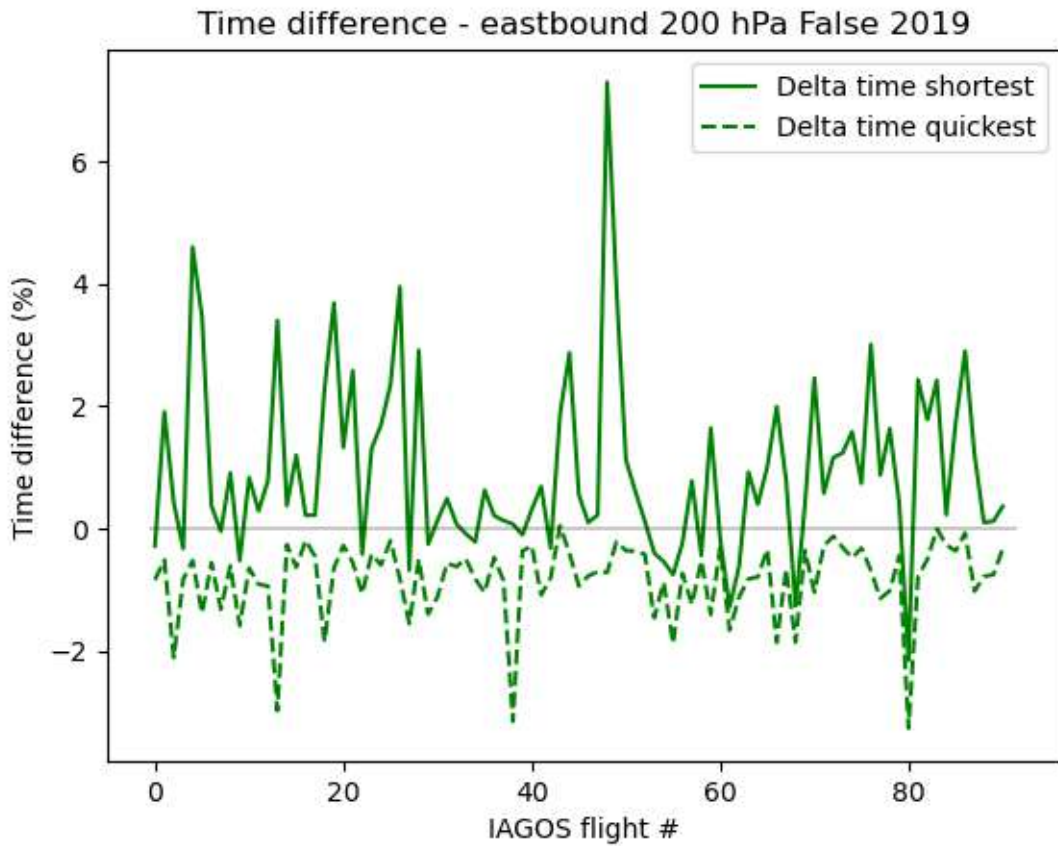


Figure 6-2: Relative difference in flight time between the great circle (i.e., shortest) or the optimised (i.e., quickest) trajectories and the actual IAGOS trajectories for eastbound flights in the year 2019. Here the IAGOS flight time is not the actual flight time, but the flight time recomputed as in our minimisation procedure. Therefore, by construction the reconstructed IAGOS flight time is always longer than the optimised flight time.

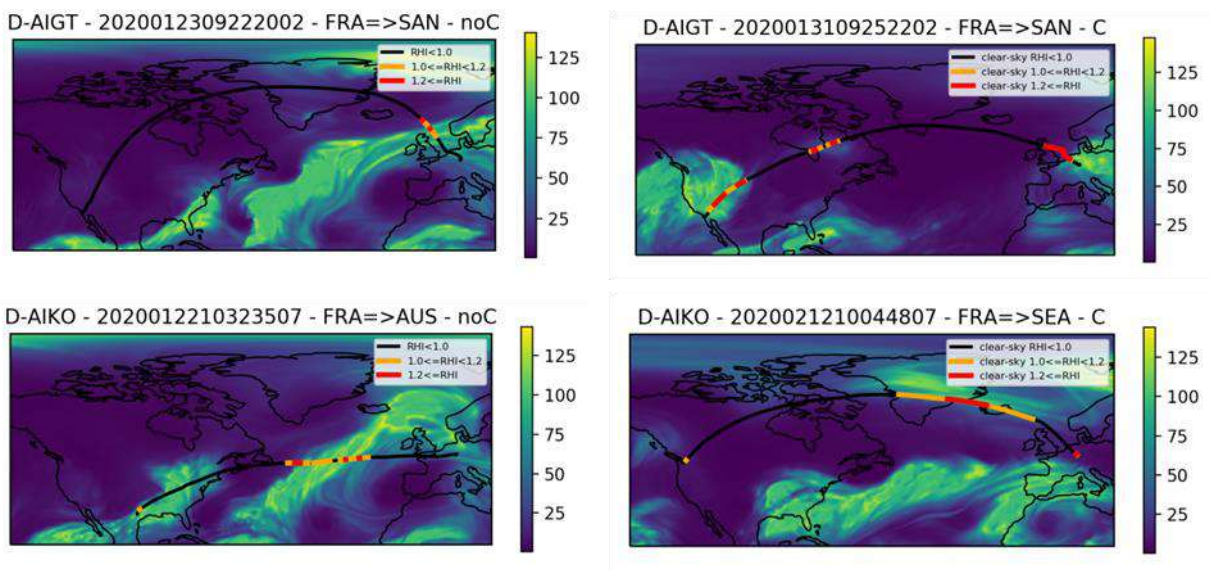


Figure 6-3: IAGOS trajectories (in black) for selected flights with mild and severe ISSR shown in orange and red colour. The large-scale pattern in relative humidity over ice (RHI) from ERA5 is shown in the background.

#### 6.4.2. *Logistics improvement: methodology and feasibility*

We often consider two main paths for reducing the aviation impact on climate: technology improvements (through combustion/propulsion, aerodynamics, etc..) and aircraft trajectories in Air Traffic Management (ATM). A third path is maybe understudied with very little consideration in the literature and consists in optimising the logistical aspects of air transport. Indeed, from a societal point of view, the value of aviation resides primarily in the service it provides, namely, the transportation of people and goods. Apart from the improvements hoped for in terms of aircraft technology and traffic management, and practically independent of them, there is obviously an organizational (or “logistical”) waste in the way this service is currently rendered, regarding its environmental impact.

Current constraints on the industry (kerosene taxes, environmental regulations...) are relatively light and in part self-imposed due to financial and public relations concerns, but this picture is probably bound to change rapidly along with the increased perception of global climate change and a re-evaluation of energy usage priorities. Evaluating how much of aviation’s impact could be reduced while still providing the same transport service is an important task, were it only to help stakeholders decide whether the potential gain would be worth the efforts invested in organizational improvements, if and when they are faced with cost-incentive regulations, environmental taxes or more stringent measures.

Three main branches of logistical improvement we can readily envision and will discuss below are

- the load factor, or capacity utilisation of each aircraft.
- fitting the aircraft used for each mission as best as possible.
- optimising each aircraft’s usage: choosing a cruise speed and altitude best suited to each mission.

To compare alternative solutions, a homogeneous criterion (“Impact Score” IS) expressing the environmental impact relative to each unit of service (e.g., in GWP\* per passenger per kilometre) must be devised. Then, a number of individual aircraft simulations will fill 4D tables, one for each aircraft type, giving the IS as a function of

- mission length.
- cruise speed.
- cruise flight level.
- number of passengers.

These tables will be large but will enable fast look-up of score values. Besides the need for care with performance and discretisation granularity, difficulties will include precise modelling of operational take-off weights, both minimizing the fuel embarked with regard to the payload and still respecting the safety fuel reserves.

The OAG 2018 database will provide a realistic quantification of passenger flows to be guaranteed with their geographical and precise temporal distribution on a global, yearly scale. The next phase will be to set a movement planning that will minimize the overall sum of IS: ideally, one wants to assign as much as possible the most favourable type of aircraft, used with economical payloads, cruise speed and altitude, so that

- the passenger demand is satisfied.
- the logistical constraints (availability of an aircraft type in the time and place needed) are respected.
- the service quality (movement frequencies, flight time) is as little degraded as possible.

In keeping with the feasibility approach of this work, sub-problems (e.g., on a regional and monthly scale) could be addressed before attempting larger or full-scale resolutions. Partial validation of the solutions devised can be obtained through large-scale traffic simulations.

Possible objections pertaining to the feasibility of the implementation of these improvements are entirely legitimate, especially considering some of them would imply an overhaul of business models in the sector: right now, each carrier owns its fleet, which is chosen on grounds of performances but also of staff qualification and economy of maintenance. Using the most environmentally friendly aircraft at their best capacity on each mission, as much as possible, would probably require that leasing becomes the common practice - or even a separation of the ticket-selling and aircraft operating businesses.

Even improving the load factors may seem daunting; as of 2017, ICAO noted a global average of only 81% while still including the large and growing share of the low-cost carriers (LCC) – the most efficient of which (RyanAir) reached no less than 94.7% that year. Gains of 10% or more are certainly possible using the LCC's dynamic pricing methods, generalising code-sharing, etc. - but at what cost, in terms of service quality (e.g., frequencies)? This study's results could help answer such questions. Again, it is intended to evaluate the amount of organisational “waste”, relative to a given service provided by the air transport, rather than to describe fully implementable solutions at a 30-year horizon.

During the first year of the project, this work was devoted to the data acquisition, the analyses of the aircraft performance models (OpenAP, BADA 3, BADA 4) and their implementation in the ONERA's air traffic simulator (ATMLab). A methodology is being established to conduct such a study, in particular for the definition of the IS based on kerosene consumption and related pollutants emissions.

## REFERENCES

- Abdul-Razzak, H., Ghan, S. J., and Rivera-Carpio, C.: A parameterization of aerosol activation. 1. Single aerosol type, *J. Geophys. Res.*, 103, 6123–6131. <https://doi.org/10.1029/97JD03735>, 1998.
- Abdul-Razzak, H. and Ghan, S. J.: A parameterization of aerosol activation. 2. Multiple aerosol types, *J. Geophys. Res.*, 105, 6837–6844. <https://doi.org/10.1029/1999JD901161>, 2000.
- Abel, S. J. and Shipway, B. J., A comparison of cloud resolving model simulations of trade wind cumulus with aircraft observations taken during RICO. *Q.J.R Meteorol. Soc.*, 133: 781-794, <https://doi.org/10.1002/qj.55>, 2007.
- Anderson G. P., S.A. Clough, F.X. Kneizys, J.H. Chetwynd, E.P. Shettle, AFGL atmospheric constituent profiles (0-120 km), Technical Report ADA175173, AFGL-TR-86-0110, Environmental research papers N°954, Project 7670, Optical Physics Division, Air Force Geophysics Laboratory, Hanscom Air Force Base, MA 01731. <https://apps.dtic.mil/sti/pdfs/ADA175173.pdf>, 1986.
- Auerswald T., J. Bange, A New Method to Generate Anisotropic Synthetic Turbulence for LES, In: R. Radespiel, R. Niehuis, N. Kroll, K. Behrends, *Advances in Simulation of Wing and Nacelle Stall*, Notes on Numerical Fluid Mechanics and Multidisciplinary Design, 131, Springer, [https://doi.org/10.1007/978-3-319-21127-5\\_13](https://doi.org/10.1007/978-3-319-21127-5_13), 2016.
- Baran A. J., Hill P., Walters D., Hardiman S. C., Furtado K., Field P. R., Manners J., The impact of two coupled cirrus microphysics–radiation parameterizations on the temperature and specific humidity biases in the tropical tropopause layer in a climate model, *Journal of Climate*, 29 (14), 5299-5316, <https://doi.org/10.1175/JCLI-D-15-0821.1>, 2016.
- Bellisario Ch., C. Malherbe, C. Schweitzer, K. Stein, Development of an atmospheric infrared radiation model with high clouds for target detection, *Proceedings SPIE Conference*, Vol. 9997. <https://doi.org/10.1117/12.2241806>, 2016.
- Berk A., P. Conforti, R. Kennett, T. Perkins, F. Hawes, J. van den Bosch, MODTRAN 6: a major upgrade of the MODTRAN radiative transfer code, *Proceedings SPIE Conference*, Vol. 9088, *Algorithms and Technologies for Multispectral, Hyperspectral and Ultraspectral Imagery XX*, 90880H, <https://doi.org/10.1117/12.2050433>, 2014.
- Bigg, E. K.: The formation of atmospheric ice crystals by the freezing of droplets, *Q. J. Roy. Meteorol. Soc.*, 39, 510–519, <https://doi.org/10.1002/qj.49707934207>, 1953.
- Borella, A., Modélisation de la sursaturation de l'eau par rapport à la glace en haute altitude dans le modèle de circulation générale LMDZ, rapport de stage de M1, Ecole Normale Supérieure, septembre 2021.
- Boucher, O., A. Borella, T. Gasser, D. Hauglustaine, On the contribution of global aviation to the CO<sub>2</sub> radiative forcing of climate, *Atmos. Environ.*, 267, 118762, <https://doi.org/10.1016/j.atmosenv.2021.118762>, 2021.
- Brown, N., Weiland, M., Hill, A., Shipway, B., Maynard, C., Allen, T., & Rezny, M. A highly scalable Met Office NERC Cloud model. arXiv preprint arXiv:2009.12849. <https://doi.org/10.48550/arXiv.2009.12849>, 2020.

- Brunet, S., F. Garnier and L. Jacquin, Numerical/experimental simulation of exhaust jet mixing in wake vortex, AIAA 30th Fluid Dynamics Conference. <https://doi.org/10.2514/6.1999-3418>, 1999.
- Burkhardt U., B. Kärcher, Global radiative forcing from contrail cirrus, *Nature Climate Change*, 1, 54-58, <https://doi.org/10.1038/NCLIMATE1068>, 2011.
- Chmielarski V., Simulation de l'interaction jet/tourbillon dans le sillage d'un avion et son impact sur la formation des traînées de condensation en utilisant l'approche RANS et l'approche hybride RANS/LES, *Mécanique des fluides*, Université Paris-Saclay, <https://tel.archives-ouvertes.fr/tel-03433381>, 2021.
- Crow S.C., Stability Theory for a Pair of Trailing Vortices, *AIAA Journal*, 8, N°12, 2172-2179. <https://doi.org/10.2514/3.6083>, 1970.
- Crow, S. C. and E. R. Bate, Lifespan of trailing vortices in a turbulent atmosphere, *Journal of Aircraft*, 13(7):476–482. <https://doi.org/10.2514/3.44537>, 1976.
- Cariolle, D., Caro, D., Paoli, R., Hauglustaine, D.A., Cuénot, B., Cozic, A., Paugam, R. Parameterization of plume chemistry into large-scale atmospheric models: Application to aircraft NO<sub>x</sub> emissions. *J. Geophys. Res.* 114, D19302. <https://doi.org/10.1029/2009JD011873>, 2009.
- Carleton A.M., D.J. Travis, K. Master, S. Vezhapparambu, Composite Atmospheric Environments of Jet Contrail Outbreaks for the United States, *J. App. Meteo. and Clim.*, 47, 641- 667. <https://doi.org/10.1175/2007JAMC1481.1>, 2008.
- Chevalier H., Flight test studies of the formation and dissipation of trailing vortices, *J. Aircraft*, 10, 1, <https://doi.org/10.2514/3.60193>, 1973.
- Courtier P., C. Freydier, J.-F. Geleyn, F. Rabier, M. Rochas, The ARPEGE project at Météo-France, *Proceedings of 1991, ECMWG Seminar on Numerical methods in Atmospheric Models*, ECMWF, Reading, 193-231. <https://www.ecmwf.int/node/8798>, 1991.
- Czech, M., G. Miller, J. Crouch, and M. Strelets, 2005: Predicting the near-field evolution of airplane trailing vortices. *C. R. Phys.*, 6, 451–466. <https://doi.org/10.1016/j.crhy.2005.07.008>, 2005.
- DeMott, P. J., Prenni, A. J., Liu, X., Kreidenweis, S. M., Petters, M. D., Twohy, C. H., Richardson, M. S., Eidhammer, T., and Rogers, D. C.: Predicting global atmospheric ice nuclei distributions and their impacts on climate, *P. Natl. Acad. Sci. USA*, 107, 11217–11222, <https://doi.org/10.1073/pnas.0910818107>, 2010.
- DeMott, P. J., Prenni, A. J., McMeeking, G. R., Sullivan, R. C., Petters, M. D., Tobo, Y., ... & Kreidenweis, S. M. Integrating laboratory and field data to quantify the immersion freezing ice nucleation activity of mineral dust particles. *Atmospheric Chemistry and Physics*, 15(1), 393-409. <https://doi.org/10.5194/acp-15-393-2015>, 2015.
- Diao, M., Jensen, J. B., Pan, L. L., Homeyer, C. R., Honomichl, S., Bresch, J. F., and Bansemer, A.: Distributions of ice supersaturation and ice crystals from airborne observations in relation to upper tropospheric dynamical boundaries, *J. Geophys. Res. Atmos.*, 120, 5101–5121, <https://doi.org/10.1002/2015JD023139>, 2015

- Duda D. and P. Minnis, Basic Diagnosis and Prediction of Persistent Contrail Occurrence Using High-Resolution Numerical Weather Analyses/ Forecasts and Logistics Regression. Part I: Effects of Random Error, *J. Appl. Met and Clim.*, 48, 1780-1789. <https://doi.org/10.1175/2009JAMC2057.1>, 2009.
- Emde C., Buras-Schnell R., Kylling A., Mayer B., Gasteiger J., Hamann U., Kylling J., Richter B., Pause C., Dowling T., Bugliaro L., The libRadtran software package for radiative transfer calculations (version 2.0.1), *Geosci. Model Dev.*, 9, 1647–1672, <https://doi.org/10.5194/gmd-9-1647-2016>, 2016.
- Eswaran V. and S.B. Pope, An examination of forcing in direct numerical simulations of turbulence, *Computers & Fluids*, Vol. 16, No. 3, pp. 257-278, [https://doi.org/10.1016/0045-7930\(88\)90013-8](https://doi.org/10.1016/0045-7930(88)90013-8), 1988.
- Final report of the TC2 Project, Projet Trainées de Condensation et Climat, TC2, Rapport final, Convention DGAC n°2011-02, 2015.
- Garnier F., S. Brunet, L. Jacquin, Modelling exhaust plume mixing in the near field of an aircraft, *Ann. Geophysicae*, 15, 1468-1477, <https://doi.org/10.1007/s00585-997-1468-1>, 1997.
- Gerz, T., T. Ehret, Wingtip Vortices and Exhaust Jets During the Jet Regime of Aircraft Wakes, *Aerosp. Sci. Technol.*, 7, 463–474. [https://doi.org/10.1016/S1270-9638\(97\)90008-0](https://doi.org/10.1016/S1270-9638(97)90008-0), 1997.
- Gerz, T., Dürbeck, T., and Konopka, P. Transport and effective diffusion of aircraft emissions. *Journal of Geophysical Research*, 103(D20):25905–25913. <https://doi.org/10.1029/98JD02282>, 1988.
- Gettelman, A., and C. Chen. The climate impact of aviation aerosols. *Geophys. Res. Lett.*, 40, pp. 2785-2789, 10.1002/grl.50520. <https://doi.org/10.1002/grl.50520>, 2013.
- Ghedhaïfi W., A. Bienner, R. Megherbi, E. Montreuil, E. Terrenoire, X. Vancassel and A. Loseille, Influence of atmospheric conditions on contrail formation: 3D simulation versus Schmidt-Appleman criterion, 24th ISABE (International Society of Airbreathing Engines) Conference, Canberra, Australie, September 2019.
- Gierens K.M.: Numerical simulations of persistent contrail, *J. Atmos. Sci.*, 53, 3333-3348, [https://doi.org/10.1175/1520-0469\(1996\)053<3333:NSOPC>2.0.CO;2](https://doi.org/10.1175/1520-0469(1996)053<3333:NSOPC>2.0.CO;2), 1996.
- Gierens K., E. Jensen, A numerical study of the contrail-to-cirrus transition, *Geo. Rea. Let.*, 25, n°23, 4341-4344; <https://doi.org/10.1029/1998GL900151>, 1998.
- Github of L. Basora. <https://github.com/lbasora/FEAT>
- Goff, J. A., Low-pressure properties of water-from 160 to 212° F, *Trans. Am. Heat. Vent. Eng.*, 52:95–121, 1946.
- Graver B, K. Zhang, D. Rutherford, CO<sub>2</sub> emissions from commercial aviation. International Council on Clean Transportation, ICCT. [https://theicct.org/wp-content/uploads/2021/06/ICCT\\_CO2-commercl-aviation-2018\\_20190918.pdf](https://theicct.org/wp-content/uploads/2021/06/ICCT_CO2-commercl-aviation-2018_20190918.pdf), 2018
- Haywood J.M., R.P. Allan, J. Bornemann, P.M. Forster, P.N. Francis, S. Milton, G. Rädcl, A. Rap, K.P. Shine, R. Thorpe, A case study of the radiative forcing of persistent contrails evolving into contrail-induced cirrus, *J. Geophys. R.*, 114, D24201, 17p.. <https://doi.org/10.1029/2009JD012650>, 2009.

Hill, A. A., Field, P. R., Furtado, K., Korolev, A. and Shipway, B. J., Mixed-phase clouds in a turbulent environment. Part 1: Large-eddy simulation experiments. *Q.J.R. Meteorol. Soc.*, 140: 855–869. <https://doi.org/10.1002/qj.2177>, 2014.

Hill, A., Brown, N., & Shipway, B. (2018). Met Office/NERC Cloud Model (MONC): User Documentation. Technical Report, Met Office, UK.

Hogan R. J., A. Bozzo, A flexible and efficient radiation scheme for the ECMWF model. *J. Adv. Modeling Earth Syst.*, 10, 1990-2008, <https://doi.org/10.1029/2018MS001364>, 2018.

Hourdin, F., Mauritsen, T., Gettelman, A., Golaz, J., Balaji, V., Duan, Q., Folini, D., Ji, D., Klocke, D., Qian, Y., Rauser, F., Rio, C., Tomassini, L., Watanabe, M., & Williamson, D. The Art and Science of Climate Model Tuning, *Bulletin of the American Meteorological Society*, 98(3), 589-602. <https://doi.org/10.1175/BAMS-D-15-00135.1>, 2017.

Hourdin, F., Rio, C., Grandpeix, J.-Y., Madeleine, J.-B., Cheruy, F., Rochetin, N., et al. LMDZ6A: The atmospheric component of the IPSL climate model with improved and better tuned physics. *Journal of Advances in Modeling Earth Systems*, 12, e2019MS001892. <https://doi.org/10.1029/2019MS001892>, 2020.

Jacquin, L. and F. Garnier, On the dynamics of engine jets behind a transport aircraft, ONERA-Publications-TP, 1996.

Jacquin, L. and C. Pantano, On the persistence of trailing vortices. *Journal of Fluid Mechanics*, 471:159–168. <https://doi.org/10.1017/S0022112002002161>, 2002.

Jacquin L, P. Molton, P. Loiret and E. Coustols, An Experiment on Jet-Wake Vortex Interaction, 37th AIAA Fluid Dynamics Conference and Exhibit. <https://doi.org/10.2514/6.2007-4363>, 2007.

Jensen E. J., O. B. Toon, D.L. Westphal, S. Kinne and A.J. Heymsfield. Microphysical modeling of cirrus, 1, Comparison with 1986 FIRE IFO measurements. *J. Geophys. Res.*, 99, 10421-10442, <https://doi.org/10.1029/93JD02334>, 1994.

Jensen E.J., A.S Ackerman, D.E. Stevens, O.B. Toon, P. Minnis, Spreading and growth of contrails in a sheared environment, *J. Geo. Res.*, 103, 31557-315997, <https://doi.org/10.1029/98JD02594>, 1998.

Johnson, H. G., V. Brion, and L. Jacquin, Crow instability: nonlinear response to the linear optimal perturbation, *Journal of Fluid Mechanics*, 795:652–670. <https://doi.org/10.1017/jfm.2016.176>, 2016.

Kärcher B., Formation and radiative forcing of contrail cirrus, *Nature Communications*, 9, 17p., <https://doi.org/10.1038/s41467-018-04068-0>, 2018.

Khou J. C., Modélisation des traînées de condensation par interaction entre l'aérodynamique, la cinétique chimique et la microphysique, *Mécanique des fluides*, Université Pierre et Marie Curie - Paris VI, <https://tel.archives-ouvertes.fr/tel-01403100>, 2016.

Krämer, M., Rolf, C., Spelten, N., Afchine, A., Fahey, D., Jensen, E., Khaykin, S., Kuhn, T., Lawson, P., Lykov, A., Pan, L. L., Riese, M., Rollins, A., Stroh, F., Thornberry, T., Wolf, V., Woods, S., Spichtinger, P., Quaas, J., and Sourdeval, O.: A microphysics guide to cirrus – Part 2: Climatologies of clouds and humidity from observations, *Atmos. Chem. Phys.*, 20, 12569–12608, <https://doi.org/10.5194/acp-20-12569-2020>, 2020.

Kristiansen, N. I., A. Stohl, and G. Wotawa, Atmospheric removal times of the aerosol-bound radionuclides <sup>137</sup>Cs and <sup>131</sup>I measured after the Fukushima Dai-ichi nuclear accident - a constraint for air quality and climate models. *Atmos. Chem. Phys.* 12, 10759-10769. <https://doi.org/10.5194/acp-12-10759-2012>, 2012.

Labarre L., K. Caillault, S. Fauqueux, C. Malherbe, A. Roblin, B. Rosier, P. Simoneau, C. Schweitzer, K. Stein, N. Wendelstein, MATISSE-V2.0: new functionalities and comparison with MODIS satellite images, *Proceedings SPIE Conference*, Vol. 8014. <https://doi.org/10.1117/12.886902>, 2011.

Lac C., J.-P. Chaboureau, V. Masson, J.-P. Pinty, P. Tulet, J. Escobar, M. Leriche, C. Barthe, B. Aouizerats, C. Augros, P. Aumond, F. Auguste, P. Bechtold, S. Berthet, S. Bielli, F. Bosseur, O. Caumont, J.-M. Cohard, J. Colin, F. Couvreur, J. Cuxart, G. Delautier, T. Dauhut, V. Ducrocq, J.-B. Filippi, D. Gazen, O. Geoffroy, F. Gheusi, R. Honnert, J.-P. Lafore, C. Lebeaupin Brossier, Q. Libois, T. Luinet, C. Mari, T. Maric, P. Mascart, M. Moge, G. Molinie, O. Nuissier, F. Pantillon, P. Peyrille, J. Pergaud, E. Perraud, J. Pianezze, J.-M. Redelsperger, D. Ricard, E. Richard, S. Riette, Q. Rodier, R. Schoetter, L. Seyfried, J. Stein, K. Suhre, M. Taufour, O. Thouron, S. Turner, A. Verrelle, B. Vie, F. Visentin, V. Vionnet, P. Wautelet, Overview of the Meso-NH model version 5.4 and its application, *Geosci. Model Dev.*, 11, 1929-1969. <https://doi.org/10.5194/gmd-11-1929-2018>, 2018.

Lafore J. P., J. Stein, N. Asencio, P. Bougeault, V. Ducrocq, J. Duron, C. Fischer, P. Hérelil, P. Mascart, V. Masson, J.-P. Pinty, J.-M. Redelsperger, E. Richard, J. Vilà-Guerau de Arellano, The Meso-NH Atmospheric Simulation System. Part I: adiabatic formulation and control simulation, *Annales Geophysicae*, European Geosciences Union, 16, 90-109. <https://doi.org/10.1007/s00585-997-0090-6>, 1998.

Le Dizès, S. and L. Laporte, Theoretical predictions for the elliptical instability in a two-vortex flow, *Journal of Fluid Mechanics*, 471:169–201. <https://doi.org/10.1017/S0022112002002185>, 2002.

Lee, D.S., D.W. Fahey, A. Skowron, M.R. Allen, U. Burkhardt, Q. Chen, S.J. Doherty, S. Freeman, P.M. Forster, J. Fuglestvedt, A. Gettelman, R.R. De León, L.L. Lim, M.T. Lund, R.J. Millar, B. Owen, J.E. Penner, G. Pitari, M.J. Prather, R. Sausen, L.J. Wilcox, The contribution of global aviation to anthropogenic climate forcing for 2000 to 2018, *Atmos. Environ.*, 244, 117834, <https://doi.org/10.1016/j.atmosenv.2020.117834>, 2021.

Lewellen D.C. and W. S. Lewellen, Large-eddy simulations of the vortex-pair breakup in aircraft wakes. *AIAA J.*, 34, 2337–2345. <https://doi.org/10.2514/3.13399>, 1996.

Lewellen D.C. and W.S. Lewellen, The effects of aircraft wake dynamics on contrail development. *J. Atmos. Sci.*, 58, 390–406. [https://doi.org/10.1175/1520-0469\(2001\)058<0390:TEOAWD>2.0.CO;2](https://doi.org/10.1175/1520-0469(2001)058<0390:TEOAWD>2.0.CO;2), 2001.

Lewellen D.C., O. Meza and W.W. Huebsch, Persistent contrails and contrail cirrus. Part I: Large-Eddy Simulations from Inception to Demise. *J. Atmos. Sci.*, 71, 4399–4419, <https://doi.org/10.1175/JAS-D-13-0316.1>, 2014.

Lewellen D.C., Persistent contrails and contrail cirrus. Part II: Persistent Contrails and Contrail Cirrus. Part II: Full Lifetime Behavior. *J. Atmos. Sci.*, 71, 4420-4438. <https://doi.org/10.1175/JAS-D-13-0317.1>, 2014.

Lewellen D.C., A large-eddy simulation study of contrail ice number formation, *J. Atmos. Sci.*, 77, 2585-2604. <https://doi.org/10.1175/JAS-D-19-0322.1>, 2020.

Lothon, M., Barnéoud, P., Gabella, O., Lohou, F., Derrien, S., Rondi, S., Chiriaco, M., Bastin, S., Dupont, J.-C., Haeffelin, M., Badosa, J., Pascal, N., and Montoux, N.: ELIFAN, an algorithm for the estimation of cloud

cover from sky imagers, *Atmos. Meas. Tech.*, 12, 5519–5534, <https://doi.org/10.5194/amt-12-5519-2019>, 2019.

Mahrt, F., Kilchhofer, K., Marcolli, C., Grönquist, P., David, R. O., Rösch, M., et al. The impact of cloud processing on the ice nucleation abilities of soot particles at cirrus temperatures. *Journal of Geophysical Research: Atmospheres*, 125, e2019JD030922, <https://doi.org/10.1029/2019JD030922>, 2020.

Masson, V., P. Le Moigne, E. Martin, S. Faroux, A. Alias, R. Alkama, S. Belamari, A. Barbu, A. Boone, F. Bouyssel, P. Brousseau, E. Brun, J.-C. Calvet, D. Carrer, B. Decharme, C. Delire, S. Donier, K. Essaouini, A.-L. Gibelin, H. Giordani, F. Habets, M. Jidane, G. Kerdraon, E. Kourzeneva, M. Lafaysse, S. Lafont, C. Lebeaupin Brossier, A. Lemonsu, J.-F. Mahfouf, P. Marguinaud, M. Mokhtari, S. Morin, G. Pigeon, R. Salgado, Y. Seity, F. Taillefer, G. Tanguy, P. Tulet, B. Vincendon, V. Vionnet, and A. Voltaire, The SURFEXv7.2 land and ocean surface platform for coupled or offline simulation of earth surface variables and fluxes, *Geosci. Model Dev.*, 6, 929–960, <https://doi.org/10.5194/gmd-6-929-2013>, 2013.

Mazon J. and D. Pino, A WRF Simulation of an Episode of Contrails Covering the Entire Sky, *Atmosphere*, 7, 95, 9p. <https://doi.org/10.3390/atmos7070095>, 2016.

Miltenberger, A. K., Field, P. R., Hill, A. A., Rosenberg, P., Shipway, B. J., Wilkinson, J. M., ... & Blyth, A. M. Aerosol–cloud interactions in mixed-phase convective clouds–Part 1: Aerosol perturbations. *Atmospheric Chemistry and Physics*, 18(5), 3119-3145. <https://doi.org/10.5194/acp-18-3119-2018>, 2018.

Misaka, T., F. Holzäpfel, I. Hennemann, T. Gerz, M. Manhart, and F. Schwertfirm, Vortex bursting and tracer transport of a counter-rotating vortex pair. *Physics of Fluids*, 24(2), <https://doi.org/10.1063/1.3684990>, 2012.

Mishchenko M. I., Travis L. D., Laci A. A., Scattering, absorption, and emission of light by small particles, Cambridge University Press, ISBN 9780521782524, 462 pp., 2002.

Montreuil E., W. Ghedhaïfi, V. Chmielarski, F. Vuillot, F. Gand and A. Loseille, Numerical simulation of contrail formation on the Common Research Model wing/body/engine configuration, 10th Atmospheric and Space Environments conference, Atlanta (GA), <https://DOI.ORG/10.2514/6.2018-3189>, June 2018.

Myhre G., M. Kvalevåg, G. Rädcl, J. Cook, K. P. Shine, H. Clark, F. Karcher, K. Markowicz, A. Kardas, P. Wolkenberg, Y. Balkanski, M. Ponater, P. Forster, A. Rap, R. R. De Leon, Intercomparison of radiative forcing calculations of stratospheric water vapour and contrails, *Meteorologische Zeitschrift*, Vol. 18, No. 6, 585-596, <https://doi.org/10.1127/0941-2948/2009/0411>, 2009.

Nuic, A., Poles, D., Mouillet, V. BADA: An advanced aircraft performance model for present and future ATM systems. *Int. J. Adapt. Control Signal Process.* 24, 850–866. <http://doi.wiley.com/10.1002/acs.1176>, 2010.

Penner, J.E., C. Zhou, A. Garnier, D.L. Mitchell. Anthropogenic aerosol indirect effects in cirrus clouds. *J. Geophys. Res. Atmos.*, 123, pp. 11,652-11,677, <https://doi.org/10.1029/2018JD029204>, 2018.

OAG Aviation Worldwide Limited. Historical schedules data for 2012 and 2018. <https://www.oag.com/airline-schedules-data>, 2019.

Paoli, R., F. Laporte, B. Cuenot, and T. Poinot, Dynamics and mixing in jet/vortex interactions, *Physics of Fluids*, 15(7):1843–1860, <https://doi.org/10.1063/1.1575232>, 2003.

- Paoli R. and K. Shariff, Turbulent condensation of droplets: direct simulation and a stochastic model, *J. Atmos. Sci.*, 66, 723-740, <https://doi.org/10.1175/2008JAS2734.1>, 2009.
- Paoli, R., L. Nybelen, J. Picot, D. Cariolle, Effects of jet/vortex interaction on contrail formation in supersaturated conditions, *Phys. Fluids*, 25, 053305, <https://doi.org/10.1063/1.4807063>, 2013.
- Paoli R. and K. Shariff, Contrail Modelling and Simulation, *Annu. Rev. Fluid. Mech.*, 48, 393-427, <https://doi.org/10.1146/annurev-fluid-010814-013619>, 2016.
- Paoli R., O. Thouron, D. Cariolle, M. Garcia, J. Escobar, Three-dimensional large-eddy simulations of the early phase of contrail-to-cirrus transition: effects of atmospheric turbulence and radiative transfer, *Meteorologische Zeitschrift*, 26, N°26, 597-620, <https://doi.org/10.1127/metz/2017/0764>, 2017.
- Papamoschou, D. and A. Roshko, The compressible turbulent shear layer: an experimental study, *Journal of fluid Mechanics*, 197:453–477, <https://doi.org/10.1017/S0022112088003325>, 1988.
- Paugam R., Simulation numérique de l'évolution d'une traînée de condensation et de son interaction avec la turbulence atmosphérique, PHD, 212p, (tel-01666360), <https://hal.archives-ouvertes.fr/tel-01666360/>, 2008.
- Paugam R., R. Paoli, D. Cariolle, Influence of vortex dynamics and atmospheric turbulence on the early evolution of a contrail, *Atmos. Chem. Phys.*, 10, 3933-3952. <https://doi.org/10.5194/acp-10-3933-2010>, 2010.
- Picot J., Simulation aux grandes échelles de traînées de condensation dans un milieu atmosphérique stratifié et turbulent., *Océan, Atmosphère*. Université de Toulouse III - Paul Sabatier, <https://tel.archives-ouvertes.fr/tel-00828483>, 2013.
- Picot J., R. Paoli, O. Thouron and D. Cariolle, Large-eddy simulation of contrail evolution in the vortex phase and its interaction with atmospheric turbulence, *Atmos. Chem. Phys.*, 15, 7369–7389, <https://doi.org/10.5194/acp-15-7369-2015>, 2015.
- Planespotters. Global aircraft fleet data as of 2019–07-23. Data provided by Planespotters.net. <https://www.planespotters.net/>, 2019.
- Quadros F. D.A., M. Snellen, J. Sun, and I. C. Dedoussi, Global Civil Aviation Emissions Estimates for 2017–2020 Using ADS-B Data, *Journal of Aircraft*, 1-11, <https://doi.org/10.2514/1.C036763>, 2022.
- Rap A., P.M. Forster, A. Jones, O. Boucher, J. M. Haywood, N. Bellouin, R. De Leon, Parametrization of contrails in the UK Met Office Climate Model, *J. Geo. Res.*, 115, D10205, 15p. <https://doi.org/10.1029/2009JD012443>, 2010.
- Righi, M., J. Hendricks, R. Sausen, The global impact of the transport sectors on atmospheric aerosol: simulations for year 2000 emissions. *Atmos. Chem. Phys.*, 13, pp. 9939-9970, <https://doi.org/10.5194/acp-13-9939-2013>, 2013.
- Sans M., El Hafi M., Eymet V., Forest V., Fournier R., Villefranque N., Null-collision meshless Monte Carlo - A new reverse Monte Carlo algorithm designed for laser-source emission in absorbing/scattering inhomogeneous media. *Journal of Quantitative Spectroscopy and Radiative Transfer*, 271, 107725, <https://doi.org/10.1016/j.jqsrt.2021.107725>, 2021.

Schäfer Matthias, Martin Strohmeier, Vincent Lenders, Ivan Martinovic and Matthias Wilhelm. "Bringing Up OpenSky: A Large-scale ADS-B Sensor Network for Research". In Proceedings of the 13th IEEE/ACM International Symposium on Information Processing in Sensor Networks (IPSN), pages 83-94, April 2014.

Schumann U., A contrail cirrus prediction tool, *Geosci. Model Dev.* 5, 543-580. <https://doi.org/10.5194/gmd-5-543-2012>, 2012.

Schumann, U.: On conditions for contrail formation from aircraft exhausts, *Meteorologische Zeitschrift*, 5, <https://doi.org/10.1127/metz/5/1996/4>, 1996.

Schumann U., T. Hauf, H. Höller, H. Schmidt, H. Volkert, A mesoscale Model for the Simulation of Turbulence, Clouds and Flow over Mountains: Formulation and Validation Examples, *Beitr. Phys. Atmosph.*, 60, 4, 416-446, <https://elib.dlr.de/64724/>, 1987.

Schumann U., A. J. Heymsfield, Chapter 3, On the life cycle of individual contrails and contrail cirrus, *Meteo. Monograph*, 58, 24p, <https://doi.org/10.1175/AMSMONOGRAPHS-D-16-0005.1>, 2017.

Seymour, K, M. Held, G. Georges, K. Boulouchos. Fuel Estimation in Air Transportation: Modeling global fuel consumption for commercial aviation, *Transportation Research Part D: Transport and Environment*, 88, 102528, <https://doi.org/10.1016/j.trd.2020.102528>, 2020.

Sharmann R., C. Tebaldi, G. Wiener, J. Wolff, An integrated approach to mid- and upper-level turbulence forecasting, *Wea. Forecast.*, 21, 268–287, <https://doi.org/10.1175/WAF924.1>, 2005.

Skamarock W. C., Klemp J. B., Dudhia J., Gill D. O., Barker D. M., Duda M. G., Huang X.-Y., Wang W., Powers J. G., A description of the Advanced Research WRF Version 4, NCAR/ TN-556+STR, <https://doi.org/10.5065/1dfh-6p97>, 2019.

Smirnov A., S. Shi, and I. Celik, Random Flow Generation Technique for Large Eddy Simulations and Particle-Dynamics Modeling, *ASME. J. Fluids Eng.*, 123(2), 359–371, <https://doi.org/10.1115/1.1369598>, 2001.

Smolarkiewicz, P.K. and L.G. Margolin, On forward-in-time differencing for fluids: an Eulerian/Semi-Lagrangian non-hydrostatic model for stratified flows, *Atmos. Oceans*, 35, 127–152, <https://doi.org/10.1080/07055900.1997.9687345>, 1997.

Smolarkiewicz P. K. and L.G. Margolin, MPDATA: A finite-difference solver for geophysical flows, *J. Comput. Phys.*, 140, (2), pp 459–480, <https://doi.org/10.1006/jcph.1998.5901>, 1998.

Smolarkiewicz P.K., C. Kühnlein and N.P. Wedi, A consistent framework for discrete integrations of soundproof and compressible PDEs of atmospheric dynamics. *J. Comput. Phys.*, 263, 185–205. <https://doi.org/10.1016/j.jcp.2014.01.031>, 2014.

Sölch I. and Kärcher, B., A large-eddy model for cirrus clouds with explicit aerosol and ice microphysics and Lagrangian ice particle tracking, *Q. J. Roy. Meteorol. Soc.*, 136, 2074–2093, <https://doi.org/10.1002/qj.689>, 2010.

Spalart P.R. and A.A. Wray, Initiation of the Crow instability by atmospheric turbulence. *Proc. AGARD Symp.*, Trondheim, Norway, CP-584, 18.1–18.8, 1996.

Spichtinger, P., Gierens, K., Leiterer, U., and Dier, H.: Ice supersaturation in the tropopause region over Lindenberg, Germany, *Meteorologische Zeitschrift*, 12, 143–157, <https://doi.org/10.1127/0941-2948/2003/0012-0143>, 2003

Spichtinger, P., Gierens, K., and Wernli, H.: A case study on the formation and evolution of ice supersaturation in the vicinity of a warm conveyor belt's outflow region, *Atmos. Chem. Phys.*, 5, 973–987, <https://doi.org/10.5194/acp-5-973-2005>, 2005.

Spichtinger, P. and Gierens, K. M. Modelling of cirrus clouds – Part 1a: Model description and validation, *Atmos. Chem. Phys.*, 9, 685–706, <https://doi.org/10.5194/acp-9-685-2009>, 2009.

Stuefer M., X. Meng, G. Wendler, MM5 contrail forecasting in Alaska, *Mon. Wea. Rev.*, 133, 3517- 3526, <https://doi.org/10.1175/MWR3048.1>, 2005.

Sun J, Hoekstra JM, Ellerbroek J. OpenAP: An Open-Source Aircraft Performance Model for Air Transportation Studies and Simulations. *Aerospace*; 7(8):104. <https://doi.org/10.3390/aerospace7080104>, 2020.

Sussmann R. and K.M. Gierens, Lidar and numerical studies on the different evolution of vortex pair and secondary wake in young contrails, *J. Geophys. Res.*, 104(D2), 2131-2142. <https://doi.org/10.1029/1998JD200034>, 1999.

Sussmann R. and K. M. Gierens, Differences in early contrail evolution of two-engine versus four-engine aircraft: Lidar measurements and numerical simulations, *J. Geophys. Res. Atmos.*, 106, 4899-4911, <https://doi.org/10.1029/2000JD900533>, 2001.

Terrenoire, E., Hauglustaine, D., Cohen, Y., Cozic, A., Valorso, R., Lefèvre, F., and Matthes, S.: Impact of present and future aircraft NO<sub>x</sub> and aerosol emissions on atmospheric composition and associated direct radiative forcing of climate, *Atmos. Chem. Phys. Discuss.*, <https://doi.org/10.5194/acp-2022-222>, in review, 2022.

Tessé L., J.-M. Lamet, Radiative transfer modeling developed at ONERA for numerical simulations of reactive flows, *AerospaceLab Journal*, Issue 2, <https://aerospacelab.onera.fr/Radiative-Transfer-Modeling-Developed>, 2011.

Unterstrasser S., K. Gierens K., P. Spichtinger P., The evolution of contrail microphysics in the vortex phase, *Meteor. Zeitschrift*, 17, 2, 145-156, <https://doi.org/10.1127/0941-2948/2008/0273>, 2008.

Unterstrasser S. and K. Gierens, Numerical simulations of contrail-to-cirrus transition – Part 1: An extensive parametric study, *Atmos. Chem. Phys.*, 10, 2017-2036, <https://doi.org/10.5194/acp-10-2017-2010>, 2010a.

Unterstrasser S. and K. Gierens, Numerical simulations of contrail-to-cirrus transition – Part 2: Impact of initial ice crystal number, radiation, stratification, secondary, nucleation and layer depth, *Atmos. Chem. Phys.*, 10, 2037-2051. <https://doi.org/10.5194/acp-10-2037-2010>, 2010b.

Unterstrasser S., I.Sölch, Study of contrail microphysics in the vortex phase with a Lagrangian particle tracking model, *Atmos. Chem. Phys.*, 10, 10003–10015, <https://doi.org/10.5194/acp-10-10003-2010>, 2010.

- Unterstrasser S., R. Paoli, I. Sölch, C. Kühnlein and T. Gerz, Dimension of aircraft exhaust plumes at cruise conditions: effect of wake vortices, *Atmospheric Chemistry and Physics*, 14, 5, 2713-2733, <https://doi.org/10.5194/acp-14-2713-2014>, 2014.
- Unterstrasser S. and I. Sölch (2014), Optimisation of simulation particle number in a Lagrangian ice microphysical model, *Geosci. Model Dev.*, 7, 695–709, <https://doi.org/10.5194/gmd-7-695-2014>, 2014.
- Unterstrasser S., K. Gierens, I. Sölch, M. Lainer, Numerical simulations of homogeneously nucleated natural cirrus and contrail-cirrus. Part 1: how different are they? *Meteo. Zeitschrift*, 26, 6, 621-642, <https://doi.org/10.1127/metz/2016/0777>, 2016.
- Unterstrasser S. and A. Stephan, Far field wake vortex evolution of two aircraft formation flight and implications on young contrails, *The Aeronautical Journal*, 124 (1275), 667-702, <https://doi.org/10.1017/aer.2020.3>, 2020.
- Urquhart, B., Kurtz, B., and Kleissl, J.: Sky camera geometric calibration using solar observations, *Atmos. Meas. Tech.*, 9, 4279–4294, <https://doi.org/10.5194/amt-9-4279-2016>, 2016.
- Vassberg, J., M. DeHaan, M. Rivers and R. Wahls, Development of a Common Research Model for Applied CFD Validation Studies, AIAA Paper 2008-6919, 2008.
- Villefranche N., R. Fournier, F. Couvreur, S. Blanco, C. Cornet, V. Eymet, V. Forest, J.-M. Tregan, A Path-Tracing Monte Carlo Library for 3-D Radiative Transfer in Highly Resolved Cloudy Atmospheres, *J. Adv. Model. Earth Syst.*, 11, 2449-2473, <https://doi.org/10.1029/2018MS001602>, 2019.
- Warren S. G., R. E. Brandt, Optical constants of ice from the ultraviolet to the microwave: A revised compilation, *J. Geophys. Res.*, 113, D14220, <https://doi.org/10.1029/2007JD009744>, 2008.
- Wells, C.A., P.D. Williams, N.K. Nichols, D. Kalise and I. Poll. Reducing transatlantic flight emissions by fuel-optimised routing. *Environ. Res. Lett.* 16 025002. <https://doi.org/10.1088/1748-9326/abce82>, 2021.
- Yang P., Liou K. N., Wyser K., Mitchell D., Parameterization of the scattering and absorption properties of individual ice crystals, *J. Geophys. Res.*, Vol. 105, No. D4, 4699–4718, <https://doi.org/10.1029/1999JD900755>, 2000.
- Yang F., H.-L. Pan, S.K. Krueger, S. Moorthi and S.J. Lord, Evaluation of the NCEP Global Forecast System at the ARM SCP Site, *Mon. Wea. Rev.*, 134, 3668-3690, <https://doi.org/10.1175/MWR3264.1>, 2006.
- Yang, H., Dobbie, S., Mace, G. G., Ross, A., & Quante, M. GEWEX Cloud System Study (GCSS) cirrus cloud working group: development of an observation-based case study for model evaluation. *Geoscientific Model Development*, 5(3), 829-843. <https://doi.org/10.5194/gmd-5-829-2012>, 2012.